Diffusiophoresis in complex and confined fluids

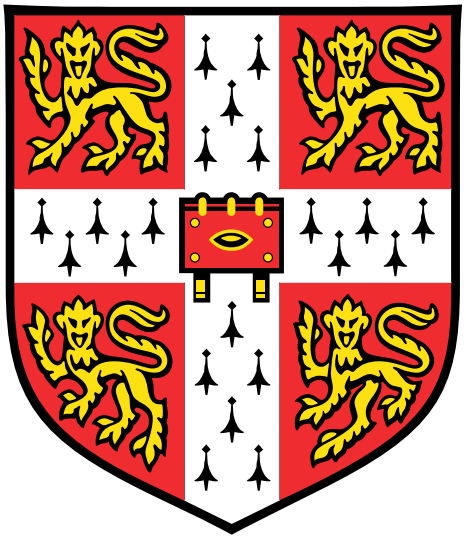

Simón Ramírez Hinestrosa
Darwin College

Supervisor: Prof. Daan Frenkel

Department of Chemistry
University of Cambridge

This thesis is submitted for the degree of
Doctor of Philosophy

Darwin College December 2020

Declaration

This thesis is the result of my own work and includes nothing which is the outcome of work done in collaboration except as declared in the Preface and specified in the text. It is not substantially the same as any that I have submitted, or, is being concurrently submitted for a degree or diploma or other qualification at the University of Cambridge or any other University or similar institution except as declared in the Preface and specified in the text. I further state that no substantial part of my thesis has already been submitted, or, is being concurrently submitted for any such degree, diploma or other qualification at the University of Cambridge or any other University or similar institution except as declared in the Preface and specified in the text. It does not exceed the prescribed word limit for the relevant Degree Committee

Simón Ramírez Hinestrosa
Darwin College
December 2020

Diffusiophoresis in complex and confined fluids

Simón Ramírez Hinestrosa
Darwin College

Moving fluids at the micro- and nano-scales requires a different approach compared to the traditional methods based on pressure gradients. The increase of surface/volume ratio as the length of the systems decreases the efficiency of the latter. The use of thermodynamic forces such as electric fields, chemical potential and temperature gradients is crucial for effective transport when the local perturbation of the fluid at the interfaces becomes relevant. The specific case of chemical potential gradients in fast-moving components of a solution driving the movement of colloids, polymers and other moieties is known as diffusiophoresis. In this thesis, we study diffusiophoresis using a combination of theory and computer simulations. We use non-equilibrium thermodynamics, starting from the entropy production to build our theoretical framework aiming to discuss some subtleties present in previous works. As the first case of study, we perform non-equilibrium molecular dynamics to analyse the movement of a very large colloid using the Derjaguin-Anderson approximation, reducing the problem to a diffusio-osmotic flow. In the simulations, we drive the system out of equilibrium by applying microscopic representations of the chemical potential gradient that are compatible with periodic boundary conditions. We then report the first applications of such a method to a colloidal system and compare it with simulations where explicit concentration gradients are imposed. Our approach is more convenient as we decouple diffusiophoresis from strong advective effects. We find a non-monotonic relation between the diffusiophoretic mobility of the colloid and the strength of the interaction with the solution. Finally, we report a numerical study of polymer diffusiophoresis, finding that the existing theory for solid particles is not accurate for polymer coils. Moreover, we observe that the hydrodynamic flow through the polymer is less screened than for pressure-driven flows.

Pedes in terra ad sidera visus

Acknowledgements

My time in Cambridge has been one of the most exciting experiences in my life. Here, I was living a dream that I never allowed myself to have, something that I thought was unreachable. Walking on the same streets where Newton, Darwin and Hawking once did, made me feel grateful every day. Ever since I read "a brief history of time", I fell in love with physics, and words cannot express the happiness that I felt when I met Hawking in person here in Cambridge. Physics will always be in my life no matter which path I choose next.

I would like to thank my supervisor Professor Daan Frenkel for always inspiring me and giving me the freedom to get immersed - sometimes more than I should - and enjoy my scientific journey. He supported the choices I made during my PhD, sometimes being the most polite Dutch I have ever met. I gratefully acknowledge all the present and past members of the group, especially Raman Ganti and Peter Wirnsberger, for their invaluable support during the first part of my PhD. Furthermore, Xipeng Wang for allowing me to participate in his projects, where I learned new topics while clearing my mind from my main subject. I would also like to thank Stephen Cox, Oded Farago, Robert Jack, Richard Sear, Shaltiel Eloul and Hiroaki Yoshida for the stimulating conversations that brought new ideas to my research. In my memories from the chemistry department, I have a special place for Vignolini's group that adopted me as an honorary member.

My life in Cambridge was, certainly, not only research, and I was lucky to find great people that triggered my curiosity about other exciting topics and points of view. Among all the interesting people that I met, Gianni, Miriam and Toby were always there. We shared our frustrations, expectations and thoughts during endless conversations. Here, I also met Christiane, with whom I have shared my life since, and I feel very fortunate to have by my side.

I also acknowledge the European Union for funding both my Masters and my PhD. I believe the concept of the Union is something that many take for granted, but as a foreigner, I have got nothing but great support. Thanks to the Nanotrans ETN (Grant No. 674979), the network that allowed me to meet not only colleagues but friends. Special thanks to my research hosts Patrick Warren and Lydéric Bocquet.

Finally, to my family, the engine that keeps me running and have supported all my decisions and endeavours. I am extremely lucky for having such a progressive family in a country where the "macondian" reality often exceeds fiction. Where choosing science is considered a wild decision without any future. My family has always helped me keep my feet on the ground, looking at the starts.

Publications

During my PhD, I have contributed to the following publication:

1. Wang, X., **Ramirez-Hinestrosa, S.** and Frenkel, D. (2020) 'Using Molecular Simulation to Compute Transport Coefficients of Molecular Gases'
   J. Phys. Chem. B 2020, 124, 35, 7636.

2. **Ramírez-Hinestrosa, S.**, Yoshida, H., Bocquet, L. and Frenkel, D. (2020) 'Studying polymer diffusiophoresis with non-equilibrium molecular dynamics'
   J. Chem. Phys. 152, 164901 (2020).

3. Wei, J., **Ramírez-Hinestrosa, S.**, Dobnikar, J. and Frenkel, D. (2020) 'Effect of the interaction strength and anisotropy on the diffusio-phoresis of spherical colloids'
   Soft Matter, 2020, 16, 3621.

4. Wang, X., **Ramírez-Hinestrosa, S.** and and Frenkel, D. (2020) 'The Lennard-Jones potential: when (not) to use it'
   Phys. Chem. Chem. Phys., 2020, 22, 10624.

Table of contents

Nomenclature

Acronyms

BD-NEMD Boundary-Driven Non-Equilibrium Molecular Dynamics

DCV-GCMD Dual Control Volume Grand Canonical Molecular Dynamics

DCV-SGCMC Double Control Volume Semi-Grand Canonical Molecular Dynamics

EMD Equilibrium Molecular Dynamics

FD-NEMD Field-Driven Non-Equilibrium Molecular Dynamics

GK Green-Kubo

LNET Linear Non-Equilibrium Thermodynamics

LTE Local Thermal Equilibrium

MC Monte Carlo

MD Molecular Dynamics

NEMD Non-Equilibrium Molecular Dynamics

NS Navier-Stokes

Superscripts

B Bulk region

Subscripts

f Solvents

m Monomer

p	Polymer
s	Solutes
dp	Diffusiophoresis

Symbols

α	Concentration gradient magnitude
β	Diffusivity difference factor
Δx^{ss}	Distance between control volumes in DCV simulations
Δ_z	Spacial binning in the z direction
η	Shear viscosity
γ	Surfacial tension
Γ_i	Gibbs surface excess of particles of species i
λ	Small parameter in the asymptotic expansion by Anderson
$\mathscr{H}$	Hamiltonian
μ	Chemical potential
ϕ	Effective interaction potential
Π	Stress tensor
ρ	mass density
σ_i	Local production of species i
σ_s	Entropy production
$\mathbf{E}$	Electric field
$\mathbf{F}_i^{\mu}$	Microscopic force on particles of species i due to a chemical potential gradient
$\mathbf{J}_i$	Flux of particles of species i
$\mathbf{J}_q$	Heat flux i
$\mathbf{J}_{s_V}$	Entropy flux

$\mathbf{v}$	Fluid velocity
ζ	Bulk viscosity
a	Radius of a colloidal particle
A_j	Chemical affinity of reaction j
C	Ionic concentration
c_i	Concentration of species i
$d_i^{\min}$	Minimum approach distance for particles of species i
e	Proton charge
g_{ij}	Reaction coefficients
H	Second moment of the excess solute distribution
J_j	Chemical reaction rate of reaction j
k_B	Boltzmann constant
L	Diffuse layer thickness
L^*	Characteristic length of the diffuse layer
L_c	Box side
L_{sys}	Typical length of the system
$M_{\alpha\delta}$	Transport coefficients
n	Number of species
N_i	Number of particles of species i
P	Pressure
Pe^{BD}	Péclet number for BD-NEMD simulations
Pe^{FD}	Péclet number for FD-NEMD simulations
r_c	Potential cutoff
r_f	Solvent radius

R_H	Hydrodynamic radius
r_s	Solute radius
S	Entropy
s_V	Entropy density
T	Temperature
V	Volume
v	Velocity
v^B	Slip velocity
X^*	Reduced quantity X
Z	Valence number
D	Diffusion coefficient

Chapter 1

Introduction

"There's plenty of room at the bottom."

Richard P. Feynman

Moving fluids at the macro-scale is intuitive and regular in our daily life. Pressure gradients drive water through pipes and lift aircrafts. With the advent of nanotechnology, the ability to design new materials has increased immensely. The miniaturisation and exquisite control in the manufacturing of widely available micro and nano-fluidic devices open up a new horizon in science. It also brings new challenges, as the reduction in scale increases the surface area to volume ratio considerably in such systems. Under those conditions, pressure gradients are not efficient anymore, and thermal fluctuations together with other phenomena ignored at the macro-scale become dominant. Additional to the practical challenges, Navier-Stokes predictions break down at the interface between the liquid and a solid surface. The answer to solving the problems also resides at the interface. This small region is where phoretic motion originates and drives the movement of the entire system. Etymologically, *phoresis* stems from the Greek "to bear" or "to carry". The carrying forces include temperature gradients (thermophoresis), concentration gradients (diffusiophoresis) or electric fields (electrophoresis). In the case of diffusiophoresis, the concentration gradients of the various fast-moving components of a solution carry larger, slower objects, such as colloids and polymers. The enhanced transport of the large particles could be up to two orders of magnitude faster than their self-diffusion [1].

1.1 A brief history of phoresis

Thermophoresis was first described by Tyndall in 1870 [2] when he was measuring how dust particles distributed close to surfaces. He noticed that there were dark spots in the scattered light from heated areas. Almost a decade later, Maxwell [3] and Reynolds [4] studied the transpiration of gases through porous plates due to an external temperature gradient and the anisotropies in the pressure distributions caused by those temperature gradients. Since then, thermophoresis has been widely studied due to its importance in industrial applications such as vapour deposition, aerosols and micro-contamination control [5]. Moreover, many applications are related to thermophoresis in liquids and the transport of colloids [6].

The earliest report on electro-osmosis dates back to 1807, with the pioneering work by Reuss [7]. His experimental setup consisted of two reservoirs filled with water and separated by a porous barrier. When he applied an electric current through the system, he observed water flow from the anode to the cathode. Electrophoresis was observed as early as the 1740s [8]. It was not until the early 1920s, with the works of Svedberg and his collaborators, that electrophoretic applications started. In those days, little was known about the detailed chemical composition of proteins but Svedberg was convinced that proteins were polydisperse [9]. In 1923, Svedberg & Jette were studying egg albumin with a technique called "cataphoresis" [10]. This method was later improved by Scott & Svedberg [11], making it possible to measure protein mobilities and finally, Svedberg & Tiselius [12] optimised the optical detection of the method. Years later, Tiselius published a more accessible [13] compendium that attracted wide attention. Tiselius received the Nobel prize in Chemistry in 1948 for his work on electrophoresis, which allowed him to separate materials once believed to be homogeneous.

Turning our attention to diffusiophoresis, the first systematic study of this phenomenon was published by Derjarguin in 1947 [14]. Almost four decades later, Anderson & Prieve [15, 16] investigated the diffusiophoresis of colloidal particles in detail, both experimentally and theoretically.

1.2 Applications

Diffusiophoresis is not used as extensively as electrophoresis. A possible reason is its late identification and the fact that it is not entirely understood. Only in the last decade, the consequences of diffusiophoresis for a wide variety of applications have started to emerge [17, 18]. From the origin of life [19] to solving long-standing laundry detergency problems [20], phoresis has a wide range of applications, moving fluids, DNA, proteins and colloids through

pores and small channels due to the reduction of the dissipation phenomena [21]. One of the first commercial applications of diffusiophoresis was in the formation of rubber gloves and the deposition of paint films onto steel surface [16], highlighting the importance of this mechanism in drying films [22, 23]. Nowadays, lab on a chip, devices at the forefront of science, rely strongly on this transport phenomenon [24–26]. Furthermore, in energy storage and desalinisation processes, there is a growing interest in applications harnessing concentration gradients to drive fluid flows [27, 18]. This is because, among all different phoretic mechanisms, diffusiophoresis has the advantage that it does not require an active internal energy input [28]. There are applications in autonomous motion [29–32], micro-nanomotors [33], micro-turbines [34]. Solute gradients enhance particle transport into and out of dead-end pores [35, 20] and are used for separation and focusing of particles [28, 36–40]. In addition to the important role in microfluidics applications, phoresis is crucial in chemotaxis, the movement of living cells by the gradient of chemical agents [16]. Diffusiophoresis drives the transport of crucial compounds inside the cell using ATP/ADP gradients [41] and can be used for enhanced drug delivery strategies [42]

1.3 Motivation

Despite the advantages and applications mentioned above, studying diffusiophoresis remains a challenging task. A better understanding of the phenomenology at the microscopic scale is crucial, as the equations governing hydrodynamics break down for small scales close to interfaces [43, 44]. On the one hand, the standard theoretical descriptions are based on a continuum approach, in which the solvent is treated as a uniform continuum and the solutes are described by a concentration profile obeying the Smoluchowski equation in the presence of an external field. On the other hand, in experiments, it is hard to precisely control all the parameters involved in the process and gain knowledge of the dynamics at the interface. Therefore, simulations offer a valuable tool to predict mobility coefficients and unveil the underlying processes not captured by other means. Strictly speaking, diffusiophoresis is caused by a gradient in electrochemical potential. It involves two types of thermodynamic forces: the chemical potential gradients due to the different species in the solution and the local electric field due to the different mobilities of the ions. One further advantage of theoretical and numerical approaches is that the effect of charges can be neglected without losing generality [45]. Lastly, the disagreement between authors on theoretical aspects, a lack of unified definitions and the simple systems analysed suggest that diffusiophoresis requires further research.

1.4 Thesis outline

This work aims to build a clear and unified theoretical ground to describe diffusio-osmosis and diffusiophoresis. Regarding simulations, the complexity of the applications will increase, proceeding from planar surfaces to polymers, giving the necessary technical details at each step. In Chapter 2, we introduce the concepts of diffusio-osmosis and diffusiophoresis, creating a link between them and describing their microscopic origins. We present the fundamental theory to understand phoresis and describe the main algorithms used to examine them. Our focus is on Non-Equilibrium Molecular Dynamics (NEMD) and the different approaches to include thermodynamic forces compatible with periodic boundary conditions. In Chapter 3, we explore diffusio-osmosis extending the results available in the literature and carefully making connections to the theory. We explore the relevant parameters in Derjaguin-Anderson theory and compute them using equilibrium molecular dynamics. In Chapter 4, we study Anderson's theory to describe the diffusiophoresis of spherical particles. We take a novel approach to simulate colloidal diffusiophoresis that is a natural extension from the techniques used in diffusio-osmosis. In Chapter 5, we focus on polymer diffusiophoresis exploring the limitations in the theoretical descriptions to describe non-spherical particles with fluctuating shape and an intrinsically fuzzy surface. Finally, we conclude with a summary and future outlook in Chapter 6.

Chapter 2

Theoretical Background

"Ludwig Boltzmann, who spent much of his life studying statistical mechanics, died in 1906, by his own hand. Paul Ehrenfest, carrying on the work, died similarly in 1933. Now its our turn to study statistical mechanics."

David L. Goodstein

2.1 From osmosis to phoresis

Before starting the discussion, it is worth pointing out that in the literature, concentration and chemical potential gradients are taken as equivalent driving forces for diffusion. The former is not a thermodynamic force and should not be used. For instance, in an ideal solution, when the connection between the concentration and chemical potential gradient is straightforward, the driving force senses the gradient in the logarithm of the concentration rather than its distribution. Moreover, the Fickian approach, common in continuum-based formulations, exposes another conceptual problem, the assumption that cross-terms in the diffusivity matrix can be neglected [46, 47]. In this chapter, we introduce a non-equilibrium thermodynamic approach, in which the chemical potential gradient, or a linear combination of thermodynamic forces, unambiguously drives the dynamics of a system. We also discuss how the chemical potential gradients in a mixture are connected and that Onsager's reciprocity is fulfilled.

2.1.1 Thermodynamic description

It is useful to employ equilibrium thermodynamics as a first attempt to describe diffusiophoresis. In Fig. 2.1, we show a colloid of radius a immersed in a binary solution with solutes and solvents. There is a gradient of chemical potential in the solutes $\nabla\mu_s$. Let $\mu_{s,1}$ be the chemical potential in one side of the system and $\mu_{s,2}$ on the other side such that $\mu_{s,2} > \mu_{s,1}$. Finally, let us suppose that the solute interacts preferentially with the colloid.

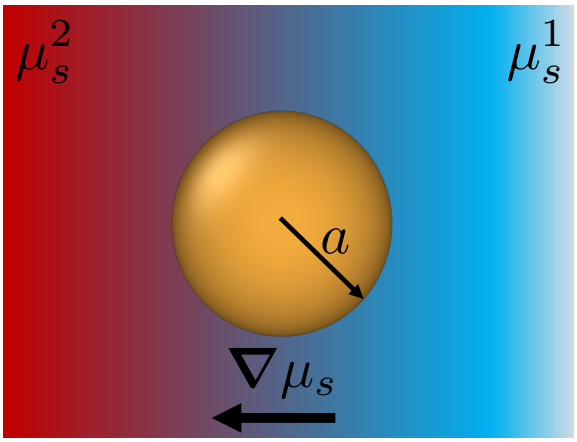

Fig. 2.1 Spherical colloid with radius a in a binary solution of solute and solvent. There is a solute chemical potential gradient $\nabla\mu_s$ between the two extremes at $\mu_{s,1}$ and $\mu_{s,2}$.

Since the solute is adsorbed at the surface of the colloid, we can express the change in free energy ΔG between regions 1 and 2 as

$$\Delta G = 4\pi a^2(\gamma_2 - \gamma_1)\,, \tag{2.1}$$

where γ is the interfacial tension. As $\mu_{s,2} > \mu_{s,1}$ then $\gamma_2 < \gamma_1$ and the particle tends to move spontaneously towards the region with higher solute concentration. This can be generalised for a case where the concentration changes continuously with the position,

$$\nabla G = 4\pi a^2 \left(\frac{\partial\gamma}{\partial\mu_s}\right)\nabla\mu_s\,. \tag{2.2}$$

Although this approach predicts that the colloidal particle should move, there is no way to quantify its speed. In chapter 4, we will use non-equilibrium thermodynamics to estimate the diffusiophoretic velocity in this system. For now, we will introduce another useful result from thermodynamics, the Gibbs-Duhem equation. It helps to understand how diffusiophoresis converts the chemical energy into mechanical energy of colloids moving through the fluids;

it does so by producing a local electric field or pressure gradient [17]. Let us suppose a system with n species, each species i composed of N_i particles with chemical potential μ_i. All the particles are kept in a volume V at pressure P, temperature T and entropy S. Therefore Gibbs-Duhem is given by

$$V\,dP - S\,dT = \sum_{i=1}^{n} N_i\,d\mu_i\,. \tag{2.3}$$

Using this relation, we see that, for instance, in a binary system at constant pressure and temperature, a gradient in the chemical potential of a single species directly induces a gradient in the other component. Moreover, if there is an isothermal process for a solution close to a surface, there is a local pressure gradient depending on the chemical potential gradients (see Chapter 3).

2.1.2 The boundary layer approximation

We just gave a thermodynamic description of diffusiophoresis without taking into account the specific microscopic details of the problem. As an example, the presence of the colloid perturbs the neighbouring fluid creating a heterogeneous region close to its surface known as the diffuse layer. Let us investigate this in more detail, in the case of the colloid radius a being much larger than the diffuse layer thickness L. Derjaguin used this approximation [14], the boundary layer approximation, to separate the problem into two regions: one inside and the other one outside the diffuse layer. Thanks to the scale separation, the dynamics can be studied inside the diffusive layer. In this approximation, the diffusiophoretic problem reduces to a fluid subject to a gradient of chemical potential flowing above a flat surface as shown in Fig. 2.2. Therefore, the study focuses on the *diffusio-osmosis*, i.e the movement of a fluid influenced by a chemical potential gradient in contact with a solid surface. To connect the two scales, Derjaguin argues that the diffusiophoretic velocity of the particle is given by $v_{\mathrm{dp}} = -v^B$, where v^B is the velocity of the fluid in the bulk, i.e. the limiting value far from the surface in the boundary layer approximation.

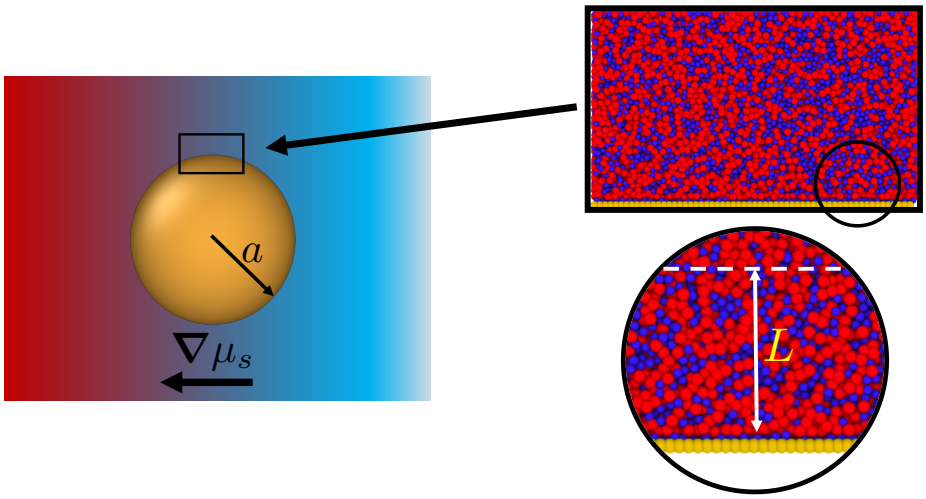

Fig. 2.2 Diffusio-osmosis can be seen as diffusiophoresis under the boundary layer approximation. Rather than focusing on the movement of the colloidal particle, we focus on the fluid flow on its surface. In this case, $a \gg L$, this reduces the analysis to a fluid flow on top of a flat plate, known as Derjaguin's approximation.

2.1.3 Microscopic origin

In Fig. 2.3, we show a flat solid wall and a binary solution composed of solutes s and solvents f. Each species interacts with the wall differently, with solutes being adsorbed preferentially at the solid surface. The adsorption creates an excess of solutes in the diffuse layer. Moreover, if there is a chemical potential gradient on the solutes $\boldsymbol{\nabla}\mu_s$, then they move following the thermodynamic force $-\boldsymbol{\nabla}\mu_s$. As a result of the excess at the interface, the solute movement drives the solution flow. All this takes place within the diffuse layer, beyond which the fluid moves force-free; thus we observe the typical plug-like flow [27, 48].

Not only chemical potential gradients give rise to osmosis (phoresis). There are other quantities, such as electric potential and temperature, whose gradients, known as *thermodynamic forces* (see Sec. 2.2), drive the motion in a system. Each one of them having an "excess" quantity associated. Therefore, we also have electro- and thermo-osmosis(phoresis) originating from an excess of charges or enthalpy at the interface respectively (see Fig. 2.4).

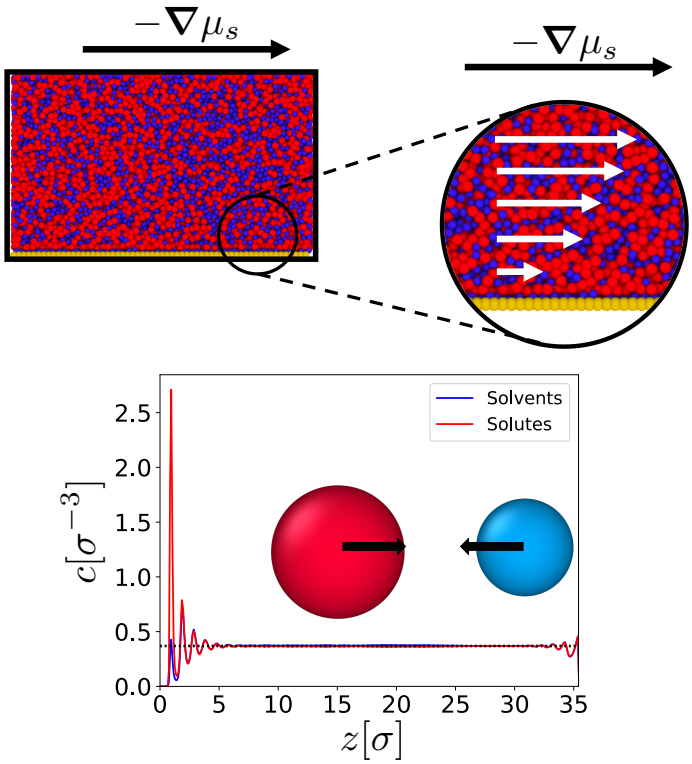

Fig. 2.3 The preferential interaction of the solutes with a solid surface creates an excess of this species at the interface. The thermodynamic force $-\nabla\mu_s$ drives the solute motion creating a net flux due to the excess at the interface, defining the flow of the whole system.

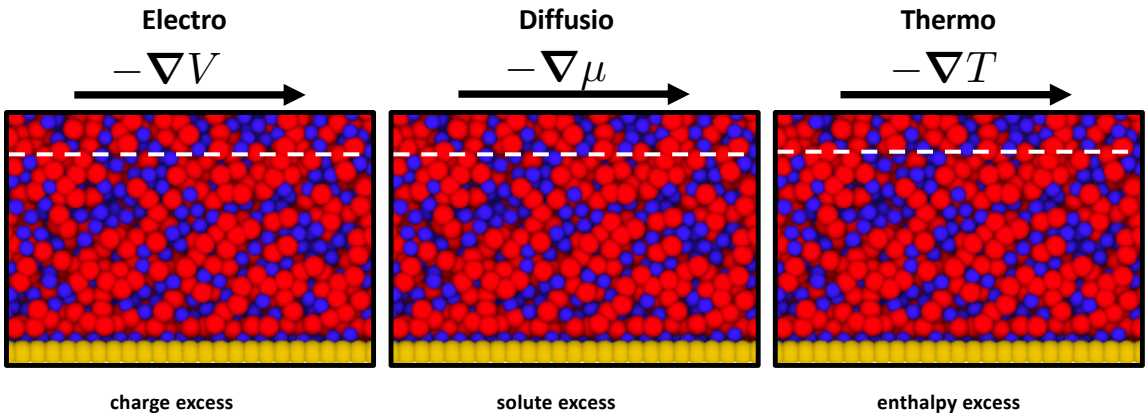

Fig. 2.4 Electro-, diffusio- and thermo-osmosis(phoresis) are interfacial phenomena originated by the excess of certain quantities that couple to the different thermodynamic forces. The excess quantities are the charge, solutes (or any species) and enthalpy, which are associated with the electric field, chemical potential gradient or temperature gradients respectively.

2.1.4 Diffusiophoresis in electrolytes

The fluid in which the colloidal particle is moving can be composed of uncharged or charged solute particles. In the former, van der Waals interactions between the colloid and the solutes drive the phoretic motion. In the latter, solutes ionise close to the surface of the particle creating an electrical double layer and the entire effect could be divided into two processes as shown in Fig. 2.5: chemiphoresis represented by the concentration gradient ∇C and electrophoresis, due to the in-situ electric field $\mathbf{E}$. In chemiphoresis, the counterions, which have an opposite charge to the surface, are adsorbed, whereas the co-ions are repelled by the particle surface. This binary solute system has two non-electrolyte type contributions each coming from co-ions and counterions concentration gradients. Finally, the electrophoretic effect results from the charged constituents that induce an electric field due to their different diffusional motion [28, 49].

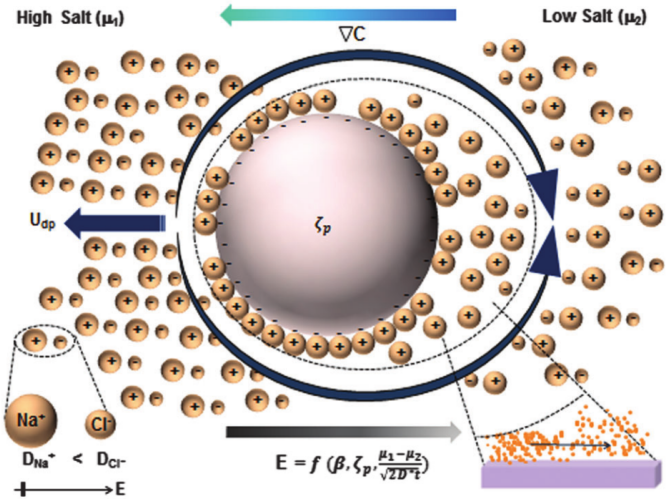

Fig. 2.5 Electrolyte diffusiophoresis diagram showing the two effects that give rise to the phenomenon. Chemiphoresis caused by the gradient of concentration in the solute ions. Electrophoresis due to the local electric field caused by the different mobilities of co-ions and counter ions [17].

It can be shown that the electric field is given by [50]

$$\mathbf{E} = \frac{k_B T}{Ze} \beta \frac{\nabla C}{C}, \tag{2.4}$$

where Z is the valence of the constituent ions of the solute, e is the proton charge, and C is the ionic concentration. β is the diffusivity difference factor which depends on the diffusion coefficient of the ions. Therefore we observe that depending on the nature of the salt, the diffusiophoretic velocity v_{dp} can be enhanced or decreased.

2.2 Linear Non-Equilibrium Thermodynamics

Consider a bulk fluid in equilibrium, the variation of any state variable creates a perturbation of the system that generates a transitory response trying to bring it back into the most favourable configuration, minimising the free energy. This induces a net flux of energy, mass or momentum in the system. There are several ways to generate these fluxes. Applying an external force results in a net motion of the center of mass of the system. Such external forces can be pressure gradients or gravitational fields. There are other gradients or *thermodynamic "forces"*[1] (Prigogine [51] coined the term *affinities* for thermodynamic forces such as temperature, electric fields or chemical potentials, which do not have a net effect on the centre of mass in the bulk of a system. The thermodynamic forces are responsible for the thermo-, electro- and diffusio-osmosis (phoresis) respectively. In this section, we will introduce these concepts in the framework of non-equilibrium thermodynamics.

2.2.1 Entropy production

In the thermodynamics of irreversible processes, we assume a Local Thermal Equilibrium (LTE). This means that we can divide the entire spatial domain into sufficiently small subdomains or control volumes, where equilibrium still holds (i.e local thermodynamic relations are valid [52]). The total entropy S in a volume V is given by:

$$S(t) = \int_V d\mathbf{r}\, s_V(\mathbf{r},t)\ . \tag{2.5}$$

where $s_V(\mathbf{r},t)$ entropy per unit volume or entropy density. We expressed the entropy density conservation as

$$\frac{\partial s_V}{\partial t} + \boldsymbol{\nabla}\cdot\mathbf{J}_{s_V} = \sigma_s\ , \tag{2.6}$$

where $\mathbf{J}_{s_V}$ is the entropy flux. The local entropy production σ_s is generated by gradients in state variables, which are related to all the irreversible phenomena, such as the viscous interaction, heat conduction, diffusion and chemical reactions [53]. The rate of change due to the exchange of entropy with neighbouring regions is given by $\boldsymbol{\nabla}\cdot\mathbf{J}_{s_V}$.

Using Gibbs equation, we can express,

[1] In general, thermodynamic forces do not have the units of force. Rather, they are derived from the basic thermodynamic relation $dS = (1/T)dE - (P/T)dV + \sum(\mu_i/T)dN_i$. The basic thermodynamic "forces" are the gradients of $1/T$, P/T and μ_i/T and they are conjugate to heat, volume or particle fluxes. However, in applications, we often transform both forces and conjugate fluxes. The fluxes caused by thermodynamic forces counteract the driving forces and, in the process, result in entropy production.

$$T ds_V = dq - \sum_i^n \mu_i \, dc_i \, , \tag{2.7}$$

where c_i is the concentration of the species i and q is the heat per volume. Assuming LTE, therefore requiring that the spatial coordinates remain constant, we get

$$T \frac{\partial s_V}{\partial t} = \frac{\partial q}{\partial t} - \sum_i^n \mu_i \frac{\partial c_i}{\partial t} \, . \tag{2.8}$$

Similarly, we can express conservation equations for q and c_i:

$$\frac{\partial q}{\partial t} + \nabla \cdot \mathbf{J}_q = 0 \, , \tag{2.9}$$

$$\frac{\partial c_i}{\partial t} + \nabla \cdot \mathbf{J}_i = \sigma_i = \sum_j^r g_{ij} J_j \, , \tag{2.10}$$

where σ_i is the local production of component i per volume due to the chemical reactions r. It can be expressed in terms of the coefficients g_{ij} for the reaction j and J_j is the chemical reaction rate of reaction j. $\mathbf{J}_q$ and $\mathbf{J}_i$ are the fluxes of heat and particles of species i respectively. Using the results in Eq.(2.8) together with Eqs. (2.6), (2.9) and (2.10) we obtain that the local entropy generation is

$$\sigma_s = \mathbf{J}_q \cdot \nabla \left(\frac{1}{T} \right) + \sum_i^n \mathbf{J}_i \cdot \nabla \left(\frac{\mu_i}{T} \right) - \frac{1}{T} \sum_j^r A_j J_j \, , \tag{2.11}$$

where we defined the chemical affinity as $A_j = -\sum_i^n g_{ij} \mu_i$.

Eq.(2.11) holds for electrolytes replacing the chemical potential by the electrochemical potential. In general, we can express the entropy production as,

$$\sigma_s = \sum_\alpha \mathbf{J}_\alpha \mathbf{X}_\alpha \, , \tag{2.12}$$

where α runs over all the irreversible phenomena present in the system, $\mathbf{J}_\alpha$ is the flux of the quantity α and $\mathbf{X}_\alpha$ is the associated thermodynamic force.

Very often, one combination of fluxes and thermodynamic forces is more convenient than others. Different authors express the same irreversible phenomena with different equivalent representations. Therefore, one can define new fluxes $\mathbf{J}_\beta$, and consequently thermodynamic forces $\mathbf{X}_\beta$, such that the entropy generation remains invariant [51], this is:

$$\sigma_s = \sum_\alpha \mathbf{J}_\alpha \mathbf{X}_\alpha = \sum_\beta \mathbf{J}'_\beta \mathbf{X}'_\beta \, . \tag{2.13}$$

Furthermore, Onsager introduced an explicit way to express the linear dependence of the thermodynamic flows on the thermodynamic forces. These phenomenological laws are only valid close to equilibrium, i.e. in the linear regime where thermodynamic forces are small [54]. A few examples of these phenomenological laws are Fourier's, Fick's, and Ohm's laws. Hence, in a general manner,

$$\mathbf{J}_\alpha = \sum_\delta M_{\alpha\delta}\mathbf{X}_\delta \ . \tag{2.14}$$

where $M_{\alpha\delta}$ are phenomenological transport coefficients such as the thermal conductivity, diffusion coefficient, etc. The off-diagonal coefficients describe the coupling between the fluxes and are known as *coupling coefficients* or cross coefficients [52]. Notice that, by using Onsager's reciprocity theorem [53], there is an explicit relation between the phenomenological coefficients given by $M_{\alpha\delta} = M_{\delta\alpha}$, which offers a route to measuring transport coefficients while using different thermodynamic forces.

Elucidating the transformations in Eq. (2.13), we can express the new fluxes as a linear combination of the old ones $\mathbf{J}' = \mathbf{A}\cdot\mathbf{J}$ and similarly with the forces $\mathbf{X}' = \mathbf{B}\cdot\mathbf{X}$. Hence, we can transform the matrix of phenomenological coefficients $\mathbf{M}$ as

$$\mathbf{M}' = \mathbf{A}\cdot\mathbf{M}\cdot\mathbf{B}^{-1} \ . \tag{2.15}$$

2.3 Modelling across the scales

In a typical diffusiophoretic system, there is a broad hierarchy of scales as shown in Fig. 2.6. Ranging from the atomic scale, relevant for the solvents, solutes and the interface, to the hundreds of micrometres of a typical channel in microfluidics experiments [55]. While modelling, if we start from the bottom at the molecular scale, soon the problem becomes untraceable. The limited times produced with very expensive computations, will not be able to reproduce experimental observations. If we decide to coarse-grain the events near the interface and use a vague knowledge from the microscale to pose some boundary conditions for a continuum theory, we will miss the microscopic details and a clear understanding of the origin of phoresis.

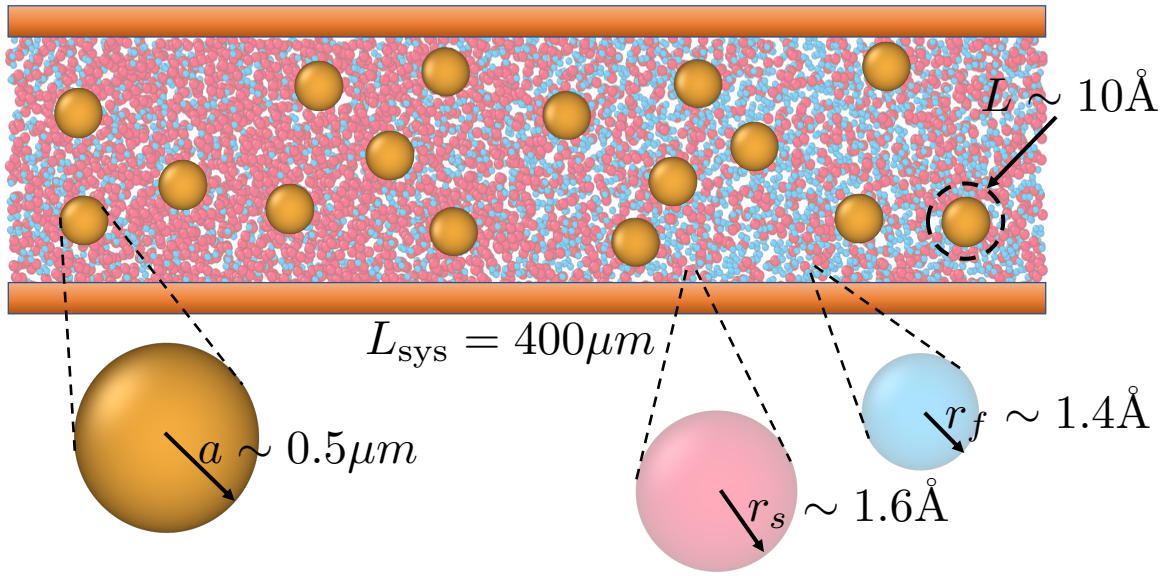

Fig. 2.6 Typical Length scales in a diffusiophoresis experimental setup. The channel length L_{sys}, colloidal particle radius a and solute typical radius r_s (estimated from the diffusivity) [55]. We assume water as solvent with radius r_f and the typical diffuse layer thickness L [16].

2.3.1 Continuum media

The continuum approach or the hydrodynamic limit arises when proper time and length scale separation is performed, averaging fast microscopic variables. As a result of this process, the large number of degrees of freedom, such as individual particles positions and velocities, reduce to a set of equations that depend solely on a few variables such as the velocity field, pressure, temperature and density. During this averaging process, a detailed description of the physical process is lost and is absorbed in the phenomenological parameters [33]. The hydrodynamic limit can be pushed to lower scales by a phenomenological extrapolation of the results to shorter wavelengths and higher frequencies [56]. This extension turns out to be valuable in the description of bulk properties. However, the hydrodynamic limit breaks down faster for interfaces, due to the inhomogeneity of the fluid close to the surface.

Governing equations

Theoretical approaches on diffusiophoresis treat the solution solvent-solute as a Newtonian fluid, into which a macroscopic particle is dispersed, and then make use of well-established non-equilibrium thermodynamics and continuum hydrodynamics treatments to work out the effect of solute gradients on the phoretic motion of the particle. Before going into the

details, it is necessary to introduce the governing equations of fluid dynamics, which emerge naturally from the conservation of mass, momentum and energy.

The continuity equation in the context of fluid dynamics refers to the mass conservation in the system that is expressed as follows (see Eq.(2.10)),

$$\frac{\partial \rho}{\partial t} + \boldsymbol{\nabla} \cdot \mathbf{v} = 0 \,, \tag{2.16}$$

where ρ is the mass density of the fluid and $\mathbf{v}$ fluid velocity.

If there is an incompressible fluid, then we obtain $\boldsymbol{\nabla} \cdot \mathbf{v} = 0$, which implies that if we try to deform a volume of fluid, it will reshape, but the volume will not vary. Moreover, if the fluid is transporting several i species, we express the continuity equation for the concentration of species i as:

$$\frac{\partial c_i}{\partial t} + \boldsymbol{\nabla} \cdot (c_i \mathbf{v}) - D_i \nabla^2 c_i = 0 \,, \tag{2.17}$$

where we suppose that the total flux $\mathbf{J}_i$ of species i has two components, diffusive and advective. The diffusive flux can be expressed by using Fick's law $\mathbf{J}_i^{\text{diff}} = D_i \boldsymbol{\nabla} c_i$ with D_i the diffusion constant of species i. The advective term expresses the coupling of the concentration with the fluid velocity field and it is given by $\mathbf{J}_i^{\text{conv}} = \mathbf{v} c_i$. Imposing momentum conservation, we can derive the Navier-Stokes (NS) equation

$$\rho \left[\frac{\partial \mathbf{v}}{\partial t} + \mathbf{v} \cdot \boldsymbol{\nabla} \mathbf{v} \right] = \boldsymbol{\nabla} \cdot \Pi + \mathbf{F}_{ext} \,, \tag{2.18}$$

with Π being the stress tensor or the momentum flux density tensor [57], given by

$$\Pi = \eta [\boldsymbol{\nabla} \mathbf{v} + (\boldsymbol{\nabla} \mathbf{v})^T - \frac{2}{3} \mathbf{I} (\boldsymbol{\nabla} \cdot \mathbf{v})] + [\zeta (\boldsymbol{\nabla} \cdot \mathbf{v}) - P] \mathbf{I} \,, \tag{2.19}$$

where P is the pressure, η is the shear viscosity, ζ is known as the bulk viscosity or volume viscosity that is related to the dissipation of energy occurring when there is an expansion or contraction of the fluid. The term $\frac{2}{3}\mathbf{I}(\boldsymbol{\nabla} \cdot \mathbf{v})$ was introduced to make the shear viscosity dependence traceless, this term could also be added to the dilatation term at the end $\zeta(\boldsymbol{\nabla} \cdot \mathbf{v})\mathbf{I}$. For low Reynolds numbers, the non-linear term $\mathbf{v} \cdot \boldsymbol{\nabla} \mathbf{v}$ can be neglected and NS becomes linear [58].

For transport in microfluidics systems, in addition to having small inertial terms compared to the typical viscous contributions (i.e. low Reynolds numbers). We can assume that the fluids are incompressible fluids. Hence, we can simplify the stress tensor,

$$\Pi = -p\mathbf{I} + \eta[\nabla\mathbf{v} + (\nabla\mathbf{v})^T] \,. \tag{2.20}$$

Therefore, Eq.(2.18) reduces to the Stokes equation,

$$\rho\frac{\partial\mathbf{v}}{\partial t} = \boldsymbol{\nabla}\cdot\Pi + \mathbf{F}_{ext} \,. \tag{2.21}$$

If we are dealing with Brownian time scales or stationary processes, the time derivative may be neglected and Stokes equation together with the incompressible mass conservation assumption are called *creeping flow* equations [58]. The main advantage of a continuum-medium approach is that it describes the phenomenology at time and length scales of typical microfluidic experiments. For instance, Montenegro-Johnson *et al.* [59] exploit the interfacial nature of diffusiophoresis to solve Stokes equations using the boundary element method. Since no quantities in the bulk are required to compute the velocity of phoretic particles, the method is fast compared to other numerical methods. In another application, Ault *et al.* [35] study the injection and withdrawal dynamics of colloidal particles into dead-end channels by using solute gradients. They simultaneously solve the (transient)diffusion-advection equations for solutes and colloids. The results are used to fit experimental data [25], thus obtaining the mobility and the time-dependent particle distributions with excellent agreement. Once the mobility is estimated, the zeta potential of both walls and particles can be inferred.

2.3.2 The mesoscopic scale: bridging between scales

Derjaguin's pioneer work and the subsequent theoretical improvements based on the same approach [14, 16, 60–63] use a continuum treatment of diffusiophoresis, where the solvent is treated as a continuum and only the concentration distribution of the solutes is included explicitly. This approach allows the inclusion of some microscopic details, such as the inhomogeneous distribution of solutes at the interface and its effective interaction with the object of interest. We will discuss these theoretical developments at length in the next chapters.

Concerning simulation methods, as we mentioned before, the biggest challenge in phoresis is to create a bridge for the length- and time-scale gaps between the solution and the particle undergoing phoresis. It would be ideal to perform full molecular dynamics to solve the complete set of equations of motions, although it is not feasible to reach the time scales required to study the wide range of practical applications. At the other extreme, we have continuum dynamics, with NS showing their successful and efficient approach to solve macroscopic problems, but lacking the detail of the microscopic approach, as thermal fluctuations which strongly influence the dynamics at the molecular level. From the need

of an intermediate scale, mesoscale models arise such as Dissipative Particle Dynamics (DPD) [64], Stochastic Rotation Dynamics (SRD) (also known as Multiparticle collision dynamics (MPC) [65]) or Lattice Boltzmann Method (LBM) [66]. These techniques capture the essential features of the solvent. They offer alternative ways of solving the NS equations, expressed as local conservative laws of mass, momentum and energy with some additional aspects of the microscopic detail [67]. However, they require explicit boundary conditions for the velocity of the solvent at the particle surface. Such conditions are slip and non-slip boundaries modelled as specular reflections or bounce back operations respectively. These two conditions are not enough to account for the velocity enhancement at the interface that can be “up to two orders of magnitude" [68].

There have been some attempts to model diffusiophoresis using MPC, mainly consisting of a moving object in a binary solution. One way of including the interfacial effect is by creating explicit gradients and having a hybrid MD-MPC [29, 31, 34], such that the interactions between the different species of solution particles and the body subject to phoresis are included. Another alternative is to modify the boundary conditions, including a new *phoretically osmotic* boundary condition [69], which gives solution particles either a slip or a non-slip boundary condition, depending on the species. This produces an unbalanced tangential force at the boundary which drives the phoretic motion. In this framework, the strength of the diffusiophoretic effect is tuned by changing the fluid-particle boundary potential interaction range.

2.3.3 Microscopic

The hydrodynamics of fluid films thicker than $10-20$ atomic sizes can be described by following a continuum approach using a slip boundary condition [70]. However, in order to estimate the magnitude of the velocity at the boundary, or slip velocity v^B, a deeper understanding of the interfacial region is required. This inhomogeneous region is where the phoretic transport occurs and the hydrodynamic limit breaks down. Furthermore, the surface effects occur at much larger scales than the bulk deviations from continuum expectations [33].

To model the diffusiophoretic movement from a microscopic perspective we can use classical Molecular Dynamics (MD). This technique allows for a detailed study of the interactions in the diffusive layer by using a deterministic approach. Thus, the equations of motion for all the particles in the system are integrated by using schemes such as Verlet or Leapfrog [71], which are time reversible and have a unitary evolution in phase space. We refer to classical MD as we are not calculating the interaction between particles starting from their electronic structure. Instead, we use van der Waals type interactions and we can

include Coulombic effects to deal with electrolytes. To summarise, the entire idea behind MD is to sample microscopic quantities every certain threshold to avoid correlation between measurements and then use statistical mechanics to create a link between the microscopic degrees of freedom and the thermodynamic/hydrodynamic properties. In the next section, we discuss the details of MD simulations in diffusio-osmosis(phoresis).

There are some applications on microscopic simulations using an explicit solvent to study diffusio-osmosis(phoresis). An early attempt to investigate diffusio-osmosis using MD simulations was performed by Adjari & Bocquet [68]. The authors modelled a binary solution interacting with a solid wall and measured the diffusio-osmotic transport coefficients indirectly by applying a pressure gradient and measuring the solute excess flux. More recently, a small number of authors revisited the same type of system using both equilibrium and non-equilibrium MD [27, 72, 48, 73]. Finally, applications on diffusiophoresis have focused on colloids [62, 74] and short polymers [75].

2.4 Molecular Dynamics

In this section, we describe the essence of the existing MD algorithms to study diffusio-osmosis(phoresis). As these phenomena are inherently out of equilibrium, the main focus will be on Non-Equilibrium Molecular Dynamics (NEMD). In what follows, we employ the most common integration algorithms, thermostats and some auxiliary techniques as Monte Carlo (MC) that will be mentioned regularly and are extensible described elsewhere [76, 77, 71, 44].

2.4.1 Equilibrium Molecular Dynamics

Although phoresis occurs in systems out of equilibrium, it is still possible to estimate transport coefficients using linear response theory (see Appendix B). Yoshida *et al.* [27] followed by Mangaud *et al.* [73] utilised this approach to estimate diffusio-osmotic mobilities by computing Green-Kubo relations. Furthermore, as this approach is limited to close-to-equilibrium systems, they were able to show that the transport matrix is symmetrical, following Onsager's reciprocity.

EMD is also used for the analytical estimations of mobilities based on continuum theories. These estimations depend on equilibrium quantities, such as the concentration distribution of species at the interface. Therefore, short EMD runs are sufficient to compute the theoretical expressions and this will be discussed in each one of the applications in the following chapters.

2.4.2 Non-Equilibrium Molecular Dynamics

The underlying idea of NEMD is to try to reproduce as close as possible what happens in real experiments under the influence of thermodynamic forces. This is, applying a driving force that keeps the system out of equilibrium to measure the resultant flux. In the context of diffusion simulations, there are three techniques used to simulate concentration gradients. The first one, Gradient Relaxation Molecular Dynamics (GRMD) [78], consists in creating two independent simulation boxes, *parent boxes*, at different concentrations using MC followed by additional NVT-MD equilibration steps. The parent boxes are then joined to create a *parent cell* with a step concentration distribution along the x-axis (see Fig. 2.7) that equilibrates while the transient concentration distribution is sampled to find the diffusivities. This technique is not suitable for our purpose because the transient nature of the gradient does not allow gathering enough statistics to sample the quantities of interest.

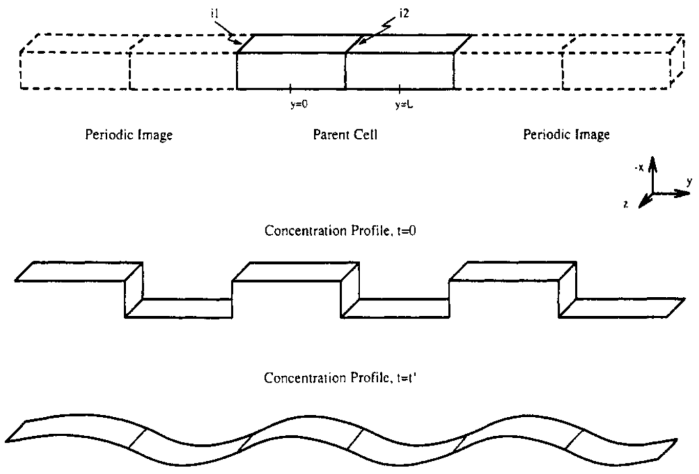

Fig. 2.7 Schematic representation of the Gradient Relaxation MD box [78]. The parent cell is formed by two independently equilibrated boxes with different homogeneous concentrations. The concentration profiles at $t = 0$ and a (transient) concentration distribution at a later time $t = t'$ are shown at the bottom.

The additional two methods are called Boundary-Driven (BD-NEMD) and External-Field (EF-NEMD) or Field-Driven (FD-NEMD) and they will be discussed in more detail below. In short, BD-NEMD is more intuitive and close to real experiments. It consists of creating two separated reservoirs in the simulation box where quantities as energy, momentum or concentrations are fixed but with different values for each reservoir. The gradient in one of the specific quantities induces a flux that brings the system to a non-equilibrium steady state. FD-NEMD can be seen as a small portion of the BD-NEMD simulation box in which there is an homogeneous distribution of the state variable. The lack of an explicit gradient

is compensated by applying an external force on each particle that mimics the influence of the thermodynamic force. In Fig. 2.8, we show the connection between BD-NEMD and FD-NEMD simulations of bulk diffusion.

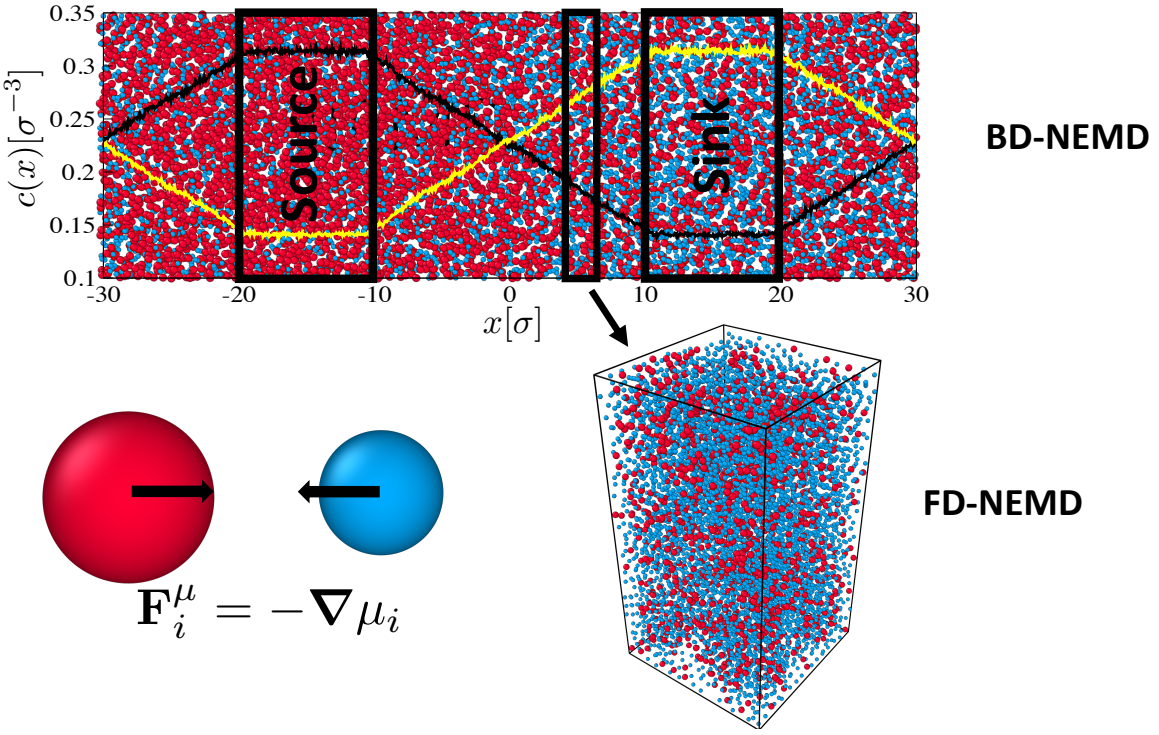

Fig. 2.8 Bulk diffusion in an ideal binary solution at constant temperature and pressure. We show a BD-NEMD simulation box with *source* and *sink* regions where we impose a high and a low concentration of red particles, respectively. The FD-NEMD box can be assumed as a new simulation box in the same thermodynamic state as a small region in LTE from the BD-NEMD simulation. As the new box has a homogeneous concentration, a force representing the effect the chemical potential gradient is applied to each particle.

Boundary-Driven Non-equilibrium Molecular Dynamics

Probably, the most intuitive way of imposing a chemical potential gradient in a simulation is to explicitly create two reservoirs in the simulations separated by a transport region as shown in Fig. 2.8. The condition, in this case, the concentrations at the boundary of the transport region, define the flux within, thus the name "boundary-driven". The first simulations of systems experiencing chemical potential gradients in the context of diffusion were developed almost simultaneously by Heffelfinger and van Swol [79] and MacElroy [80]. The former authors called the method Dual Control Volume Grand Canonical Molecular Dynamics (DCV-GCMD), as it consists of two grand canonical MC (GCMC) control volumes or reservoirs embedded in an MD-NVT simulation box. The GCMC serves to keep the desired

concentration in the reservoirs. The molecules flow between the two control volumes, from the *source* at high concentration to the *sink* at a lower concentration. Replenishing the particles in the reservoirs at the right rate generates a steady-state flux of particles. This step is critical, as it may give incorrect results if the MC/MD frequency is not large enough [79, 81, 82]. The tuning depends on the size of the reservoirs, the distance between them and the number of GCMC insertion/deletion attempted per MC step.

In principle, BD-NEDM represents what happens in real experiments and is inherently inhomogeneous. This is ideal to simulate microscopic inhomogeneous systems such as the flow through nanoscopic films [83]. However, in practice, the method has many disadvantages. As discussed before, it is difficult to tune the parameters to set up the initial concentration profile. Moreover, the use of GCMC implies that the velocity of the inserted particles must be known a priori and the method will fail for fluid mixtures with large size ratio [83]. The magnitude of the gradient can lead to simulations occurring outside the linear response regime [81]. Finally, the simulations are expensive as they must explicitly include the reservoirs, and there is an overhead associated with the MC insertion/deletions.

Field-Driven Non-Equilibrium Molecular Dynamics

Simulations using FD-NEMD require the introduction of mechanical constraints on each particle, an external field mimicking the effect of a thermodynamic force. In general, this *synthetic* constraint has no clear physical interpretation, but its mechanical nature facilitates the simulation [84] .

This approach has been applied in many contexts [85], with the body force coupling to particle variables such as the mass or the charge [44]. In the case of diffusion, Maginn *et al.* [78] performed *colour field* NEMD, in which particles are assigned colour charges according to their chemical identity. In this way, they replaced the chemical potential gradient by an equal (but opposite) *colour force*.

In practice, when the synthetic field is applied through the simulation, the particles obey modified equations of motion [83], generating a steady flux in a system without an explicit gradient. As the forces do not depend on the position, the simulation remains homogeneous in the direction of the gradient and is therefore compatible with periodic boundary conditions and less prone to finite size-effects. It is worth pointing out that special care is required as the external force inevitably produces heat. Hence, suitable thermostats as the Gaussian isokinetic [86] or Nosé-Hoover [87] are used, both giving identical steady-state predictions of material properties [44]. These thermostats also solve a common problem that arises when large fields are applied, namely the string-phase separation [85] or the *traffic lanes* effect [88]. This non-equilibrium phase separation arises because there is a free energy advantage

to partially separate the system to reduce the effective friction between molecules of different species.

Arya *et al.* [81] highlight that “this method has not been widely used, perhaps because the equivalence of such a homogeneous external forcing function that drives diffusion and an actual chemical potential gradient has not been formally demonstrated". Subsequently, Yoshida *et al.* [27] demonstrated based on linear response theory that this is indeed the case and that the Onsager reciprocity relations for phoretic transport follow if the imposed gradients are replaced with a constant colour-force field (see Sec. 3.2.3).

There is another method to determine the microscopic forces acting on the individual particles based on the stress tensor. This method was first introduced by Han *et al.* [45] and then applied in simulations of diffusio-osmosis and Marangoni effect by Liu *et al.* [48, 72]. Also, in thermo-osmosis by Ganti *et al.* [89]. The method allows the computation of the force per fluid volume from the gradient of the microscopic pressure tensor at a position z from a solid wall as:

$$\mathbf{f}^V(z) = -\frac{\partial P^{xx}(z)}{\partial c_i^B}\frac{\partial c_s^B}{\partial x}\,, \tag{2.22}$$

where c_i^B is the concentration of species i in the bulk. Using centred finite differences and assuming that the concentration gradient is small, we can approximate Eq.(2.22) to

$$\mathbf{f}^V(z) = -\frac{P^{xx}(c_i^B + \Delta c_i^B) - P^{xx}(c_i^B - \Delta c_i^B)}{2\Delta c_i^B}\nabla c_i^B;. \tag{2.23}$$

Therefore, instead of computing the stress gradient from NEMD, two independent equilibrium simulations at different concentrations are required to measure the pressures in Eq. (2.23).

This method seemed promising, however, there is a subtlety worth considering: the definition of the microscopic stress tensor is not unique, as the only restriction on it is $\boldsymbol{\nabla}\cdot\Pi = 0$. This generates different estimates for the force and ultimately different velocities.

To summarise, the advantages that FD-NEMD offers over BD-NEMD are that it allows the simulation of moving objects inside a chemical potential gradient under periodic boundary conditions and a homogeneous simulation box compatible with LTE. The simulations require fewer computational resources, as their system sizes are considerably smaller, and there is no overhead caused by MC movements. Once the diffusive layer equilibrates, the imposition of chemical potential gradients requires the modification of an input parameter rather than the re-definition of the reservoirs in BD-NEMD. The latter feature allows for the examination of both linear and non-linear responses.

Chapter 3

Diffusio-osmosis

"God made the bulk; surfaces were invented by the devil."

Wolfgang Pauli

3.1 Introduction

As described in Chapter 2, concentration gradients in bulk fluid cannot cause fluid flow. However, a gradient in the chemical potential of the various components in a fluid mixture can cause a net hydrodynamic flow in the presence of an interface that interacts differently with the different species in the solution. Such a flow, induced by chemical-potential gradients, is known as diffusio-osmosis. We can describe the theory of diffusio-osmotic flow in a mixture of uncharged species. This discussion is easily extended to an electrolyte solution, as the forces acting on charges can be accounted for by adding electrostatic potential energies to the chemical potentials [45], i.e. by replacing the chemical potential by the electrochemical potential. The analogies between both phenomena were discussed in the pioneering work of Derjaguin [90], who stressed the analogy between solute and charge excess, and between chemical potential gradients and electric fields.

Several numerical studies on diffusio-osmosis have been conducted in recent years, from computations of the transport coefficients using the Green-Kubo formalism in EMD simulations [68, 27, 73], to attempts to relate the microscopic forces to stress gradients [48].

The present chapter introduces most of the concepts used and extended in this thesis. The text is organised in the two following sections: Sec 3.2 presents a framework to study diffusio-osmosis/phoresis starting from Non-Equilibrium Thermodynamics. We introduce the relevant quantities associated with the excess of species at the interface and find a connection

between the transport coefficients using Onsager's formalism. In Sec 3.3, we present a benchmark simulation that we use, in order to highlight certain subtleties that are often glossed over in the literature.

3.2 Theory

3.2.1 Diffusio-osmotic entropy generation

To illustrate the theoretical description of diffusio-osmosis we consider a n-component fluid in contact with a solid surface, as shown in Fig. 3.1. The only thermodynamic forces acting on the system are the chemical potential gradients of each species i, $\nabla\mu_i$. Usually, the fluid can be divided into two regions: the bulk, where the fluid can be considered homogeneous, and the vicinity of the (solid-liquid) interface, where the concentration of the different species at a distance z from the interface, $c_i(z)$, differs from its bulk value. This heterogeneity decays as the distance from the surface increases until the bulk concentration is reached. We aim to find an expression for the entropy production for this system, as the entropy production is the crucial quantity required to define a consistent set of fluxes and thermodynamic forces in the context of Onsager's theory (see Sec 2.2).

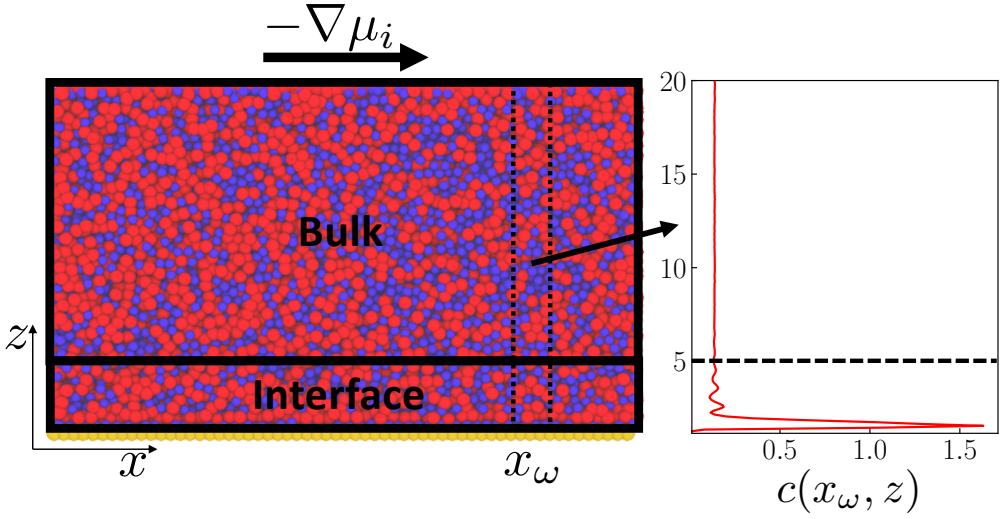

Fig. 3.1 A diffusio-osmotic system composed of a n-component solution (only two are shown) and a solid surface. The fluid is divided into two regions: bulk, where the concentration of the fluid $c(x,z)$ is independent of z, and the interface, where the fluid is heterogeneous, even in the absence of imposed concentration gradients. We consider the case that the gradient of the chemical potential ($\nabla\mu_i$) is along the x-direction. A typical z-dependent density profile ($c(x_\omega,z)$) of the fluid at a position x_ω is shown in the right-hand panel of the figure.

We start from the expression for the entropy production (Eq. (2.11)) with no temperature gradient nor chemical reactions,

$$\Phi = T\sigma_s = \sum_{i=1}^{N} \mathbf{J_i} \cdot (-\boldsymbol{\nabla}\mu_i) \, . \tag{3.1}$$

Here Φ is the dissipation function as defined by Lord Rayleigh. It has units of energy density per unit of time, as it represents the dissipation of energy by an irreversible process in a control volume [91]. The gradient in the chemical potential can be expressed as

$$\boldsymbol{\nabla}\mu_i \equiv (\boldsymbol{\nabla}\mu_i)_{P,T} + \left(\frac{\partial \mu_i}{\partial P}\right)_{c_j,T} \nabla P \, , \tag{3.2}$$

where c_j indicates that the derivative is evaluated at constant concentration of the additional $n-1$ species with $j \neq i$. Additionally, we know that

$$\left(\frac{\partial \mu_i}{\partial P}\right)_{c_j,T} = v_i \, , \tag{3.3}$$

with v_i being the partial molar volume of species i. Therefore, we can formulate the dissipation function as

$$\Phi = \left(\sum_{i=1}^{n} \mathbf{J_i} v_i\right) \cdot (-\boldsymbol{\nabla} P) + \sum_{i=1}^{n} \mathbf{J_i} \cdot (-\boldsymbol{\nabla}\mu_i)_{P,T} \, . \tag{3.4}$$

The total volume flux in the system $\mathbf{Q}$ is defined as

$$\mathbf{Q} \equiv \sum_{i=1}^{n} v_i \mathbf{J}_i \, , \tag{3.5}$$

which is the average volume flow velocity in the system. We can then express the dissipation function as

$$\Phi = \mathbf{Q} \cdot (-\boldsymbol{\nabla} P) + \sum_{i=1}^{n} \mathbf{J_i} \cdot (-\boldsymbol{\nabla}\mu_i)_{P,T} \, . \tag{3.6}$$

From an experimental point of view, the expression in Eq. (3.6) is useful as it separates the fluid flow from the diffusive fluxes (that are Galilei-invariant). At this point we can use the Gibbs-Duhem relation,

$$V dP = \sum_{i=1}^{n} N_i \, d\mu_i \, , \tag{3.7}$$

where N_i is the number of particles of species n. We can rewrite Eq. (3.7) as:

$$\boldsymbol{\nabla} P = \sum_{i=1}^{n} c_i \, \boldsymbol{\nabla} \mu_i \; . \tag{3.8}$$

Eq. (3.8) establishes a general relation between the thermodynamic forces in the system, but we have not made a distinction between bulk and interfacial region yet. If we choose $(\boldsymbol{\nabla}\mu_i)_{P,T}$ in Eq. (3.6) as the independent driving forces then $\boldsymbol{\nabla} P$ is fixed. Conversely, if we use $\boldsymbol{\nabla} P$ as a driving force, then one of the $(\boldsymbol{\nabla}\mu_i)_{P,T}$ is linearly dependent on the others. For instance, we can express the solvent chemical potential $(\boldsymbol{\nabla}\mu_f)_{P,T}$ using Gibbs-Duhem in the *bulk* as,

$$(\boldsymbol{\nabla}\mu_f)_{P,T} = -\sum_{i=1}^{n-1} \frac{c_i^B}{c_f^B} (\boldsymbol{\nabla}\mu_i)_{P,T} \; . \tag{3.9}$$

Note that the pressure that is held constant in Eq. (3.9) should be the *bulk* pressure [53, 52], and the concentrations must be in the bulk. When the pressure in the bulk fluid is constant, the presence of chemical potential gradients can still cause a pressure gradient at an interface.

We can now write the dissipation function, which depends on $n-1$ chemical-potential gradients and on the pressure gradient as:

$$\Phi = \mathbf{Q} \cdot (-\boldsymbol{\nabla} P) + \sum_{i=1}^{n-1} \left(\mathbf{J}_i - \frac{c_i^B}{c_f^B} \mathbf{J}_f \right) \cdot (-\boldsymbol{\nabla}\mu_i)_{P,T} \; . \tag{3.10}$$

In what follows, we restrict the analysis to a two component system, with solvent f and solute s. The dissipation function then becomes

$$\Phi = \mathbf{Q} \cdot (-\boldsymbol{\nabla} P) + \mathbf{J}_s' \cdot (-\boldsymbol{\nabla}\mu_i)_{P,T} \; , \tag{3.11}$$

where we have defined the excess flux of solute as

$$\mathbf{J}_s' = \mathbf{J}_s - \frac{c_s^B}{c_f^B} \mathbf{J}_f \; . \tag{3.12}$$

Finally, we can write the transport matrix connecting the fluxes with the thermodynamic forces,

$$\begin{bmatrix} \mathbf{Q} \\ \mathbf{J}_s' \end{bmatrix} = \begin{bmatrix} M_{QQ} & M_{QJ} \\ M_{JQ} & M_{JJ} \end{bmatrix} \begin{bmatrix} -\boldsymbol{\nabla} P/T \\ -\boldsymbol{\nabla}\mu_s/T \end{bmatrix} \tag{3.13}$$

By including the factor $1/T$ in the thermodynamic forces, we can cast the entropy production in a simple bi-linear form in fluxes and thermodynamic forces. Such form is needed to derive

the Onsager reciprocity relations for the transport coefficients $M_{\alpha\beta}$. In practice, the factor $1/T$ is often absorbed in the transport coefficients - but it would be unwise to do so if the symmetry property of the transport matrix is made explicit.

3.2.2 Local Thermodynamic Equilibrium and the Derjaguin-Anderson theory for diffusio-osmosis

Again, we consider the system in Fig. 3.1. The mixture is at a constant temperature and, we assume a chemical potential gradient of species i in the x-direction. If the bulk fluid is incompressible, the speed of sound is “infinite". Hence, the density/pressure equilibrate instantaneously in the bulk. Moreover, the rate of the spontaneous decay of chemical potential gradients over a distance ℓ scales as ℓ^2/D_i (D_i denotes the diffusion coefficient of species i). As a consequence, chemical potential differences across the boundary layers equilibrate very quickly compared to the time scale of the diffusio-osmotic flow. Therefore, we can employ LTE, assuming that the system is in equilibrium in the z-direction, even though a chemical potential gradient can be maintained along the x-direction. Hence, we can write the relation between the thermodynamic forces in the bulk from Eq.(3.8) as:

$$\frac{\partial P_{xx}^B}{\partial x} = 0 = \sum_{i=1}^{n} c_i^B \left(\frac{\partial \mu_i}{\partial x}\right) , \tag{3.14}$$

where P_{xx} refers to a component of the pressure tensor parallel to the surface. At the interface, the density profile $c_i(z)$ depends on z. The fact that $\mu = \mu^{\text{exc}}(z) + k_B T \ln c_i(z)$ is constant across the diffusive boundary layer (and for a fixed x) implies that the excess chemical potential μ^{exc} will, in general, depend on the distance z from the wall.

At a point z within the diffusive boundary layer we can write,

$$\frac{\partial P_{xx}(z)}{\partial x} = \sum_{i=1}^{n} [c_i(z) - c_i^B] \left(\frac{\partial \mu_i}{\partial x}\right) . \tag{3.15}$$

It is important to stress that mechanical forces in liquids can only be caused by body forces such as gravity or by pressure gradients [89]. The reason why chemical potential gradients near a surface cause fluid flow is that they induce a pressure gradient near a wall. It is the pressure gradient in Eq. (3.15) which moves the fluid.

As the chemical potential μ is constant, we can relate the concentrations in the bulk ($z \to \infty$) and close to the surface as

$$c_i(z) e^{\beta(\mu_i^{\text{exc}}(z))} = c_i^B e^{\beta(\mu_i^{\text{exc}}(\infty))} , \tag{3.16}$$

thus, we can rewrite Eq.(3.15),

$$\frac{\partial P_{xx}(z)}{\partial x} = \sum_{i=1}^{n} c_i^B [e^{-\beta \Delta \mu_i^{\text{exc}}(z)} - 1] \left(\frac{\partial \mu_i}{\partial x} \right) . \tag{3.17}$$

where $\Delta\mu_i(z)^{\text{exc}} = \mu_i^{\text{exc}}(z) - \mu_i^{\text{exc}}(\infty)$ is the excess chemical potential due to the presence of the interface. We can now combine Eq. (3.17) with the Stokes equation in Eq. (2.18) to estimate the flow velocity in the x direction:

$$\eta(z) \frac{\partial^2 v_x(z)}{\partial z^2} = \frac{\partial P_{xx}(z)}{\partial x} . \tag{3.18}$$

Assuming a constant viscosity η, we get

$$v_x(z) = -\frac{1}{\eta} \int_0^z dz' \int_{z'}^{\infty} dz'' \sum_{i=1}^{n} c_i^B [e^{-\beta \Delta \mu_i^{\text{exc}}(z)} - 1] \left(\frac{\partial \mu_i}{\partial x} \right) . \tag{3.19}$$

Using non-slip boundary conditions, and exploiting the fact that outside the diffuse layer, the velocity does not vary, we obtain the bulk velocity of the fluid v_B,

$$v_x(z \to \infty) = v_x^B = -\frac{1}{\eta} \int_0^{\infty} dz z \sum_{i=1}^{n} c_i^B [e^{-\beta \Delta \mu_i^{\text{exc}}(z)} - 1] \left(\frac{\partial \mu_i}{\partial x} \right) \tag{3.20}$$

Notice that in fluid dynamics, the slip velocity is usually defined as the velocity at the interface where the boundary condition is imposed. However, in the present case, using a local continuum description, the slip velocity v_x^B is the fluid velocity in the bulk just outside the diffuse layer.

In the following part of this section, we will show how Derjaguin-Anderson's description of diffusio-osmosis [14, 92] can be written as a special case of Eq. (3.20). For an ideal solution in the bulk, we have that

$$\frac{\partial \mu_i}{\partial x} = \frac{k_B T}{c_i^B} \frac{\partial c_i^B}{\partial x} . \tag{3.21}$$

Thus, we can write Eq. (3.20) as,

$$v_x^B = -\frac{k_B T}{\eta} \int_0^{\infty} dz z \sum_{i=1}^{n} [e^{-\beta \Delta \mu_i^{\text{exc}}(z)} - 1] \left(\frac{\partial c_i^B}{\partial x} \right) . \tag{3.22}$$

Moreover, we restrict the analysis to a very dilute solution of discrete solute molecules s in a continuum liquid phase (solvent f),

$$v_x^B \approx -\frac{k_B T}{\eta} \int_0^{\infty} dz z [e^{-\beta \phi(z)} - 1] \left(\frac{\partial c_s^B}{\partial x} \right) , \tag{3.23}$$

where we neglected the solvent contribution as $e^{-\beta\Delta\mu_i^{\text{exc}}(z)} \propto 1/c_i^B$ and $c_s^B \ll c_f^B$. Additionally, we defined $\phi(z) \equiv \Delta\mu_i^{\text{exc}}(z)$. In Derjaguin-Anderson theory $\phi(z)$ is the potential mean-field felt by the solutes at a distance z from the solid surface. This potential does not only include the direct effect of the surface on the solutes, it also accounts for the interaction with the solvent and other solutes. Therefore, $\phi(z)$ only vanishes at the bulk region, where the presence of the interface does not perturb the fluid anymore.

The original Derjaguin-Anderson theory did not consider the atomistic nature of the liquid mixture. The use of a continuum description of the solvent in this approach is not surprising, as no reliable theory of dense liquids existed at the time and as there were no simulation data. However, at present, we can use molecular simulations (MD/MC) to compute all the parameters in Eq. (3.20).

The applicability of the framework described in this section might be questioned for thin boundary layers of the order of 10Å [33]. Nevertheless, as was discussed in Sec. 2.1.1, a thermodynamic picture arrives at the qualitatively correct prediction that a solute gradient along an interface, be it flat or curved, can induce fluid flow.

The interaction of the fluid particles with the wall may create layering at the interface, as shown in Fig. 3.1. To quantify whether the net effect of this layering is an accumulation or depletion of particles near the surface, we use Gibbs's definition of the surface excess for particles of species i as (see [16]):

$$\Gamma_i = \int_0^\infty [c_i(z) - c_i^B] dz \,. \tag{3.24}$$

Γ_i is positive if there is net adsorption of particles on the wall, and negative in the case of depletion at the interface. Next, we relate the so-called solute *adsorption-length* K_i to the zeroth moment of the excess-concentration profile:

$$K_i = \int_0^\infty \left(\frac{c_i(z) - c_i^B}{c_s^B} \right) dz \,. \tag{3.25}$$

K_i can be interpreted as the thickness (positive or negative) of a layer of bulk solution that would contain the same net number of adsorbed or depleted particles. K_i is obtained experimentally by equilibrium adsorption studies and it could be as large as 1 μm [16], or much larger near a wetting transition.

A second measure of the adsorption/depletion layer is given by ξ_i (a length squared). ξ_i is related to the first moment of the excess concentration:

$$\xi_i \equiv \int_0^\infty \frac{\left(c_i(z) - c_i^B\right)}{c_i^B} z\, dz \,. \tag{3.26}$$

Derjaguin defined the characteristic extension of the diffuse adsorption layer as $\sqrt{\xi_i}$ [93], and Anderson defined the characteristic length L_i^* [1]:

$$L_i^* \equiv \frac{\xi_i}{K_i} \,. \tag{3.27}$$

Using the above definitions, we can rewrite the diffusio-osmotic velocity in Eq. (3.23)

$$v^B = -\frac{\alpha}{\beta\eta} K_s L_s^* \,, \tag{3.28}$$

where α is the concentration gradient of solutes in the bulk. Note that even when there is strong net adsorption of solutes (large K_s), L_s^* may be small, zero, or even of the opposite sign, depending on $(c_s(z) - c_s^B)$. In other words, diffusio-osmotic flow is least sensitive to the excess concentration closest to the wall. This effect becomes even more pronounced when there is strong adsorption on the wall, leading to a local increase in the viscosity.

3.2.3 Transport coefficients

To compute the transport coefficients $M_{\alpha\delta}$ (see Sec. 2.2.1) using FD-NEMD, we need to represent the thermodynamic forces as fictitious mechanical forces that can be incorporated in the Hamiltonian of the system and can act on the particles in the fluid. In this section, we employ linear response theory to show that such an approach is valid and fulfills Onsager's symmetry relations.

We consider a system with N interacting particles satisfying Hamiltonian equations of motion:

$$\dot{\mathbf{r}}_i = \frac{\mathbf{p}_i}{m_i} \,, \tag{3.29}$$

$$\dot{\mathbf{p}}_i = \mathbf{F}_i + \mathbf{F}_{ext} \,, \tag{3.30}$$

where $\mathbf{F}_i$ is the force exerted by all the other particles on particle i and $\mathbf{F}_{\text{ext}}$ is the mechanical equivalent of the thermodynamic force. The Hamiltonian can be written as

$$\mathscr{H} = \mathscr{H}_0 + \mathscr{H}_{\text{ext}} \,. \tag{3.31}$$

For the diffusio-osmotic case, we now represent all chemical potential gradients by equivalent forces $\mathbf{F}_i^{\mu}$ on every particle of species i. Note that (in a periodic system) these forces cannot be viewed as the gradient of a potential. To satisfy the condition of mechanical equilibrium

[1] Anderson's definition can give unphysical results when $K_i \to 0$, while $\xi_i \neq 0$.

in the bulk, if we apply a microscopic force $\mathbf{F}_s^\mu$ on the solutes, we also need to exert an equivalent force on the solvent particles $\mathbf{F}_f^\mu$, such that:

$$\mathbf{F}_{\text{ext}}^B = 0 = \mathbf{F}_s^\mu N_s^B + (N^B - N_s^B)\mathbf{F}_f^\mu \,, \tag{3.32}$$

where N^B and N_s^B are the total number of particles and the number of solute particles in the bulk. Eq. (3.32) is the mechanical equivalent of the Gibbs-Duhem equation.

Expressing everything in terms of the external force on the solutes

$$\mathbf{F}_{\text{ext}}^B = \left[N_s^B - \frac{N_s^B}{N^B - N_s^B}(N^B - N_s^B) \right] \mathbf{F}_s^\mu = 0 \,. \tag{3.33}$$

The Hamiltonian coupling of the particles to the external driving forces is

$$\mathscr{H}_{\text{ext}} = \left[\sum_{i\in s}^{B} \mathbf{x}_i - \frac{N_s^B}{N^B - N_s^B} \sum_{i\in f}^{B} \mathbf{x}_i \right] \cdot \mathbf{F}_s^\mu \,. \tag{3.34}$$

It is worth pointing out that all the sums in Eq. (3.34) are in the bulk B. Next, we consider a system confined in a slit. The total volume of the fluid Ω includes an interfacial region. The previous expression is still valid, giving rise to the diffusio-osmotic flow, as now there is a non-vanishing contribution from the externally applied forces $\mathbf{F}_{\text{ext}}$

$$\mathscr{H}_{\text{ext}} = \left[\sum_{i\in s}^{\Omega} \mathbf{x}_i - \frac{N_s^B}{N^B - N_s^B} \sum_{i\in f}^{\Omega} \mathbf{x}_i \right] \cdot \mathbf{F}_s^\mu \,. \tag{3.35}$$

From linear response theory (see Appendix B), we can compute the response of a given observable B to an external perturbation of the form $\Delta\mathscr{H} = A(x_i)F_0 = \mathscr{H}_{\text{ext}}$ as

$$< B >= L_{AB}F_0 = \left[\frac{1}{k_B T} \int_0^\infty < B(t)\dot{A}(0) > dt \right] F_0 \,. \tag{3.36}$$

Focusing on the non-diagonal terms of the transport matrix on Eq. (3.13), when a chemical potential gradient is applied, the observable we want to measure is the total flux of the particles $\mathbf{Q}$

$$B = \mathbf{Q}^\Omega = \frac{1}{N^\Omega} \sum_{i\in\text{all}}^{\Omega} \dot{\mathbf{x}}_i \,. \tag{3.37}$$

It is convenient to write the variable that couples to the external field as

$$\begin{aligned}\dot{A} &= \sum_{i\in s}^{\Omega}\dot{\mathbf{x}}_i - \frac{N_s^B}{N^B-N_s^B}\sum_{i\in f}^{\Omega}\dot{\mathbf{x}}_i \\ &= V^{\Omega}\left(\frac{1}{V^{\Omega}}\sum_{i\in s}^{\Omega}\dot{\mathbf{x}}_i - \frac{c_s^B}{c_f^B}\frac{1}{V^{\Omega}}\sum_{i\in f}^{\Omega}\dot{\mathbf{x}}_i\right) \\ &= V^{\Omega}\left(\mathbf{J}_s^{\Omega} - \frac{c_s^B}{c_f^B}\mathbf{J}_f^{\Omega}\right) .\end{aligned}$$

Finally, using Eq. (3.36) we can express the total volume flux as

$$\begin{aligned}\mathbf{Q}^{\Omega} =< \mathbf{Q}^{\Omega} > &= \left[\frac{V^{\Omega}}{k_BT}\int_0^{\infty} < \mathbf{Q}^{\Omega}(t)(\mathbf{J}_s^{\Omega} - \frac{c_s^B}{c_f^B}\mathbf{J}_f^{\Omega})(0) > dt\right]\mathbf{F}_s^{\mu} \\ &= M_{QJ}\frac{\mathbf{F}_s^{\mu}}{T} .\end{aligned} \tag{3.38}$$

Hence, using transport equations in Eq.(3.13), we can establish the connection between the thermodynamic force and its microscopic counterpart as

$$\boldsymbol{\nabla}\mu_s = -\mathbf{F}_s^{\mu} . \tag{3.39}$$

Eq. (3.39) is general (i.e. it is valid for arbitrary forces). However, the Green-Kubo expression in Eq. (3.36) is only valid in the linear regime. Moreover, the expression for the entropy production (Eq. (3.13)) assumes that the fluxes are linear functions of the thermodynamic forces.

Let us focus on the excess of solutes $\mathbf{J}_s'$ and transform it into an equivalent flux appearing in the literature [27, 73].

$$\mathbf{J}_s'^{\Omega} = \mathbf{J}_s^{\Omega} - \frac{c_s^B}{c_f^B}\mathbf{J}_f^{\Omega} = \left(\frac{c^B}{c_f^B} - \frac{c_s^B}{c_f^B}\right)\mathbf{J}_s^{\Omega} - \frac{c_s^B}{c_f^B}\mathbf{J}_f^{\Omega} \tag{3.40}$$

$$= \frac{c^B}{c_f^B}\mathbf{J}_s^{\Omega} - \frac{c_s^B}{c_f^B}c^{\Omega}\mathbf{Q}^{\Omega} \tag{3.41}$$

$$= \frac{c^B}{c_f^B}\left(\mathbf{J}_s^{\Omega} - \phi_s^B\, c^{\Omega}\mathbf{Q}^{\Omega}\right) \tag{3.42}$$

$$= \frac{N^B}{N^B-N_s^B}\left(\mathbf{J}_s^{\Omega} - c_s^*\,\mathbf{Q}^{\Omega}\right) . \tag{3.43}$$

Where $\phi_s^B = N_s^B/N^B$ is the molar fraction of solutes in the bulk and $c_s^* = \phi_s^B c$. Replacing the excess flux from Eq. (3.43) in the entropy production from Eq. (3.11) we obtain the following transport matrix

$$\begin{bmatrix} \mathbf{Q} \\ \mathbf{J}_s - c_s^* \mathbf{Q} \end{bmatrix} = \begin{bmatrix} M'_{QQ} & M'_{QJ} \\ M'_{JQ} & M'_{JJ} \end{bmatrix} \begin{bmatrix} -\nabla P/T \\ -\nabla \mu'_s/T \end{bmatrix} \tag{3.44}$$

with

$$\nabla \mu'_s = \frac{N^B}{N^B - N_s^B} \nabla \mu_s \, . \tag{3.45}$$

If we replace the transformed flux in Eq. (3.43) back into Eq. (3.38) we get the new connection between the microscopic forces and their thermodynamic counterpart;

$$\mathbf{Q}^{\Omega} = M'_{QJ} \frac{N^B}{N^B - N_s^B} \mathbf{F}_s^{\mu} = M'_{QJ}(-\nabla \mu'_s) \, , \tag{3.46}$$

recovering the result in Eq. (3.39). This expression differs from the result reported by Yoshida *et al.* [27]:

$$\nabla \mu_s \equiv -\frac{N^B}{N^B - N_s^B} \mathbf{F}_s^{\mu,\mathrm{Y}} \tag{3.47}$$

where $\mathbf{F}_s^{\mu,\mathrm{Y}}$ is the microscopic force applied in their simulations. However, the difference is due to a somewhat unfortunate definition of the chemical potential gradient of the solutes. The expression used in ref [27] underestimates the effect of the thermodynamic force $\nabla \mu_s$ by a factor equal to the molar fraction of solvents in the bulk $\phi_f^B = N_f^B/N^B$. Therefore, this approximation is only valid in the limit of infinite dilution.

We can show using Eq. (2.15) the relations between the transport coefficients in Eq. (3.13) and Eq. (3.44):

$$M_{QQ} = M'_{QQ} \tag{3.48}$$

$$M_{QJ} = \frac{N^B}{N^B - N_s^B} M'_{QJ} \tag{3.49}$$

$$M_{JQ} = \frac{N^B}{N^B - N_s^B} M'_{JQ} \tag{3.50}$$

$$M_{JJ} = \left(\frac{N^B}{N^B - N_s^B} \right)^2 M'_{JJ} \, . \tag{3.51}$$

We focus now on the additional off-diagonal term M_{JQ} of the transport matrix. It connects the excess solute flux with a pressure gradient. A pressure gradient exerts a force on a volume

of fluid rather than on individual particles. As a first approximation, one might tend to connect the thermodynamic force acting on the system to the microscopic force as

$$\mathbf{F}^P = -\boldsymbol{\nabla} P / c^\Omega \,. \tag{3.52}$$

This is a common choice (see e.g [94, 95, 27, 44, 73]) which applies a constant force to all the particles in the system. Therefore, rather than describing a pressure gradient yields a gravitational-like field. If the fluid density is heterogeneous, as is the case for a slit, the constant force creates a pressure gradient dependent on the position from the walls.

In what follows, we consider a small volume ω at a distance z_ω from the wall. We obtain that the Hamiltonian coupling to the external force is

$$\mathscr{H}_{ext}(\omega) = \sum_{i\in \text{all}}^{\omega} \mathbf{x}_i \cdot \mathbf{F}^P(\omega) \,, \tag{3.53}$$

therefore $A(\omega) = \sum^{\omega}_{i\in \text{s}} \mathbf{x}_i$.

The variable that couples to the external field $\mathbf{F}^P(\omega)$ is given by

$$\begin{aligned} \dot{A}(\omega) &= \sum_{i\in \text{s}}^{\omega} \dot{\mathbf{x}}_i \\ &= V^\omega \left(\frac{1}{N^\omega} \sum_{i\in \text{s}}^{\omega} \dot{\mathbf{x}}_i \right) \frac{N^\omega}{V^\omega} \\ &= V^\omega \mathbf{Q}^\omega c(\omega) \,. \end{aligned}$$

Finally, using Eq. (3.36) we can express the excess solute flux as:

$$\begin{aligned} \mathbf{J}_s^\Omega - \frac{c_s^B}{c_f^B}\mathbf{J}_f^\Omega =< \mathbf{J}_s^\Omega - \frac{c_s^B}{c_f^B}\mathbf{J}_f^\Omega > &= \left[\frac{V^\omega}{k_B T} \int_0^\infty < (\mathbf{J}_s^\Omega - \frac{c_s^B}{c_f^B}\mathbf{J}_f^\Omega)(t)(Q^\Omega)(0) > dt \right] c\,\mathbf{F}^P \\ &= \frac{M_{JQ}}{T}\, c\,\mathbf{F}^P \,. \end{aligned} \tag{3.54}$$

By comparing Eq. (3.54) with Eq. (3.13) the microscopic force representing the pressure gradient is given by,

$$\mathbf{F}^P(z) = -\frac{\boldsymbol{\nabla} P}{c(z)} \,. \tag{3.55}$$

Finally, the expressions for the transport coefficients in Eq. (3.38) and Eq. (3.54) are equivalent, as the correlation functions are symmetric in time. Thus, $M_{JQ} = M_{QJ}$, fulfilling Onsager's reciprocal relations.

3.3 Simulations

3.3.1 Benchmark

We use the system described by Yoshida *et al.* [27] as a benchmark to study the basic concepts on diffusio-osmosis. We performed the simulations using LAMMPS [96]. Particles interact via a 12-6 Lennard-Jones potential (LJ) $V_{LJ}(r) = 4\varepsilon_{ij}^{LJ}[(\sigma_{ij}^{LJ}/r)^{12} - (\sigma_{ij}^{LJ}/r)^{6}]$ shifted and truncated at $r = r_{\text{cut}}$, such that

$$V_{TS}(r) = \begin{cases} V_{LJ}(r) - V_{LJ}(r_{\text{cut}}), & \text{if } r \leq r_{\text{cut}} \\ 0, & \text{otherwise.} \end{cases} \tag{3.56}$$

The indices i and j denote the particle types in our simulations: solutes (s), solvents (f) and wall (w). We assume that in the bulk the solute and solvent behave as an ideal mixture. Therefore, we choose the same Lennard-Jones interaction for the particle pairs ss, sf, ff with $\varepsilon_{ij}^{LJ} = \varepsilon_0$ and $\sigma_{ij}^{LJ} = \sigma_0$. We also use these same parameters for the wall-solvent interaction wf. The wall-solute interaction strength ε_{ws}^{LJ} and σ_{ws}^{LJ} were varied to control the degree of solute adsorption or depletion around the colloidal particle. For all interactions, $r_c = 2.5\sigma_0$. In what follows, we use the mass m_0 of all the particles (s,f and w) as our unit of mass and we set our unit of energy equal to ε_0, whilst our unit of length is equal to σ_0, all other units are subsequently expressed in term of these basic units. As a result, forces are expressed in units ε_0/σ_0, and our unit of time is $\tau \equiv \sigma_0\sqrt{m_0/\varepsilon_0}$.

The system is as shown in Fig. 3.2. The initial dimensions of the simulation box are $(17\sigma_0, 17\sigma_0, 35\sigma_0)$ with 7424 solution particles. The average concentration of solutes in the whole volume of $\bar{c}_s = 0.15$. The box is periodic in the x and y directions. In the z direction, there is a solid wall at the bottom and a reflective surface at the top. The reflective boundary inverts the momentum in the direction perpendicular to the surface and places back the atoms with mirrored positions when they go outside the boundary during the position update. Meanwhile, the lower wall is made of one layer of immobile solid atoms arranged in a face-centred cubic (FCC) (100) lattice with a constant $\sqrt{2}\sigma_0$. The interaction of the solutes with the wall is $(\varepsilon_{sw}, \sigma_{sw}^{LJ}) = (1.5, 1.5)$. We used a Nosé-Hoover thermostat [87] to fix $k_BT/\varepsilon_0 = 1.0$ for all the simulations.

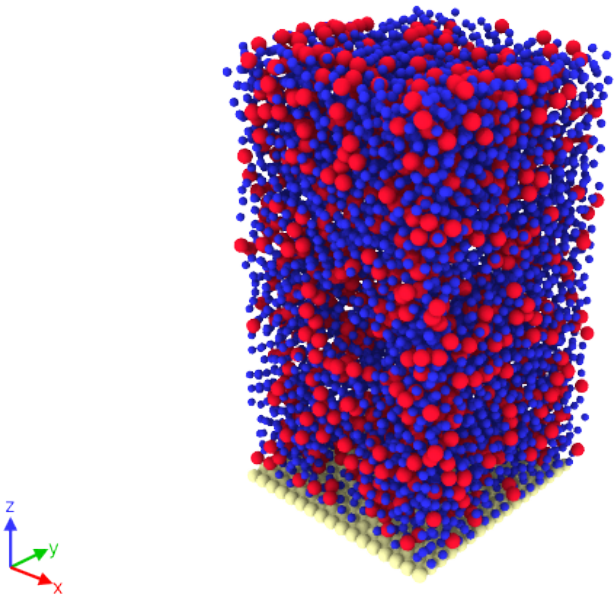

Fig. 3.2 Simulation box used for NEMD simulations. There are periodic boundary conditions in x and y. In the z direction, there is solid wall at the bottom and a reflective surface at the top.

To initialise the system, we performed 10^5 NVT MD steps, using a time step $\Delta t = 0.002\tau$. Additionally, 5×10^5 steps were required to impose $P\sigma_0^3/\varepsilon_0 = 1.0$ as described in [97, 98]; this was achieved by applying an external force on the lower wall atoms. During this process, we sampled the height in the z-direction. For all the subsequent simulations, the height was fixed at the average value.

After equilibrating and barostating, we sampled the density distribution for all the species during 3×10^6 steps (see Fig. 3.3). The initial peak of the solvents near the wall is due to the higher excluded volume by the solutes which leave space for the smaller solvent particles to come closer to the wall. The migration of solutes towards the interface during the equilibration decreases their concentration in the bulk, therefore it is expected that $c_s^B < \bar{c}$. This effect is negligible for the system size and the relatively weak ε_{ws}. Fig. 3.3 also shows some density oscillations due to the reflecting boundary. These oscillations pose no problem, as this region is excluded from all the following measurements.

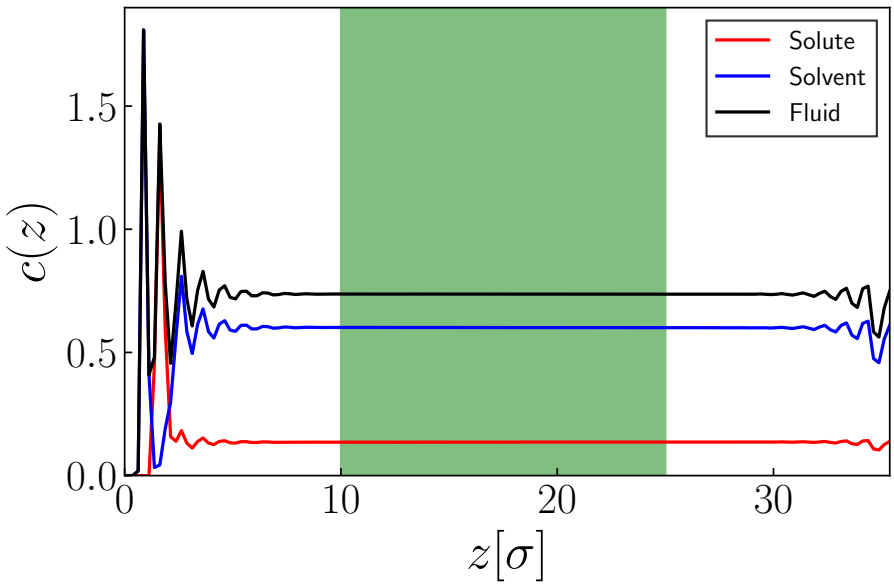

Fig. 3.3 Density distribution per species sampled every $\Delta_z = 0.25\sigma_0$. The first peak in the solvents appears before the solutes as $\sigma_{wf} < \sigma_{ws}$.

Field-Driven Non-Equilibrium Molecular Dynamics

There are two ways of imposing microscopic forces for diffusio-osmosis using FD-NEMD. On the one hand, we can apply a force on each particle depending on their species [27]. On the other hand, using the equilibrium density distribution for each species, we can compute the average force applied at a given distance z from the wall as [48],

$$\mathbf{F}^{\mu}_{\text{ave}}(z) = \frac{[c_s(z)\mathbf{F}^{\mu}_{s} + c_f(z)\mathbf{F}^{\mu}_{f}]}{c(z)} \tag{3.57}$$

where the force on the solutes $\mathbf{F}^{\mu}_{s}$ is given by Eq. (3.39) and the force on the solvents $\mathbf{F}^{\mu}_{f}$ is determined by imposing mechanical equilibrium in the bulk Eq. (3.32). Both approaches should give the same flow profiles if the spatial binning used to measure the concentration distributions in Eq. (3.57) is the same as the one used to sample the velocity profiles. Furthermore, Liu *et al.* [48] showed that the flow profile using Eq. (3.57) are in good agreement with results obtained applying an explicit chemical potential gradient. It worth noticing that the application of $\mathbf{F}^{\mu}_{\text{ave}}(z)$ will not reproduce the correct diffusive fluxes. It gives the right force per unite volume but not per species.

In this chapter, we will use Eq. (3.57) to apply the microscopic forces. The force distribution on the solution is shown in Fig. 3.4.

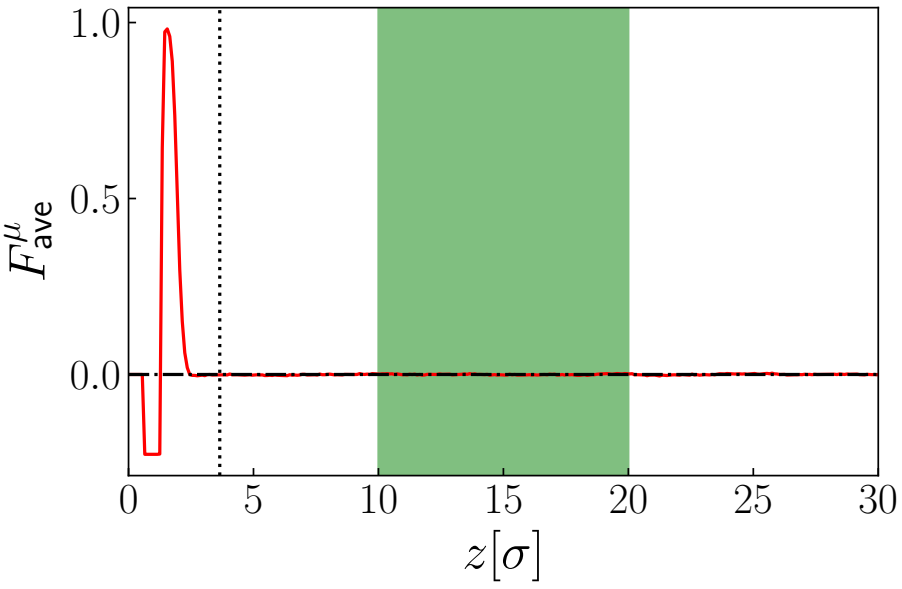

Fig. 3.4 Force applied as a function of the distance from the wall for diffusio-osmotic simulations with $\boldsymbol{\nabla}\mu_s = 1$. Notice that the magnitude of the gradient is for plotting purposes only.

Similarly, for pressure-driven simulations, we can apply a force distribution given by Eq. (3.55) and shown in Fig. 3.5.

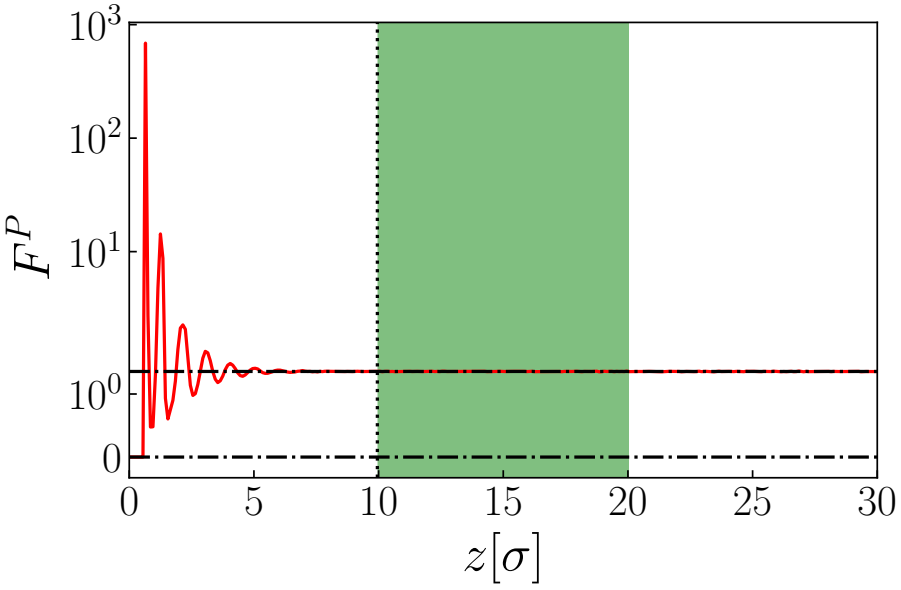

Fig. 3.5 Force applied as a function of the distance from the wall for pressure-driven simulations with $\nabla P = 1$.Notice that the magnitude of the gradient is for plotting purposes only.

We performed 10^8 steps of FD-NEMD. We applied the computed force distributions and measured the velocity profiles in the fluid. Results in Fig. 3.6 show the diffusio-osmotic velocity profile for $\nabla\mu_s = -0.125$. We observe the plug-flow profile characteristic of diffusio-osmosis. At the interface, there is a steep increase in velocity due to the excess of solutes. Notice that all the flow profiles are non-monotonic in z and exhibit a peak before settling down to the bulk velocity. This peak has also been observed in previous studies [27, 48]. This overshoot can be (partially) described using Eq. (3.19) (see also Fig. 3.12). Nevertheless, note that a constant viscosity was assumed. A possible explanation for this non-monotonic behaviour is that the effect of the excess of concentration at the interface is not balanced locally, but globally, as discussed by Marbach *et al.* [63]. Therefore, the overshoot takes place before the effect of the non-constant (non-local) viscosity compensates the effect.

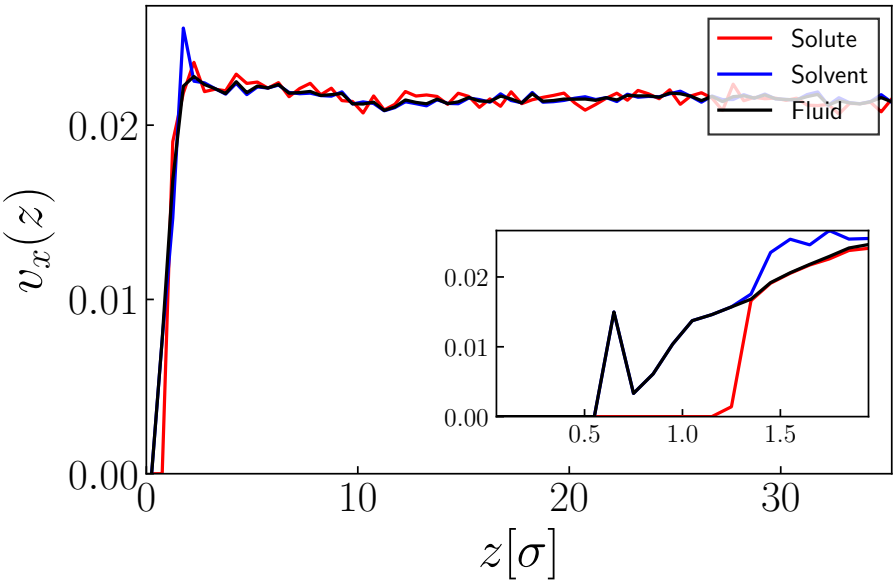

Fig. 3.6 Velocity profiles per species for diffusio-osmotic flow for $\nabla\mu_s = -0.125$. The sampling bin sizes are $\Delta_z = 0.25\sigma_0$ and $\Delta_z = 0.10\sigma_0$ for the insert.

Finally, in Fig. 3.7 we show the concentration distribution for equilibrium simulations and the largest chemical potential gradient applied in our FD-NEMD simulations. It shows that the density distribution remains unperturbed in the direction perpendicular to the wall.

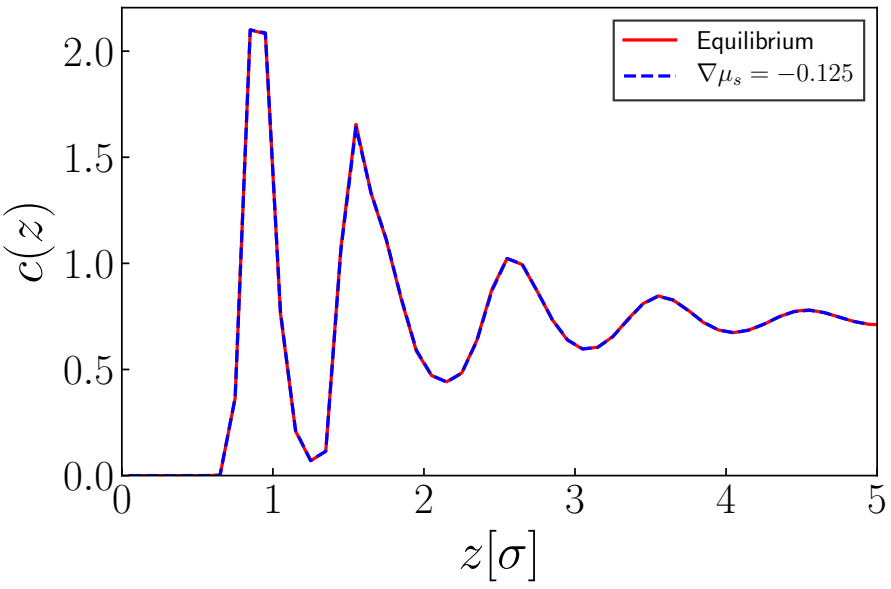

Fig. 3.7 Density profiles from EMD and FD-NEMD using a gradient of chemical potentials in the solutes of $\nabla\mu_s = -0.125$. The binning spacing for the density sampling is $\Delta_z = 0.1\sigma_0$.

Theoretical predictions

In order to use the theoretical expressions (Eq. (3.19) or Eq. (3.23)) for the slip velocity, we need to compute the concentration distribution $c_i(z)$ of all species i as a function of the distance z from the wall, and the viscosity η of the solution. The former is obtained from EMD simulations, and relatively short runs are required as the equilibration in the z-direction is fast. In the simplest theoretical description, the viscosity is assumed to be independent of z, and equal to its bulk value: $\eta(z) = \eta^B$. Assuming that η is independent of z is a strong assumption, as we know that the concentration changes and the fluid shows layering near the wall, which affects the local viscosity. η^B can be obtained by several methods as described in Appendix C.

One particularity of our benchmark system is that solvents and solutes have different σ^{LJ}. This fact is important as both species have different accessible volumes in the system, in particular close to the wall. Todd *et al.* [94] identified the problem of defining the average particle density in a WCA-fluid [99] confined between two solid walls and concluded that the definition of the available width to the fluid atoms will always have some degree of arbitrariness. Let us try to define the minimum approach distance $d_i^{\min}$ for particles of species i to the wall. $d_i^{\min}$ is system-specific and depends not only on the interaction between the particles but also in the lattice, orientation and, in general, the structure of the wall.

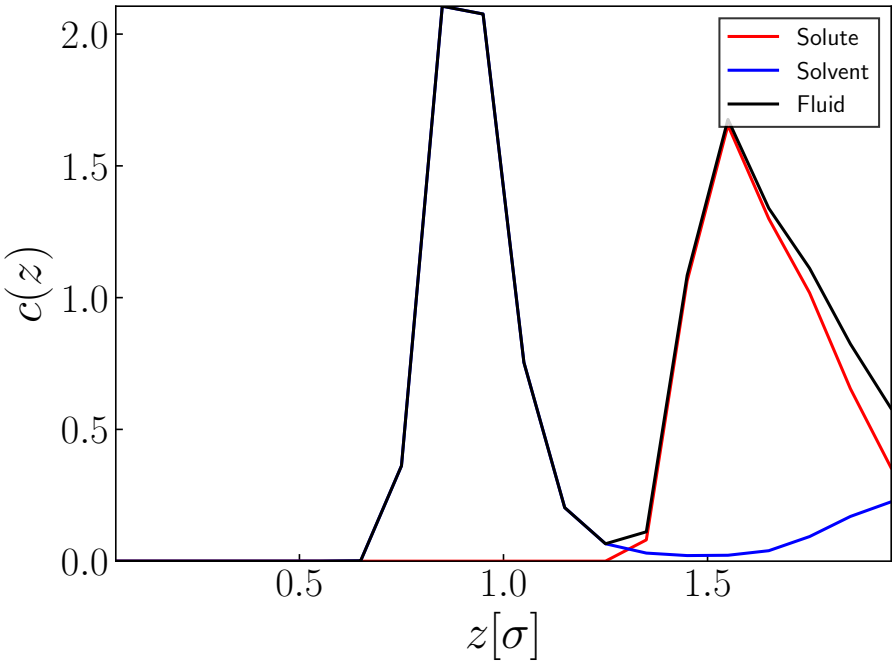

Fig. 3.8 Detail of the density profiles close to the solid wall. The density sampling bin size is $\Delta_z = 0.1\sigma_0^{LJ}$.

In Fig. 3.8 we show the density distribution for each species close to the wall. As a first approximation, we can define $d_i^{\min}$ as the distance from the wall below which no particles of species i are found. We obtain $d_f^{\min} = 0.55$ and $d_s^{\min} = 1.15$ for the solvents and solutes respectively. A second choice would be to perform NEMD simulations and measure the flow profile for a Poiseuille flow (see Fig. 3.9) or a diffusio-osmotic flow (see Fig. 3.6). In the NEMD cases, we can compute the position of the maximum distance from the wall, below which the velocity of the fluid is zero. For the present system, the two approaches produce the same results. However, the two approaches are not equivalent. In the case of diffusio-osmosis, what drives the flow is the movement of the excess species within the interface. Therefore, if there is extremely strong adsorption of such species at the wall, they could have negligible mobility and do not contribute to diffusio-osmosis. In such a case, the first approximation based solely on the density distributions does not agree with a mobility-based estimate.

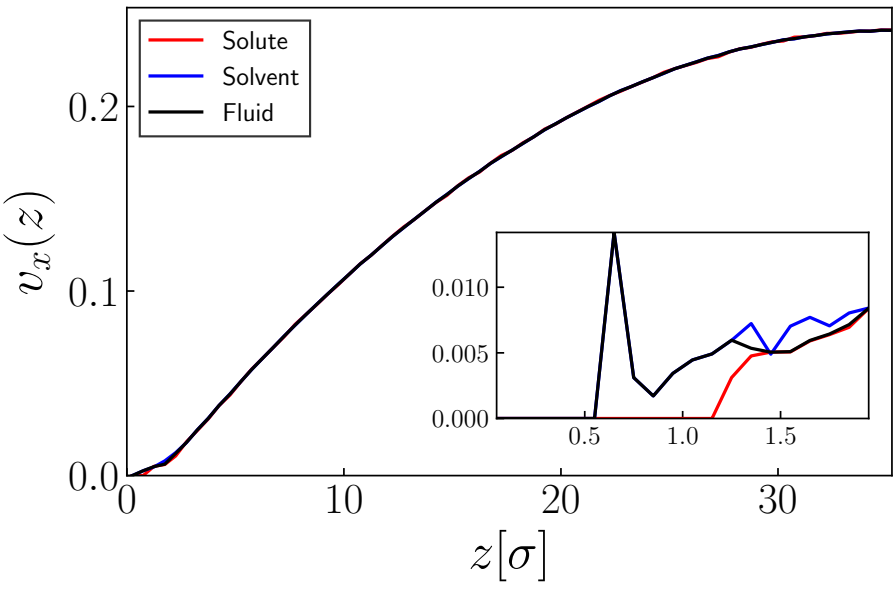

Fig. 3.9 Velocity profiles per species for pressure-driven flow for $\nabla P = -0.00063$. The sampling bin sizes are $0.25\Delta_z = \sigma_0$ and $0.1\Delta_z = \sigma_0$ for the insert.

All relevant parameters in the theory of diffusio-osmosis, such as Γ, K, L^*, depend on moments of the concentration distributions (see Sec. 3.2.2). The integrals in the definition of these parameters are evaluated from the surface ($z_0 = 0$) to the bulk ($z \to \infty$). Nevertheless, in practice, due to the volume exclusion, z_0 is not easily defined. To elaborate on the importance of the definition of z_0, let us focus on the most critical parameter, L^*, which depends on the first moment of the concentration distribution. In Fig. 3.10, we show the different values for the integrand I_ξ in Eq. (3.26) as the lower limit for the integration z_0 is varied. The results show that it is crucial to define z_0 properly, as theoretical estimates of the velocity vary significantly with the choice of this parameter. The different estimates for the velocity using different z_0 are shown in Fig. 3.11.

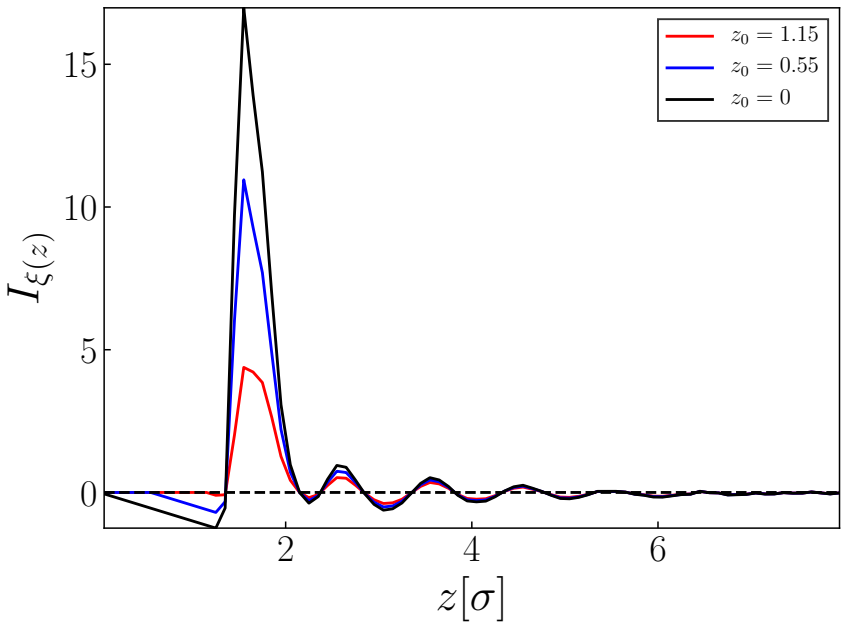

Fig. 3.10 Integrand in Eq. (3.26) for the solutes with a concentration distribution sampled every $\Delta_z = 0.25\sigma_0$. z_0 takes 3 different values: the position of the wall $z_0 = 0$, $z_0 = d_f^{\min} = 0.55$ and $z_0 = d_s^{\min} = 1.15$. Notice that the integrands were translated accordingly such that their maximum values coincide.

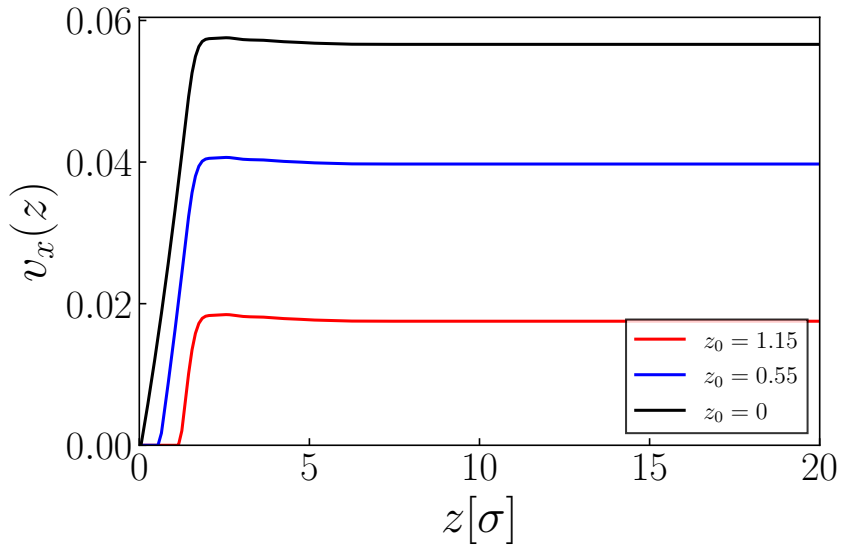

Fig. 3.11 Theoretical prediction of the velocity contribution from the solutes in Eq. (3.19) for different low integration limits z_0. The solute density distribution was sampled every $\Delta_z = 0.25\sigma_0^{LJ}$.

Using our LTE approach, we extended the Derjaguin-Anderson theory of diffusio-osmosis taking into account all species in the solution. Therefore, we can determine the contribution from the different species to the velocity in Eq. (3.19). In Fig. 3.12, both solvents and solutes contributions have the same sign. The reason is that, although their gradients have opposite gradients, the additional term in Eq. (3.19) compensates, so the net contribution is positive. In this case, it is straightforward to estimate the sign of the diffusio-osmotic velocity *a priori*, using our thermodynamic picture (see Sec. 2.1.1). However, Eq. (3.19) can also deal with situations where there is a multi-component solution with competing interactions between the species and the surface.

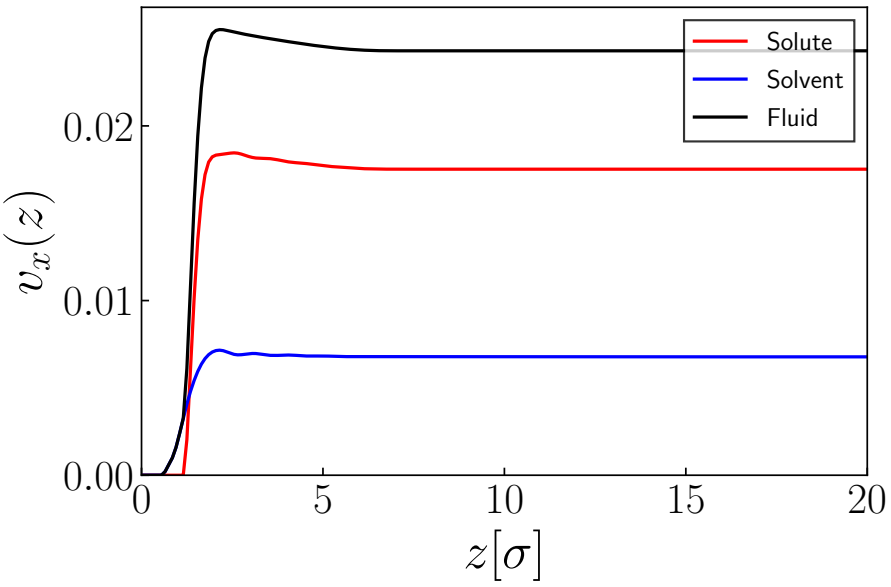

Fig. 3.12 Theoretical predictions of the Individual and total contributions to diffusio-osmotic velocity in Eq. (3.19), with $z_0 = d_i^{\min}$.

In Fig. 3.13 we compare the results of our FD-NEMD simulations applying two different magnitudes of the microscopic forces on the solutes. One, given by Eq. (3.39). The other is the force used by Yoshida *et al.* [27]. Despite having applied the same $\nabla\mu_s$, in the latter, the connection between the microscopic force and the chemical potential has a pre-factor, as shown in Eq. (3.47). This pre-factor reduces the contribution from the thermodynamic force, resulting in a smaller diffusio-osmotic velocity.

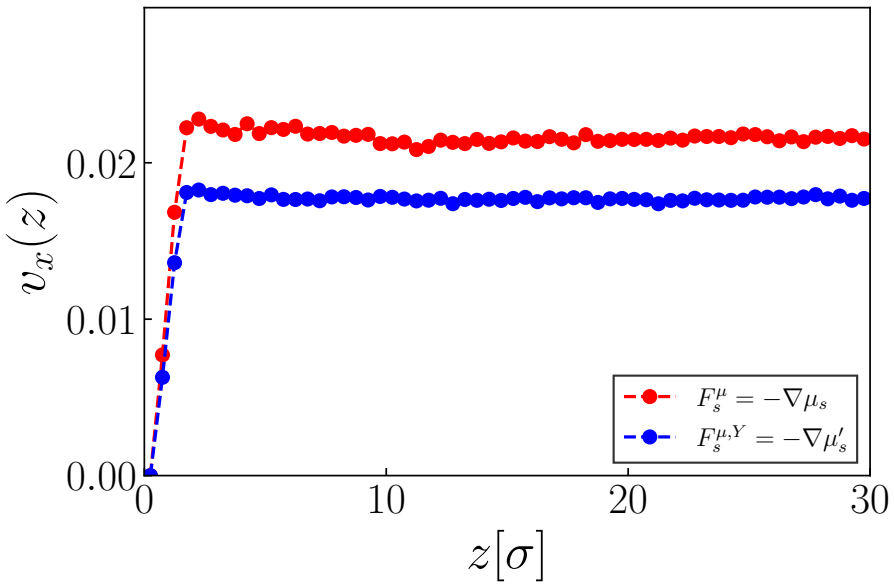

Fig. 3.13 Diffusio-osmotic flow profile for $\nabla\mu_s = -0.125$. The NEMD results applying the force reported by Yoshida *et al.* (see Eq. (3.47)) are shown in blue dots and the results using Eq. (3.39) are shown in red dots .

Fig. 3.14 shows the velocity profiles for different values of the gradient of the chemical potential $\nabla\mu_s$. The characteristic plug flow profile is present, and the bulk velocity scales linearly with the thermodynamic force. We also show the theoretical predictions from our generalisation of the Derjaguin-Anderson theory (see Eq. (3.19)). It is worth pointing out that the theoretical results were derived using Stokes equations, assuming a constant viscosity. However, neither Stokes predictions nor a constant viscosity should be assumed at the typical scales of the diffuse layer [43, 100]. Bitsatis *et al.* [101] proposed a simple way to obtain a position-dependent viscosity using a local average density model (LADM). In their model, the strongly inhomogeneous density close to a solid wall is replaced by averages over a typical molecular diameter. The local viscosity would penalise the contributions from the excess close to the wall, reducing the theoretical estimate of the velocity. The idea of a local viscosity seems promising at first sight, but for fluids at small scales, the reality is that the transport coefficients become non-local [102]. We did not compute the local approximations to the viscosity to try to improve the theoretical predictions, as our main focus was to explore the NEMD simulations.

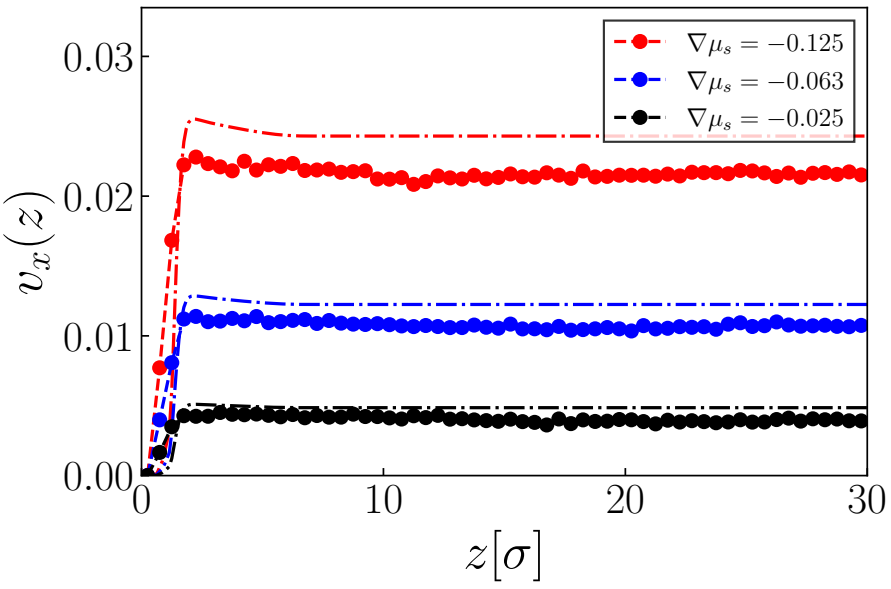

Fig. 3.14 Diffusio-osmotic velocity profile for different chemical potential gradients. The simulation results are shown in circles. The theoretical results using Eq. (3.19) are in dot-lines. The velocity sampling bin size is $0.25\sigma_0^{LJ}$.

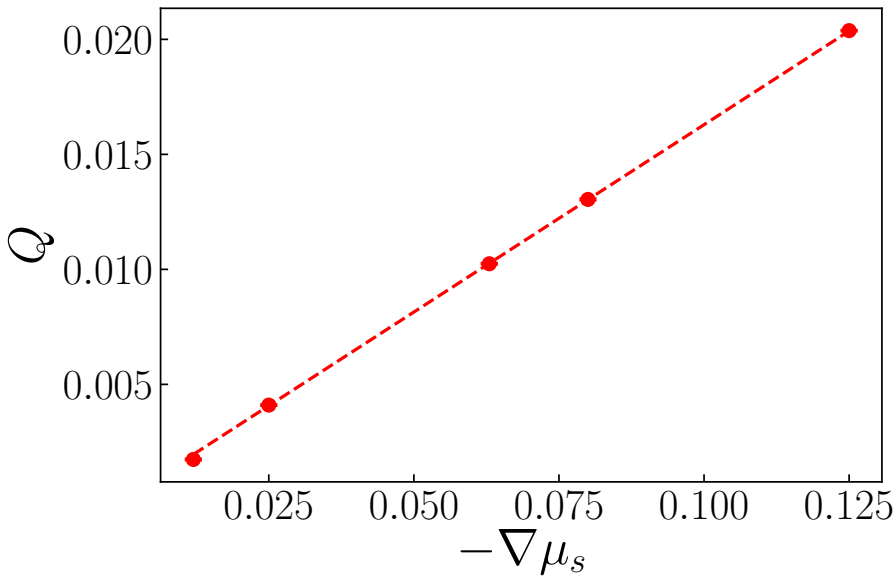

Fig. 3.15 Total volume flux Q vs the chemical potential gradient $\boldsymbol{\nabla}\mu_s$. The slope of the linear fit gives the transport coefficient M_{QS}.

Having computed the velocities for all the species we can estimate the total volume flow $\mathbf{Q}$ defined by Eq. (3.37). In Fig. 3.15 we plot the results for different $\nabla\mu_s$. We obtain that the transport coefficient from $M_{QS} = 0.159 \pm 0.004$ (see Eq. (3.13)), which could be transformed into the coefficient $M'_{QS} = 0.126 \pm 0.003$ by using Eq.(3.48). Our estimate agrees with the results reported by Yoshida *et al.* [27] $M'_{QS} = 0.120 \pm 0.005$. It is important to highlight here that the prefactor in the microscopic force used by Yoshida *et al.* does not influence their results for the transport coefficients, as in their simulations they employ the correct thermodynamic force $\nabla\mu'_s$ for the representation of the transport matrix in Eq. (3.44).

3.3.2 Moving along a concentration gradient

In Sec. 2.4.2, we described two non-equilibrium methods to simulate diffusio-osmosis, namely FD-NEMD and BD-NEMD. In experimental situations [103, 36, 25, 104], diffusio-osmosis(phoresis) is generated by imposing a concentration gradient along a channel, slit or microfluidic device. Therefore, it would be reasonable to consider BD-NEMD to simulate more realistic systems. Unfortunately, in addition to the drawbacks mentioned in Sec. 2.4.2, imposing an explicit gradient makes it challenging to study diffusio-osmosis, as convective effects influence the system as will be described in Chapter 4. In this section, we study how the properties of the system and the flow change along a concentration gradient using FD-NEMD instead. For the simulations, we used the same system as described for the benchmark. The only difference being that we set $\sigma_{sw}^{LJ} = 1.0$.

We performed EMD simulations and measured the concentration distribution for each species. In Fig. 3.16, the Gibbs surface excess Γ (see Eq. (3.24)) is plotted for both species. The results show that Γ is not a constant quantity along the gradient; in fact, it is non-monotonic. On the one hand, for low concentrations, the excess of particles of species i at the interface should go to zero when there are no particles in the system. On the other hand, for high concentrations, the interface saturates, causing a reduction in Γ that should reach a limiting value depending on the structure of the solid wall, interaction, etc.

Next, we performed FD-NEMD imposing a solute concentration gradient $\nabla c_s^b = 0.017$ which was included in the microscopic force by using Eq.(3.21). Fig. 3.17 shows the diffusio-osmotic velocities compared with the theoretical predictions for different solute/solvent ratios. The diffusio-osmotic velocity decays as the concentration of solutes increases in the bulk. The reason for this behaviour is that the driving force is the chemical potential gradient and not the concentration gradient.

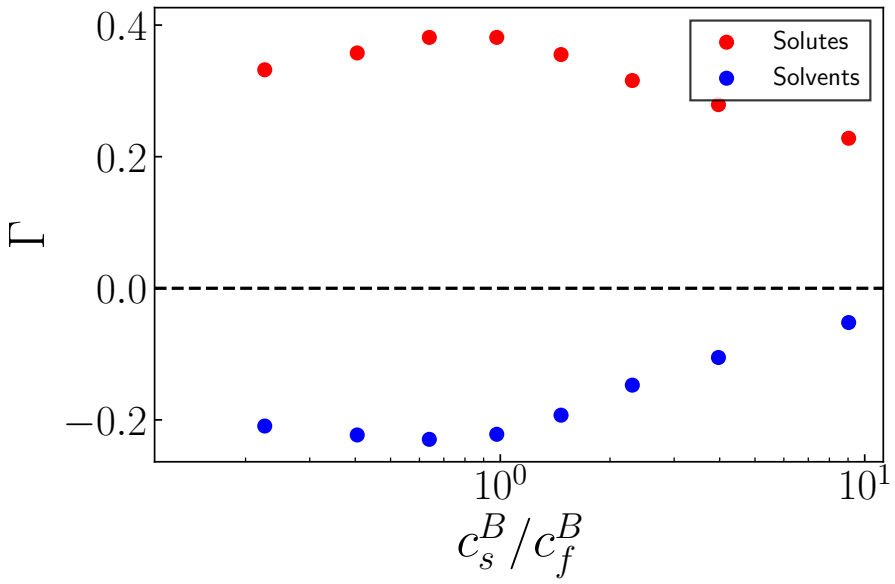

Fig. 3.16 Gibbs surface excess Γ for solutes and solvents at different bulk concentration ratios c_s^B/c_f^B.

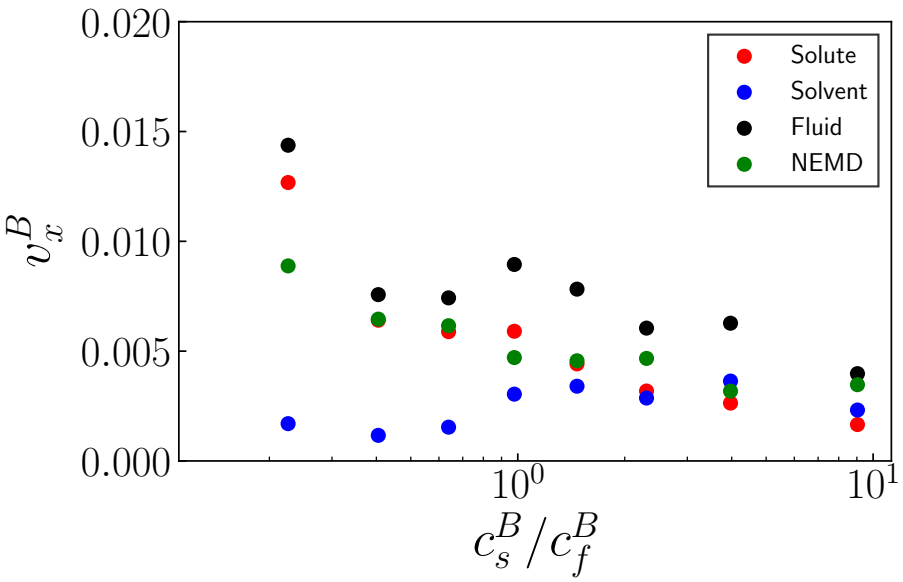

Fig. 3.17 Diffusio-osmotic velocity for different bulk concentration ratios, c_s^B/c_f^B with $\nabla c_s^b = 0.017$. Results from FD-NEMD are shown in green; theoretical predictions for the solutes contribution are in red, solvents in blue and the total contribution in black.

3.4 Conclusions

We have assumed local thermodynamic equilibrium to derive a theoretical expression for the diffusio-osmotic velocity of a multi-component system. In our general approach, we take into account all the species in the solution, including the solvent. In our formalism, the chemical potential gradient, and not the concentration gradient, appears as the thermodynamic force driving the process. We show that the Derjaguin-Anderson expression for the diffusio-osmotic velocity follows as a special case from our results when considering an ideal-dilute solution.

We used non-equilibrium thermodynamics to find the entropy production associated with diffusiophoresis. This procedure allowed us to further connect the thermodynamic and microscopic forces for a representation involving pressure and chemical potential gradients. The derivation allowed us to identify subtleties which are not pointed out or discussed elsewhere and are crucial for the understanding of phoretic motion. Furthermore, our simulations on a benchmark system allowed us to investigate additional details related to the microscopic forces applied in the FD-NEMD scheme and the estimates using the theoretical expressions. Finally, we performed a set of simulations of the diffusio-osmotic flow along a constant concentration gradient. The results show a clear difference in the flow velocity between the high and low concentration regions, which is expected from the logarithmic sensing of the concentration distributions in diffusio-osmosis.

Chapter 4

Colloidal diffusiophoresis

"If I could remember the names of these particles, I would have been a botanist. I will therefore restrict myself to a small fraction of the particles in order to keep the discussion simple. Probably the proton, the neutron, and the electron are familiar to all of you — you may even own some."

Enrico Fermi

4.1 Introduction

The same mechanism that causes diffusio-osmosis drives the motion of a colloid, polymer, or other mesoscopic moieties. Derjaguin, for instance, did not analyse the explicit-movement of particles. Instead, considering the radius of curvature sufficiently large, he focused on the fluid flow along a flat surface and obtained the particle velocity from the slip velocity. It is reasonable to use Derjaguin's approximation [14, 93] if the mesoscopic particle (say a colloid) is very large compared to the characteristic length scale on which adsorption or depletion occurs. However, Derjaguin's approach is likely to fail if the particles that are subject to phoresis are no longer large compared to the range of adsorption/depletion. Anderson *et al.* [15] obtained a more general estimate of the diffusiophoretic velocity by including the effect of the particle radius a. The results express the velocity in a series in expansion in L/a. The leading is identical to the boundary layer approximation, with L being the diffuse layer thickness.

In this chapter, we study the phoretic motion of a colloidal particle. In Sec. 4.2, we present Anderson's extension to the theory of diffusiophoresis. We describe the main assumptions and emphasise on the physical parameters that can be obtained from simulations. Later, in Sec. 4.3, we use the methods described in Sec. 2.4.2 to simulate a single colloidal particle.

4.2 Theory

When a colloidal particle is placed in a solution with a concentration gradient, for instance in solutes, the concentration field is disturbed. The reason is that the solution rearranges by the sole presence of the colloid (volume exclusion) and by any additional interaction. The colloid will move either, following the gradient in solutes or the opposite direction. The direction will depend on the interaction between the colloid and the species in the solution. Anderson *et al.* [15] developed a quantitative theory to describe the diffusiophoretic mobility of the colloid. They solved the conservation equations for the solution both at the vicinity and far away from the particle. In this section, we illustrate the key arguments in their theory.

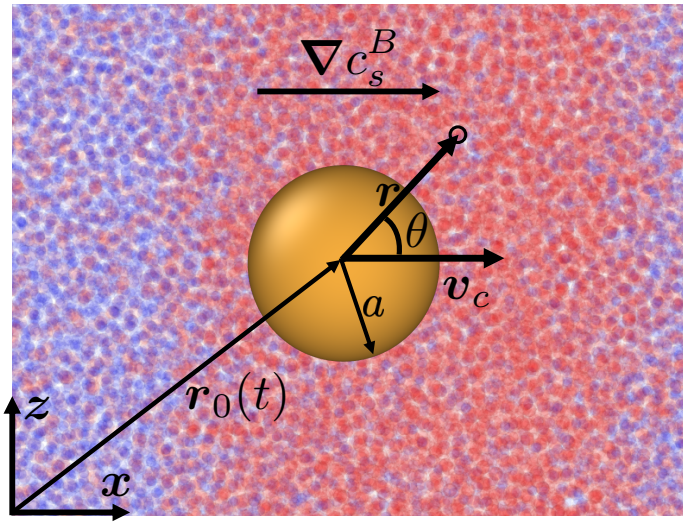

Fig. 4.1 Colloidal particle with radius a moving along a concentration gradient ∇c_s^B with velocity $\boldsymbol{v}_c$. The position of the colloidal centre with respect to a laboratory frame is given by $\mathbf{r}_0$ and the position of a solute measure from the colloid centre is given by $\mathbf{r}$. θ is the angle between $\boldsymbol{v}_c$ and $\mathbf{r}_0$.

We consider a colloid in a solution with uncharged solute molecules dissolved in it. The solutes interact with the colloid through steric repulsion as well as dipole and van der walls forces. The solute concentration far from the colloid is $c_s^B(r)$, i.e the unperturbed concentration field that would exist in the absence of the colloid. There is a solute concentration

gradient across the system with magnitude $\alpha = \left|\nabla c_s^B(r_0)\right|$, at the position of the centre of the colloid r_0. For low Reynolds numbers, the fluid motion is described by Stoke's equations

$$\nabla \cdot \boldsymbol{v} = 0, \tag{4.1}$$

$$\eta \nabla^2 \boldsymbol{v} - \nabla P - c_s \nabla \phi = 0, \tag{4.2}$$

Where ϕ is the mean-field felt by the solutes due to interaction with the colloid and the surrounding solvent, as described in Sec. 3.2.2. $\boldsymbol{v}$ is the velocity of the fluid relative to the colloid and fulfils the no-slip boundary condition at the surface of the colloid;

$$\boldsymbol{v} = 0 \quad \text{for} \quad \boldsymbol{r} = a\,. \tag{4.3}$$

The additional condition is that the velocity at infinity is given by;

$$\boldsymbol{v} = -\boldsymbol{v}_c \quad \text{for} \quad \boldsymbol{r} \to \infty\,. \tag{4.4}$$

The mass conservation equations for the solutes expressed in a reference frame centred and moving with the colloid are given by:

$$\frac{\partial c_s}{\partial t} + \nabla \cdot \boldsymbol{J}_s = 0, \tag{4.5}$$

$$\boldsymbol{J}_s = -D_s \nabla c_s - \frac{D_s}{k_B T} c_s \nabla \phi + \boldsymbol{v} c_s, \tag{4.6}$$

where c_s is the solute concentration, $\boldsymbol{J}_s$ is the solute flux and D_s is the diffusion coefficient of the solute particles *in the bulk*.

As the colloid migrates, its environment changes. Thus, the local concentration and velocity change, as discussed in Sec. 3.3.2. In this analysis, we assume that the migration speed is slow. This assumption has two implications: the first one that the Peclet number is very small

$$Pe^{FD} = \frac{a v_c}{D_s} \ll 1\,, \tag{4.7}$$

here FD is used as this Peclet number also applies to our FD-NEMD simulations (see Sec. 4.3.2).

Also, a quasi-steady state is achieved. The reason is that the relaxation time for a change in concentration $c_s^B/(v_c\alpha)$ is longer than the time it takes to the solutes to relax around the colloid a^2/D_s, thus

$$\frac{a\alpha}{c_s^B(r_0)} \lesssim 1;. \tag{4.8}$$

Therefore, Eq. (4.5) becomes time independent and the convective term in Eq. (4.6) can be neglected, leading to:

$$\boldsymbol{\nabla}^2 c_s + \frac{\boldsymbol{\nabla}\cdot(c_s\boldsymbol{\nabla}\phi)}{k_B T} = 0\,. \tag{4.9}$$

The boundary conditions are such that there is no solute flux through the colloid surface and that the unperturbed concentration field far from the colloid is given by:

$$c_s^B \backsim c_s^B(r_0) + \boldsymbol{r}\cdot\boldsymbol{\nabla}c_s \quad \text{for} \quad \boldsymbol{r}\to\infty\,. \tag{4.10}$$

After neglecting convection, Eq. (4.9) can be decoupled from the equations describing the solution flow Eqs. (4.1) and (4.2). The axisymmetric solution $c_s(r,\theta)$ is obtained by using a matching asymptomatic expansion in $\lambda \equiv L/a$, considering two different regions of the problem. An inner region close to the colloid, with thickness L, where all interactions (direct and indirect[1]) between solute molecules and the colloid happen. The outer region is where $\phi(r)$ and its derivatives are zero. Once the concentration field is known, the equations for the solution are solved. The body force depending on θ is included via the concentration field in the term $c_s\boldsymbol{\nabla}\phi$ in Eq. (4.2). As in the concentration case, the system can be divided into two regions to solve the flow equations. The net force acting on the body, plus the solution contained within the inner region, is zero. There is one side of the colloid which is exposed to a higher solute concentration which generates a streaming flow towards the lower concentration. From momentum conservation, the solute flow generates the opposite effect on the colloid, which moves following the concentration gradient (for the case of solute adsorption). The phoretic velocity $\boldsymbol{v}_c$ is computed by using the perturbed axisymmetric concentration around the colloid matching the solutions in the inner and outer regions, obtaining:

$$v_c = v_0\left[1 - \frac{(K+H)}{L}\lambda + \mathscr{O}(\lambda^2)\right]. \tag{4.11}$$

In this approximation, the first term corresponds to the Derjaguin limit $L \ll a$:

$$v_0 = \frac{\alpha}{\beta\eta}L^* K, \tag{4.12}$$

[1] As mentioned in Sec. 3.2.2 ϕ only vanishes at the bulk, even if the range of solute-colloid is shorter.

where $\beta = 1/(k_B T)$, η is the shear viscosity and ϕ is the potential of mean force experienced by solutes at a distance $y = r - a$ from the surface of the colloid. K, L^* were introduced in Sec. 3.2.2. The new term H appearing in Eq. (4.11) is proportional to the second moment of the excess solute distribution,

$$H = \frac{\int_0^\infty \frac{1}{2} y^2 [c_s(y) - c_s^B] dy}{\int_0^\infty y [c_s(y) - c_s^B] dy}. \tag{4.13}$$

The correction terms in Eq. (4.11) account for the effect of the curvature of the particle. The above equations apply in the case where there is no hydrodynamic slip on the surface of the colloid (for the inner region solution). However, if solute particles are strongly adsorbed to the colloid, they become immobile, and the result is that the surface of no-slip, and hence the effective colloidal radius, increases.

The importance of Anderson's solution from the perspective of a theoretical and numerical simulation is twofold: first, it depends on the unperturbed concentration distribution around the colloid. Therefore, a quantity that is easy to compute using results from EMD. Second, it explicitly contains physical parameters such as the Gibbs surface excess and the moments of the concentration distribution; thus providing knowledge of the diffuse layer's structure.

The solution presented above was later improved by Anderson & Prieve [16] to include convective transport on the solutes (see also [61, 105]). Anderson & Prieve [60] also studied the diffusiophoresis of a colloidal particle in a solution with strongly adsorbing solutes. More recently, Marbach *et al.* [63] reported the local force balance between the viscous and the forces due to the excess concentration around the colloid. Finally, there is a natural extension to self-propelled particles, first addressed by Golestanian *et al.* [106, 107] and later by Sharifi-Mood *et al.* [62], where they included catalytic reactions at the surface of the colloid.

4.2.1 Marangoni effect and diffusiophoresis

So far, we have described a solid particle or surface in a solution with a chemical potential gradient in solutes. Here, we offer a brief description of what occurs at a liquid-liquid interface and the connection with diffusiophoresis. In what follows, we make the same assumptions as in Sec. 3.2.2 to derive Derjaguin-Anderson expression (see Eq. (3.23)), namely, we suppose an ideal solution in the bulk and low solute concentration. The Marangoni effect is the flow caused by a thermal or concentration gradient parallel to a liquid-liquid interface. For a spherical bubble, Young *et al.* [108] estimated the velocity under the thermal

Marangoni effect. Young's estimates can also describe the solutal Marangoni effect [16, 109], predicting a velocity

$$v_M = \frac{a}{3\eta_d + 2\eta}\left(-\frac{\partial\gamma}{\partial c_s^B}\right)_T \boldsymbol{\nabla} c_s^B \tag{4.14}$$

where a is the radius of the droplet; η_d and η are the viscosities of the fluid inside and outside the droplet. γ is the interfacial tension. The result depends on the interface tension gradient, with the forward pole (in the direction of the gradient) subject to a lower tension than the rear pole. This gradient in tension drives the movement of the droplet towards the region with a higher number of solutes. Notice that if $\eta \to \infty$ the velocity in Eq. (4.14) is zero. Ruckerstein [110] proposed that for a liquid-liquid interface diffusiophoresis also contributes to the movement, and Anderson & Prieve [15] further developed this idea, demonstrating that the velocity for a "drop" is given by

$$v_0 = \left(\frac{a + 3(\eta_d/\eta)L^*}{3(\eta_d/\eta) + 2}\right)\frac{k_B T}{\eta} K |\boldsymbol{\nabla} c_s^B| \,. \tag{4.15}$$

In the limit of $a \gg L \sim L^*$, for a liquid droplet ($\eta_d/\eta \to 1$), we recover Eq. (4.14) by using Gibbs adsorption equation

$$\left(\frac{\partial\gamma}{\partial c_s^B}\right)_T = -\frac{k_B T}{c_s^B}\Gamma = -k_B T K \,. \tag{4.16}$$

Therefore, the velocity does not depend on the interfacial structure and is proportional to the radius, which confirms Young's results. When the viscosity $\eta_d \to \infty$, we recover the expression in Eq. (4.12).

4.3 Simulations

Conceptually, the most straightforward way of simulating diffusiophoresis would be to carry out NEMD with an imposed concentration gradient, following a procedure similar to Heffelfinger & Van Swol [79] and Thompson & Heffelfinger [83](see Sec. 2.4.2). Nonetheless, there are several drawbacks associated with this approach for modelling diffusiophoresis, the most significant one being that periodic boundary conditions are incompatible with the existence of constant concentration gradients, as advection deforms the concentration profiles [74, 75]. However, in analogy with simulations of systems in a homogeneous electrical field, as we did for diffusio-osmosis, we can replace the gradient of a chemical potential by an equivalent constant force per particle. Such a force is compatible with periodic boundary conditions [27, 48].

In this section, we perform both BD-NEMD and FD-NEMD for a colloidal particle. In the former, we impose an explicit concentration gradient, and in the later, we apply a microscopic force equivalent to the chemical potential gradient.

4.3.1 Boundary-Driven Non-Equilibrium Molecular Dynamics

For our BD-NEMD, we used a double control volume semi-grand canonical algorithm DCV-SGCMC[2]. The box size is (51.30 x 20.52 x 30.78) (in units of σ_0). A colloid was fixed in the centre of the simulation box (see Fig. 4.2) by placing a single Lennard-Jones particle with $\sigma_{cs} = \sigma_{cf}$ = 3.23 σ_0, where the subscript c denotes the colloid. The concentration gradient was created by using two reservoirs of particles. The *source* region at $c_s^B = 0.6\sigma_0^{-3}$ and the *sink* at $c_s^B = 0.15\sigma_0^{-3}$. The difference in concentration between the reservoirs is equivalent to $\nabla\mu_s \sim 0.06$. The imposed concentration gradient is linear when there is no preferential interaction between the colloid and the solutes $\varepsilon_{cs} = 1.0$ (see Fig 4.3). Finally, it is worth pointing out that the particle identity swap does not create a fluid density gradient in the bulk, as we suppose an ideal solution.

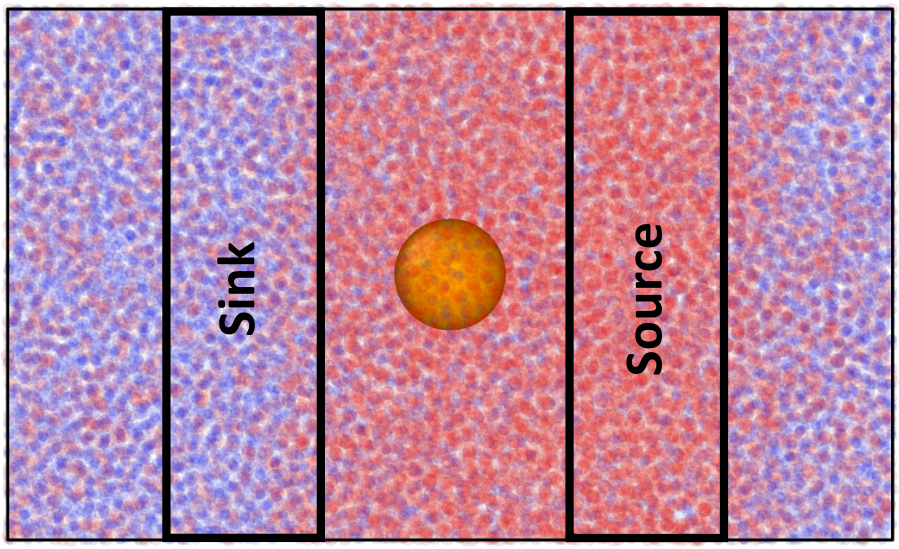

Fig. 4.2 Dual control volume simulation box used for the boundary-driven non-equilibrium simulations. In both control volumes, the concentration for each particle species was fixed, with the *sink* and *source* indicating the low and high solute concentration regions respectively. The distance between the reservoirs is $\Delta x^{\text{ss}} = 12x_l$ and the length of the control volumes in the x direction is $\Delta_x^{\text{cv}} = 3x_l$, where $x_l = 5^{1/3}\sigma_0$.

[2]In Sec. 2.4.2 we described the method with a grad-canonical ensemble (DCV-GCMC). However, here we use a semi-grand canonical ensemble (see [77]). This approach is more efficient as particles are not inserted/removed, but their identities are swapped.

We performed the simulations using LAMMPS [96], with a 12-6 LJ potential as described in Sec. 3.3.1. The indices i and j in Eq. (3.56) denote the particle types in our simulations: solutes (s), solvents (f) and colloid (c). We assume that solutes and solvents behave as an ideal mixture in the bulk. Therefore, we choose the same Lennard-Jones interaction for the particle pairs ss, sf, ff with $\varepsilon_{ij}^{LJ} = \varepsilon_0$ and $\sigma_{ij}^{LJ} = \sigma_0$. We also apply these same parameters for the colloid-solvent interaction cs. The colloid-solute interaction strength ε_{cs}^{LJ} was varied to control the degree of solute adsorption or depletion around the colloidal particle. For simplicity, we kept σ_{cs}^{LJ} equal to σ_0. We initialised the system with a solute/solvent ratio $c_s^B/c_f^B = 1$ and an average solution density in the box of $\bar{c} = 0.75\varepsilon_0^{-3}$. We swapped particle identity in the reservoirs every 20 time steps, with a time step of $\Delta t = 0.05\tau$. We let the system equilibrate for 10^7 steps. By doing this, we achieve both an equilibration of solutes around the colloid and the desired concentration gradient between the control volumes. The equations of motion were integrated using a velocity-Verlet algorithm, and we kept the temperature of the system at $k_BT/\varepsilon_0 = 1.0$ using a Nosé-Hoover thermostat [87]. After the equilibration, we ran 10^7 production steps to sample the flow velocity around the colloid and the concentration distribution for each species.

Results

In Fig. 4.3 we show the solute concentration profiles for different colloid-solute interactions ε_{cs}. As soon as phoresis starts, i.e. for $\varepsilon_{cs}^{LJ} \neq 0$, the concentration gradient becomes non-linear due to advection. As a result, the local concentration gradient at the location of the colloid decreases (see also [74]). In the BD-NEMD simulation, the colloidal particle is fixed with respect to the two reservoirs. This setup resembles more the conditions of a diffusio-osmotic experiment. In fact, similar concentration profiles were observed by Lee *et al.* [111] when studying the diffusio-osmotic flow caused by solute gradients in nanochannels.

We can show that the concentration distribution becomes exponential. We consider the colloidal particle fixed in our simulation box and a steady velocity field $\boldsymbol{v}$ in the fluid. We can express the flux of species i as a sum of a purely diffusive flow and the convective contribution,

$$\boldsymbol{J}_i = -D_i \boldsymbol{\nabla} c_i^B + \boldsymbol{v} c_i^B \, . \tag{4.17}$$

In order to have steady flow, the concentration has to be

$$c_i(x) = \text{const}_a \, e^{(v/D_i)x} + \text{const}_b \, , \tag{4.18}$$

with $D_s/v = 1/k$ being a characteristic length of the system. const_a and const_b are given by the boundary conditions at the source and sink regions of the system (see Fig. 4.2).

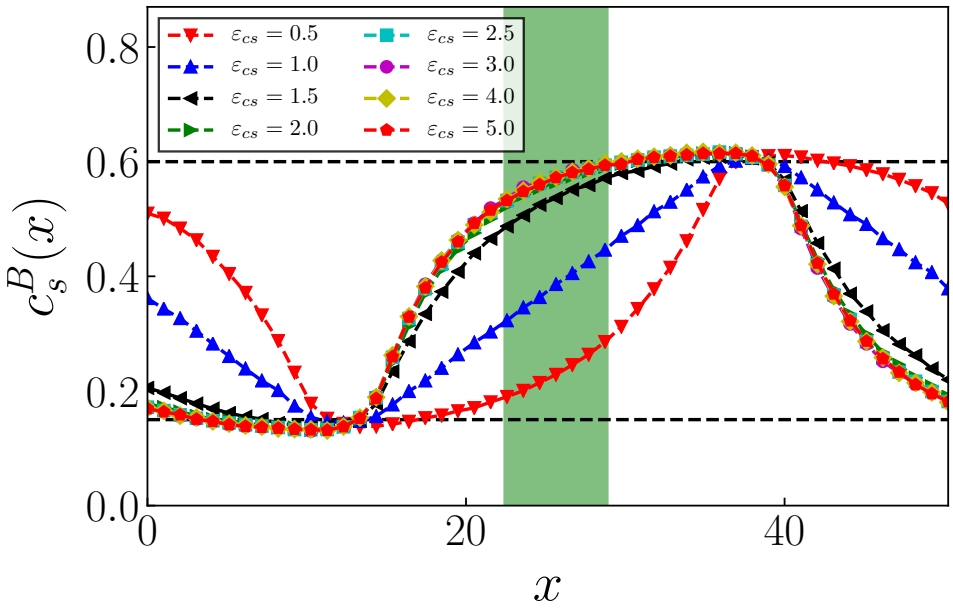

Fig. 4.3 Solute concentration profile for a constant concentration gradient. We show the results for difference phoretic flow velocities, corresponding to several values of ε_{cs}. We measure the concentration profiles at a lateral distance of at least 10σ from the colloid, where the colloid does not directly perturb the concentration profile. The shaded region represents the x position of the colloid, which we show to emphasize the asymmetry in the concentration distribution created by the advection.

If we restrict the analysis to the solutes and set $c_s(0) = c_s^{\text{sink}}$ and $c_s(\Delta x^{\text{ss}}) = c_s^{\text{source}}$, with Δx^{ss} being the distance between the control volumes, we have:

$$c_s^B(x) = c_s^{\text{sink}} + \frac{e^{kx} - 1}{e^{k\Delta x^{\text{ss}}} - 1} \Delta c_s^B \,, \tag{4.19}$$

with $\Delta c_s^B = c_s^{\text{source}} - c_s^{\text{sink}}$. We can define the Péclet number for the BD-NEMD simulations as $Pe^{BD} = k\Delta x^{\text{ss}} = v\Delta x^{\text{ss}}/D_s$. In Fig. 4.4 we show Pe^{BD} for the different interactions ε_{cs}. Even for the smallest non-zero phoretic flow Pe^{BD} is not negligible, therefore convection plays an important role. Khair [105] showed that the particle velocity decreases monotonically with increasing Pe (we discuss below that this is the case if we compare with FD-NEMD) and that the concentration distribution around the colloid becomes fore-aft asymmetrical. Anderson [16] argues that the reduction of speed by convective effects is created by the additional pressure over the front hemisphere of the colloid ($\theta = 0$) which opposes it to move forward. Wei *et al.* [74] found that solutes near $\theta = 0$ or $\theta = \pi$ have less mobility than those close to $\theta \pm \pi/2$ therefore, the stagnant excess of solutes interacting with the colloid is what causes the phoretic slowdown.

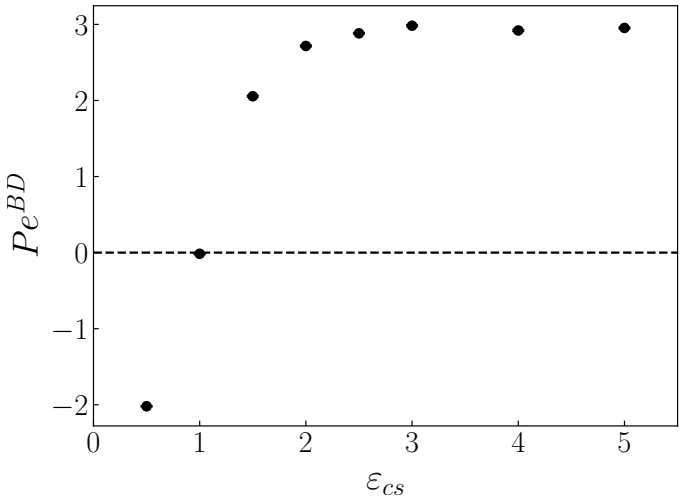

Fig. 4.4 Péclet number Pe^{BD} for the diffusiophoretic flow with several colloid-solute interaction strengths ε_{cs}. Note that, even for the smallest non-zero phoretic flow velocities $Pe^{BD} > 1$.

4.3.2 Field-Driven Non-Equilibrium Molecular Dynamics

For our FD-NEMD we used a simulation box (20.52 x 20.52 x 30.78) (in units of σ_0). Snapshot of both the FD-NEMD and the BD-NEMD are shown in Fig. 4.5.

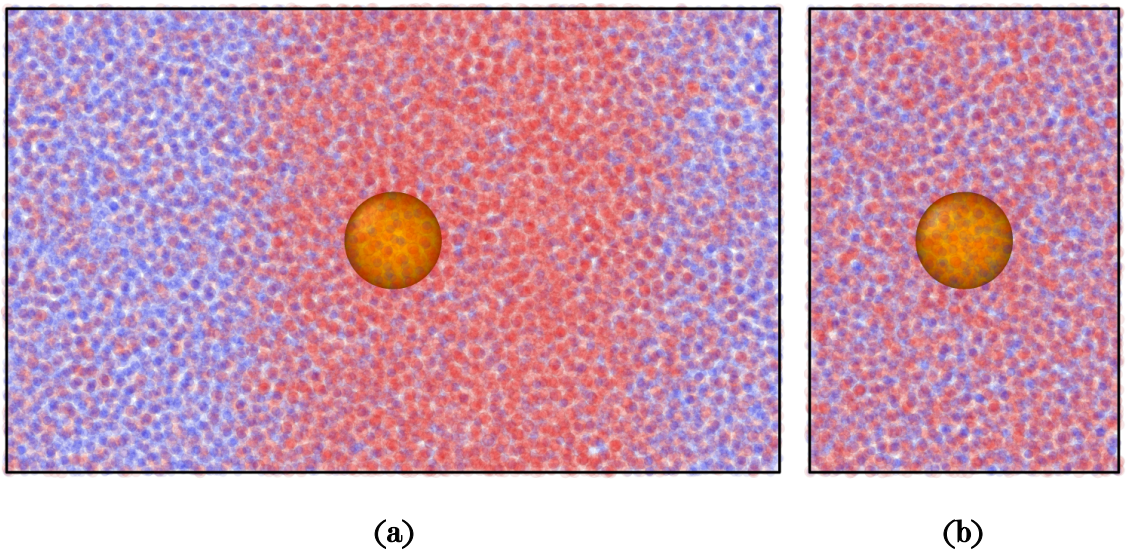

Fig. 4.5 Simulation boxes for (a) the explicit (BD-NEMD) and (b) the implicit gradient systems (FD-NEMD).

Note that the deformation of the concentration profile in Fig. 4.5(b) FD-NEMD is barely visible. This observation illustrates the advantage of using colour forces rather than explicit gradients. In contrast, in Fig. 4.5(a) BD-NEMD, the colloid is not in the centre of the concentration profile (if it were, it would be at the red-blue boundary).

Initialisation

The initial system was created following the same procedure as in the BD-NEMD simulations. To equilibrate, in this case, we imposed semi-grand canonical swap moves between s and f in the entire box. We attempted to swap 10^4 particle identities every 10 steps for the first 10^5, reaching an equilibrium distribution of solutes around the colloid and an equimolar solution in the bulk. This equilibration step is crucial as our aim to carry out simulations under conditions where the composition of the bulk fluid was kept fixed, even as we varied the colloid-solute interaction ε_{cs}. In Fig. 4.6, we show the equilibrium distributions for each species in specific cases of depletion and adsorptions of solutes around the colloid.

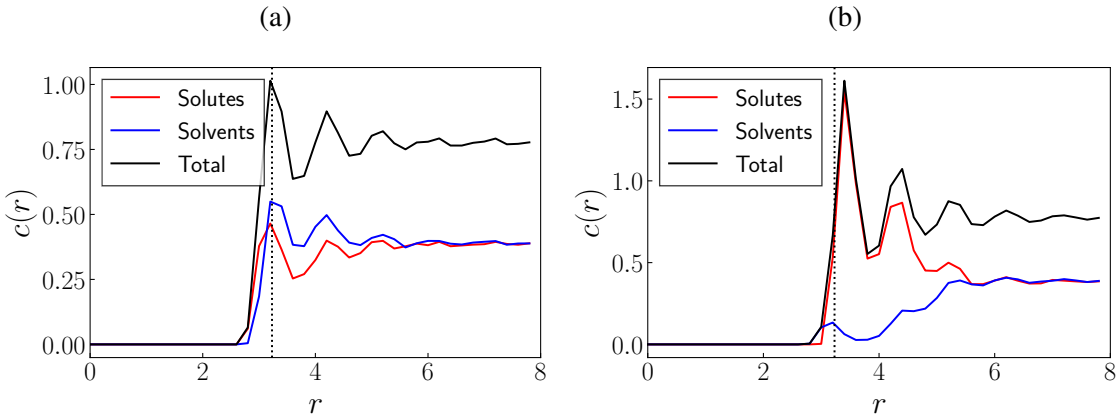

Fig. 4.6 Concentration radial distributions around a colloid. (a) when there is depletion of solutes, $\varepsilon_{cs} = 0.5$ (b) for strong adsorption, $\varepsilon_{ms} = 5.0$. Notice that there is an equimolar binary solution in the bulk. The profiles were computed using bins with $\Delta r = 0.2$. The vertical dashed line represents $r = \sigma_{cs}$.

Based on the results in Fig. 4.6 we can define a bulk region where the concentration of solutes and solvents is constant. This region is shown in Fig. 4.7 and its relevance will be discussed below.

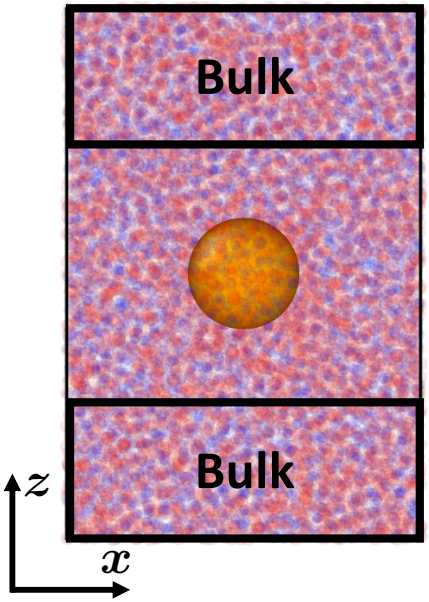

Fig. 4.7 Simulation box showing solutes (red), solvents (blue) and colloid (orange). The bulk regions are shown inside black boxes. They are localised at $|z - z_c| \geq 10$, where the centre of the colloid is at z_c. We assume that the solute and solvent concentrations unperturbed by the presence of the colloid in the bulk.

Results

As discussed previously, we represent the chemical potential gradients by equivalent external forces that are compatible with the periodic boundary conditions. They are such that a) there is no net force on the bulk solution away from the colloid and b) there is no net force on the system as a whole. These two conditions imply that there is only one independent force that can be defined in the system. In the present case, we chose to fix the force on the solutes F_s^μ. We set it by using the parameters in the BD-NEMD simulation box at the position where the concentration ratio $c_s^B/c_f^B = 1$ (assuming a linear concentration distribution). Therefore, $F_s^\mu = 0.06\varepsilon_0/\sigma_0$.

Having specified the force on the solutes, the force on the solvent particles $\mathbf{F}_f^\mu$ follows from mechanical equilibrium in the bulk:

$$\mathbf{F}_s^\mu N_s^B + \mathbf{F}_f^\mu N_f^B = 0, \tag{4.20}$$

N_s^B, N_f^B denote the number of solutes and solvent in the bulk region. Once the forces in the bulk are specified, we obtain the phoretic force on the colloid $\mathbf{F}_c^\mu$ by imposing mechanical equilibrium in the whole system,

$$\mathbf{F}_c^{\mu} = -(\mathbf{F}_s^{\mu} N_s + \mathbf{F}_f^{\mu} N_f), \tag{4.21}$$

N_s, N_f refer to the number of solutes and solvents in the whole system. This equation expresses the fact that there can be no net external force on the fluid: if there were, the system would accelerate without bound, as there are no walls or other momentum sinks in the system. Eq. (4.21) establishes a connection between all chemical potential gradients (or the corresponding microscopic forces), which must be balanced throughout the system as the phoretic flow cannot cause bulk flow.

In practice, during the FD-NEMD simulations, we need to ensure that the bulk region remains unperturbed by the colloid. We did this in two different ways: we let the colloid move free, translating the coordinates of all the particles in the system such that the colloid is always in the centre of the box. Alternatively, we can constrain the colloid to the centre of the system and measure the flow around it. In Fig. 4.8, we show a comparison between the two approaches, concluding that both give equivalent results. It worth noticing that the velocity is non-monotonic. The reason is that initially, ε_{cs} increases the excess of solutes around the colloid, which, in turn, increases the phoretic velocity as expected in the linear regime. However, for large ε_{cs}, the closest solutes to the colloid are tightly bound and lose their mobility. Hence, they stop contributing to the flow around the colloid. We will study in more detail this non-monotonic behaviour of the velocity(mobility) in Sec 5.2.4.

Due to the finite size of the bulk, there are inevitably fluctuations in the composition of this domain. These variations would lead to unphysical velocity fluctuations in the bulk (unphysical because in the thermodynamic limit this effect goes away), creating noise in the observed phoretic flow velocity. To suppress this effect, we could either adjust the composition in the bulk domain at every time step or recompute the forces on the solvents $\mathbf{F}_f^{\mu}$) such that the external force on the bulk domain is always rigorously equal to zero (this also adjusts the force on the colloid $\mathbf{F}_c^{\mu}$). We opted for the latter approach as particle swaps would affect the stability of the MD simulations.

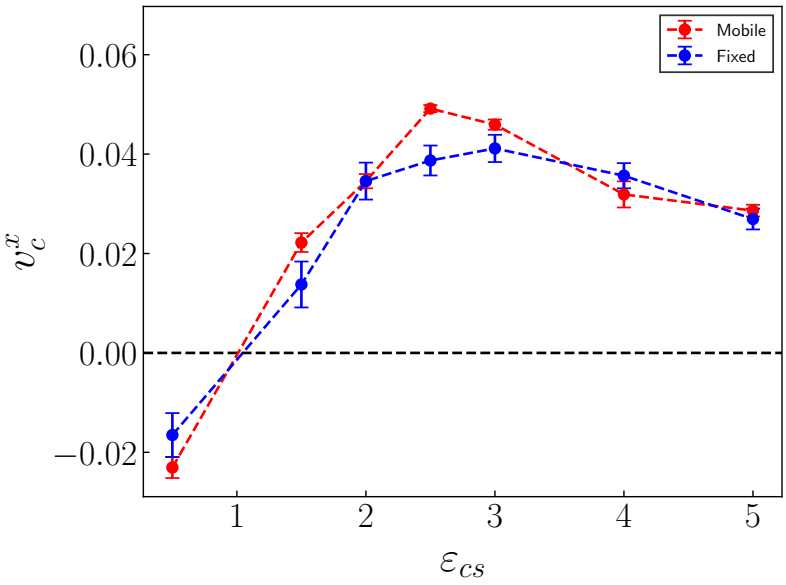

Fig. 4.8 The phoretic velocity of the colloid v_c^x with several colloid-solute interaction strengths ε_{cs}. The red line shows the results when the colloid moves freely, and v_c^x is the velocity of the colloid relative to the bulk fluid. In blue, we show the results when the colloid position is fixed, and v_c^x is minus the velocity of the fluid flow in the bulk.

Comparison with theoretical predictions

Using Eq. (4.11) to predict the diffusio-phoretic velocity requires the definition of the colloidal radius a. This radius indicates the position of the surface from where we perform the integration of the excess distribution moments. This position is critical for the theoretical calculations and even more with the curvature correction terms, as they depend on the higher moments of the distributions. As a first approximation, we can define $a = \sigma_{cs}$. Additionally, we can include the effect of the solute-colloid interaction to a certain level by using the hydrodynamic radius R_H defined by the Stokes-Einstein relation:

$$R_H \equiv \frac{k_b T}{\zeta_c \pi \eta D_c} , \tag{4.22}$$

where $\zeta_c = 4$ for slip-boundary condition and $\zeta_c = 6$ for non-slip boundary conditions. The viscosity η and the diffusion coefficient of the colloid D_c are computed as described in Appendix B. In Fig. 4.9 we show that the diffusion coefficient decreases as the ε_{cs} increases. The reason for this behaviour is that the effective hydrodynamic radius of the colloid grows as it drags more solutes with it when the adsorption increases. The diffusion coefficient reaches a plateau for large εcs when increasing the interaction strength does not modify the number of solutes influenced by the presence of the colloid anymore.

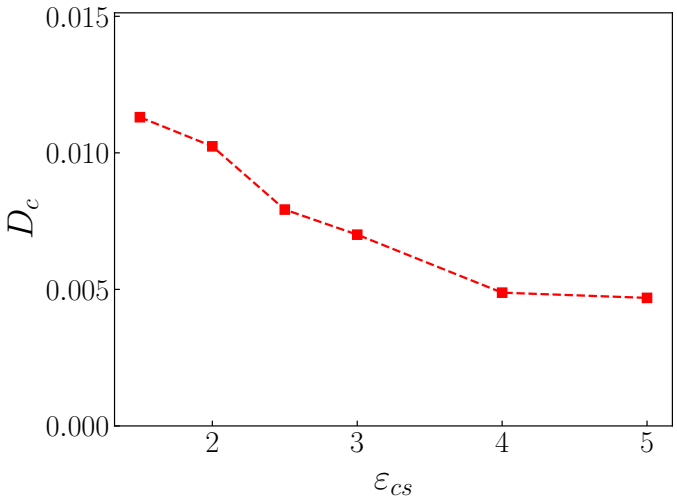

Fig. 4.9 Colloid diffusion coefficient D_c for solute adsorption at the surface $\varepsilon_{cs} \geq 1$.

In Fig. 4.10 we show the estimates of the diffusiophoretic velocity using different colloidal radius a for the theoretical expression in the Eq. (4.11).

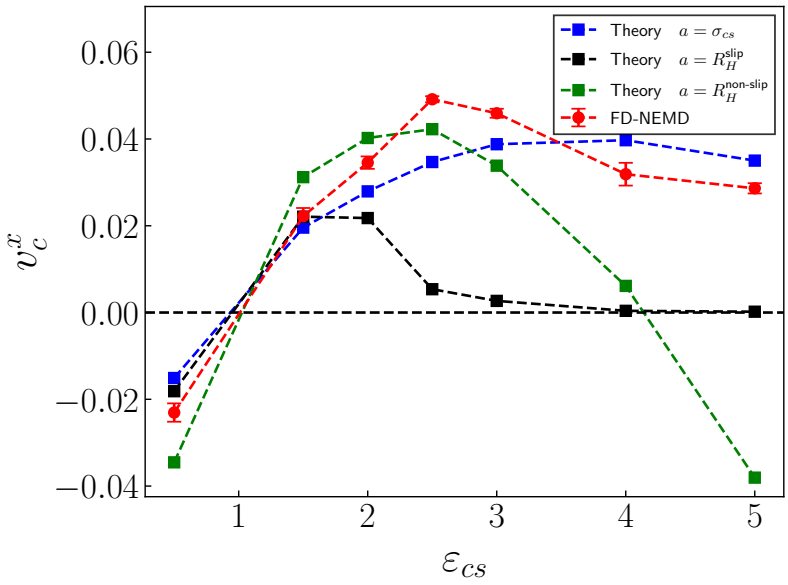

Fig. 4.10 Phoretic velocity of the colloid v_c^x with several colloid-solute interaction strengths ε_{cs}. The curves show the results obtained with FD-NEMD simulations compared to theoretical estimates with different values for a. The hydrodynamic radius R_H was obtained by assuming Stokes-Einstein (Eq. (4.22)) with both slip and non-slip condition.

The results show how sensitive the theoretical prediction is to the parameter choice, stressing the importance of the NEMD calculations. We see that the estimates using the

hydrodynamic radius with both slip or non-slip boundary conditions fail. The slip boundary condition over-estimates the radius once ε_{cs} increases, penalising the integrals of the moments of the concentrations distributions (see Fig. 4.6). The non-slip boundary condition fails for large ε_{cs} as the curvature correction term becomes larger than v_0 in Eq. (4.11).

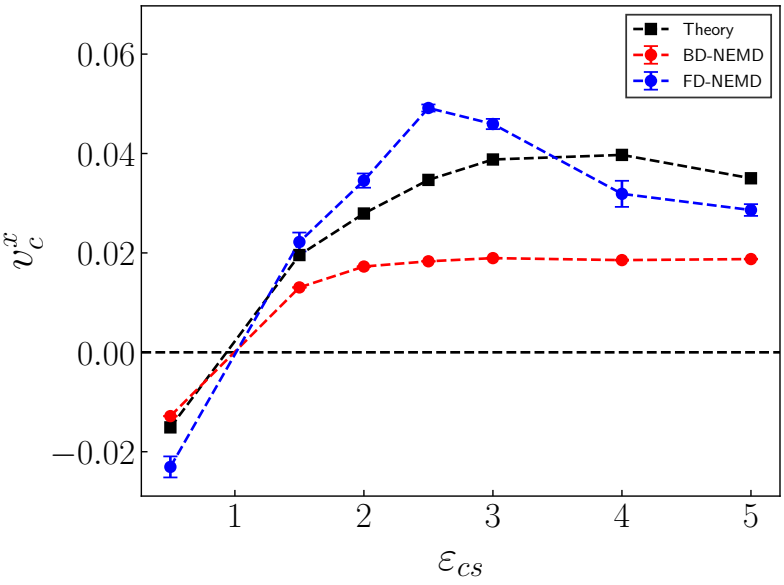

Fig. 4.11 Phoretic velocity v_c^x for several colloid-solute interaction strengths ε_{cs}. We compare the results for an explicit concentration gradient (BD-NEMD), FD-NEMD and theoretical predictions with $a = \sigma_{cs}$.

Finally, in Fig. 4.11 we show the results obtained using the BD-NEMD and FD-NEMD, together with the theoretical predictions $a = \sigma_{cs}$.

The results show that the BD-NEMD method is only suitable for small phoretic effects. Whereas, FD-NEMD simulations make it possible to suppress most advective effects on diffusiophoresis. The reason is that in the former $Pe^{BD} = \Delta x^{ss} v_c / D_s$, and in the latter $Pe^{FD} = a v_c / D_s$ with $\Delta x^{ss}/a \sim \mathcal{O}(10)$ for our simulations. Sharifi *et al.* [112] tried to overcome this limitation by enforcing the concentration profiles to be linear, but at the expense of introducing (unphysical) *sources/sinks* of solute particles throughout the simulation box as show in Fig. 4.12.

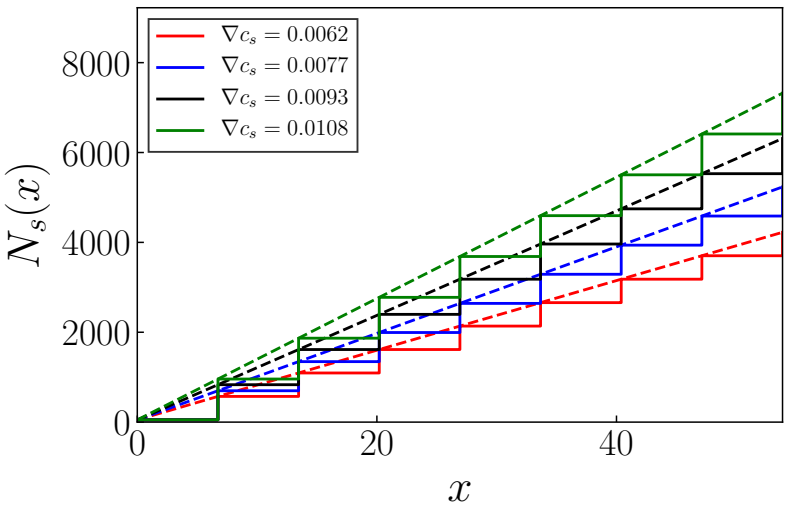

Fig. 4.12 Solute number N_s in the simulation box by Sharifi *et al.* [112]. The simulation box is divided into eight sub-volumes along the concentration gradient direction. The imposed distribution (in continuous lines) is maintained by swapping particle identities on each subsystem. The target concentration is shown in dashed lines.

4.4 Conclusions

We performed molecular dynamics simulation on the diffusiophoresis of colloids in a fluid mixture under the influence of a concentration gradient of solutes. We used two NEMD approaches: first, we imposed an explicit concentration gradient by using two reservoirs in the simulation box. Second, we extended the FD-NEMD method to non-planar geometries for the first time [74, 75]. We find large distortions of the concentration profile due to the fluid flow ($Pe^{BD} > 1$). These advective effects diminish for small gradients when the signal-to-noise ratio becomes poor. As a result, the comparison between simulation with explicit gradients and with colour forces is only fair. The difficulty in performing simulations with real concentration gradients illustrates the advantage of the FD-NEMD technique. Using colour forces, we obtained similar results by either keeping the colloid fixed or moving freely. Hence, this technique allows for simulating moving objects compatible with periodic boundary conditions. Finally, our results reveal a non-monotonic relation between the diffusiophoretic velocity and the interaction strength between the colloid and the solute. The findings imply that, in the strong interaction regime, phoretic mobility decreases with increasing colloid-solute interaction strength. We will investigate this effect in detail in the following chapter.

Chapter 5

Polymer diffusiophoresis

"It is nice to know that the computer understands the problem. But I would like to understand it too."

Eugene Wigner

5.1 Introduction

In previous chapters, we studied diffusio-osmosis under Derjaguin approximation [14, 93]. For small colloids, this theory was not valid, as we could not describe the colloid-fluid interface as locally flat since its radius was relatively short compared to the diffuse layer thickness. Therefore, we introduced Anderson's extension to include curvature effects for the diffusiophoresis of spherical particles in Sec. 4.2. There is yet another situation where the Derjaguin-Anderson approach is questionable, namely in the case of particles without a well-defined surface. One particularly notable example is the case of polymer diffusiophoresis: molecules that have a fluctuating shape and an intrinsically fuzzy surface. One manifestation of this fuzziness is the fact that the magnitude of the Kirkwood approximation for the hydrodynamic radius R_H of a long self-avoiding polymer is about 63% of the radius of gyration R_g [113]. This difference implies that there is a density inhomogeneity in a self-avoiding polymer, which allows penetration of hydrodynamic flow fields and solutes into its outer "fuzzy " layer. Therefore, it is difficult to describe a polymer as a solid sphere surrounded with fluid, and Derjaguin-Anderson approach is questionable. The lack of predictive power of the colloidal approximation was pointed out previously by experiments with λ-DNA by Palacci *et al.* [36, 37].

An additional factor rendering polymer diffusiophoresis difficult is that, unlike in the case of colloids, it cannot be assume that the size of polymers subject to diffusiophoresis is independent of the polymer-solute interaction.

In this chapter, we report MD simulations of diffusiophoretic transport of short polymers. Specifically, we apply NEMD simulations using a microscopic force acting on each species and examine the effect of interaction parameters between the monomer and the solute on the induced diffusiophoretic velocity of the polymer. Our simulations reveal, as in the case of colloids, a non-monotonic dependence of the phoretic mobility M_{ps} on ε_{ms}, the interaction strength between the monomers and solute. We have investigated the influence of the size of the polymer on its diffusiophoretic mobility. We found a weak polymer-size dependence of mobility. We compare these findings with the corresponding theoretical predictions for a colloidal particle.

5.2 Simulation

We performed non-equilibrium Molecular Dynamics (NEMD) simulations using LAMMPS [96]. In *most* simulations, particles interact via a 12-6 Lennard-Jones potential (LJ) as described in Sec. 3.3.1

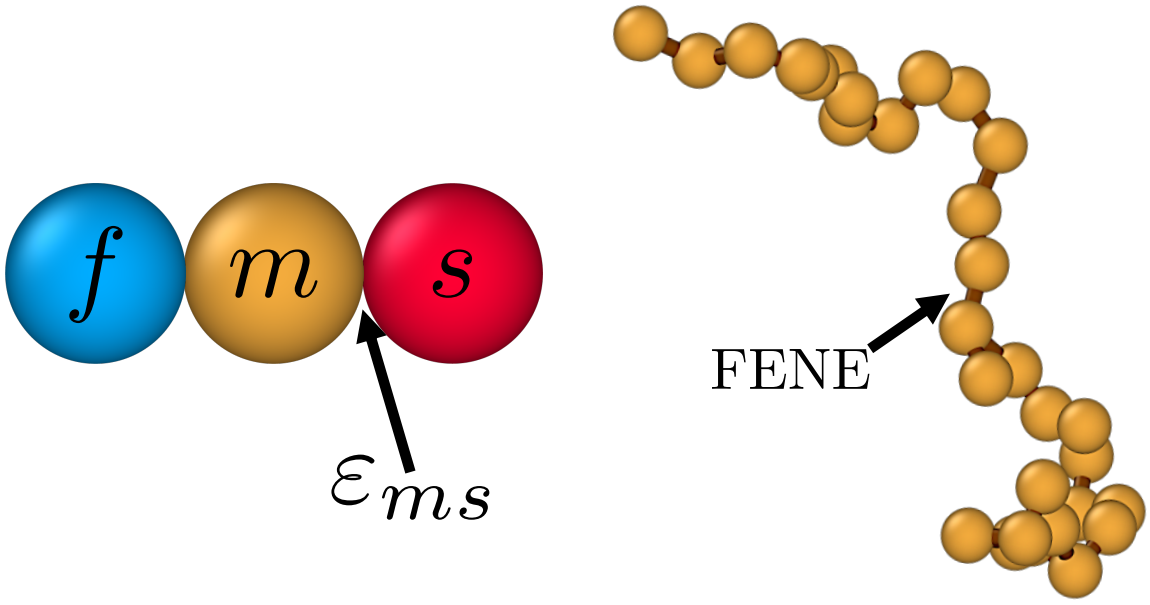

Fig. 5.1 The system is made of solvents f, solutes s and monomers m. The interaction between consecutive monomers is given by a FENE potential. We tune the interaction between monomers and solutes ε_{ms}^{LJ} to control diffusiophoresis.

The indices i and j in Eq. (3.56) denote the particle types in our simulations: solutes (s), solvents (f) and monomers (m) (see Fig 5.1). To keep the model as simple as possible, we assume that in the bulk the solute and solvent behave as an ideal mixture. We therefore choose the same Lennard-Jones interaction for the particle pairs ss, sf, ff with $\varepsilon_{ij}^{LJ} = \varepsilon_0$ and $\sigma_{ij}^{LJ} = \sigma_0$. We use these same parameters also for the monomer-solvent interaction ms. The monomer-solute interaction strength ε_{ms}^{LJ} was varied to control the degree of solute adsorption or depletion around the polymer. Yet, we kept σ_{ms}^{LJ} equal to σ_0. For the monomer-monomer interaction, we use a purely repulsive Weeks-Chandler-Andersen potential [99], i.e. a Lennard-Jones potential truncated and shifted at the minimum of the LJ potential, $r_c = 2^{1/6}\sigma_0$. For all other interactions, $r_c = 2.5\sigma_0$. Finally, neighbouring monomers were connected by a finite extensible nonlinear elastic (FENE) anharmonic potential $U_{FENE}(r)$, [114, 115]

$$U_{FENE}(r) = -\frac{kR_0^2}{2}\ln\left[1-\left(\frac{r}{R_0}\right)^2\right], \tag{5.1}$$

with $k = 7\varepsilon_0/\sigma_0^2$ and $R_0 = 2\sigma_0$. In what follows, we use the mass m_0 of all the particles (s,f and m) as our unit of mass and we set our unit of energy equal to ε_0, whilst our unit of length is equal to σ_0, all other units are subsequently expressed in term of these basic units. As a result, forces are expressed in units ε_0/σ_0, and our unit of time is $\tau \equiv \sigma_0\sqrt{m_0/\varepsilon_0}$.

5.2.1 Equilibration

We studied the diffusiophoresis of a single polymer chain composed of 30 monomers, $N_m = 30$, suspended in an equimolar ideal mixture of solute and solvent molecules. The initial simulation box dimensions were (20 x 20 x 30) (in units of σ_0) and the number of fluid particles was 8748. After equilibration, chemical potential gradients were applied along the x-axis. We distinguished two types of domains in the simulation box: one periodically repeated domain with width $20\sigma_0$ in the z-direction centred around the polymer's centre of mass in the z-coordinate. The remainder of the system (a domain with width $10\sigma_0$), contains only bulk fluid (see Fig. 5.2). The system is periodically repeated in each direction

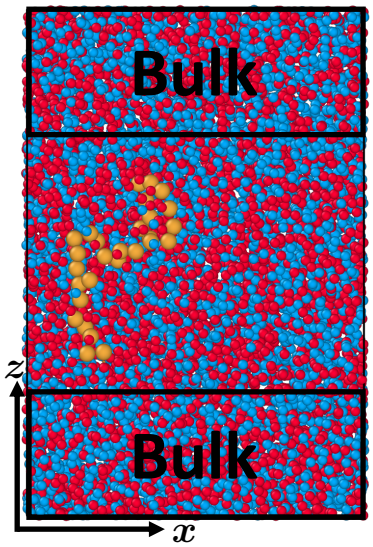

Fig. 5.2 Simulation box showing solutes (red), solvents (blue) and monomers (orange). The bulk regions are shown inside black boxes. In the bulk, the solute and solvent concentrations are assumed to be unperturbed by the presence of the polymer.

In Fig. 5.3, we show the concentration distribution measured from the centre of mass of the polymer in the radial direction for $\varepsilon_{ms} = 1.5$. The results show that for $r > 7\sigma_0$, the solution is unperturbed by the presence of the polymer.

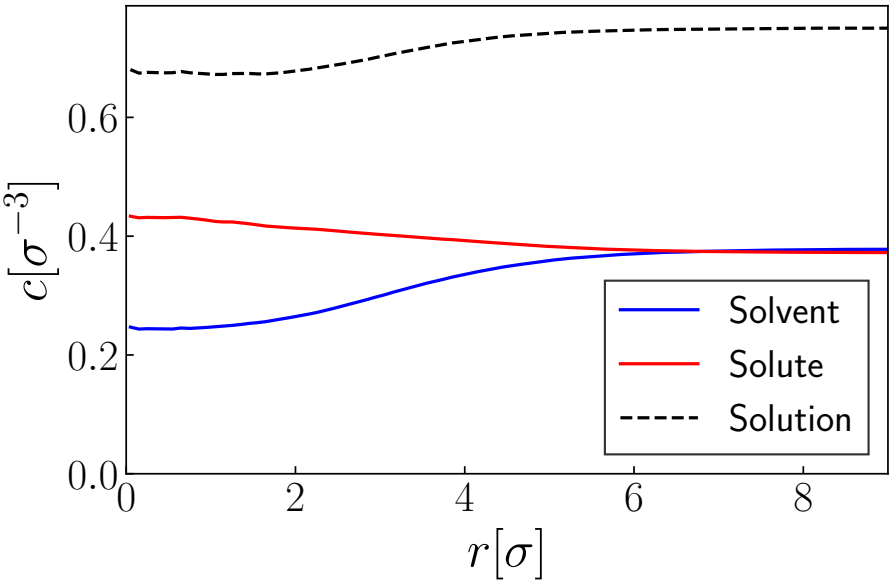

Fig. 5.3 Concentration of solvent, solute, and solution as a function of radial coordinate from the centre of mass of the polymer for $\varepsilon_{ms} = 1.5$.

Our goal was to carry out simulations under conditions where the composition of the bulk fluid was kept fixed, even as we varied the monomer-solute interaction. Moreover, we prepared all systems at the same hydrostatic pressure. Therefore, we performed NPT simulations using a Nosé-Hoover thermostat/barostat [87]. The equations of motion were integrated using a velocity-Verlet algorithm with a time step $t = 0.005\tau$. After the relaxation of the initial configuration, the box was allowed to fluctuate in the y direction, fixing $k_B T/\varepsilon_0 = 1.0$ and $P\sigma_0^3/\varepsilon_0 = 1.0$ for 2×10^4 steps.

During the NPT equilibration, fixing the bulk concentration of the liquid requires a precise protocol, in particular in cases where the solute binds strongly to the polymer. In our simulations, we accelerated the equilibration of the solute adsorption on the polymer by attempting to swap solvent and solute molecules 10^4 times for every MD step throughout the simulation box. Simultaneously, we exchanged solutes and solvents in the bulk, to ensure that adsorption on the polymer would not deplete the solute concentration in the bulk. To this end, we swapped solutes and solvents in the bulk every 200 steps such that the bulk solute concentration remained fixed at $c_s^B \approx 0.376$. It is worth pointing out that particle swaps occurred only during the equilibration.

5.2.2 Field-Driven Non-Equilibrium Molecular Dynamics

Once the system is at a pre-determined pressure and bulk composition, we study the effect of chemical potential gradients on the phoretic motion of the polymer in NVT simulations. These forces are such that there is no net force on the system as a whole, and there is no net force on the bulk solution away from the polymer. These two conditions imply that there is only one independent force to be defined in the system. In the present case, we fixed the force on the solutes $\mathbf{F}_s^\mu$, which was varied between 0 and 0.1 ε_0/σ_0 for different runs. During all the FD-NEMD simulations, we employed a dynamical definition of the bulk and polymer domains, such that the z-coordinate of the centre of mass of the polymer is always in the middle of the polymer domain. We also constrained the polymer position to the centre of the box by using two different methods, and the results were equivalent (see Sec. D.1)). This procedure ensures that the "bulk" region remains unperturbed by the polymer. Having specified the force on the solute, the force on the solvent particles $\mathbf{F}_f^\mu$ follows from mechanical equilibrium in the bulk in Eq. (5.3) (see Fig. 5.2):

$$\mathbf{F}_s^\mu N_s^B + \mathbf{F}_f^\mu N_f^B = 0, \tag{5.2}$$

where N_s^B, N_f^B denote the number of solutes and solvent in the bulk region. Once the forces in the bulk have been specified, the phoretic force on the polymer $\mathbf{F}_p^\mu$ is obtained by imposing force balance on the system as a whole

$$\mathbf{F}_p^\mu = -(\mathbf{F}_s^\mu N_s + \mathbf{F}_f^\mu N_f), \tag{5.3}$$

In simulations, it is convenient to work with a force per monomer, rather than a force on the centre-of-mass of the polymer: $\mathbf{F}_m = \mathbf{F}_p^\mu / N_m$, where N_m denotes the number of beads in the polymer. Eq. (5.3) establishes a connection between all chemical potential gradients (or the corresponding microscopic forces), which must be balanced throughout the system as the phoretic flow cannot cause bulk flow.

5.2.3 Phoretic velocity

In Fig. 5.4, the polymer velocities in the direction of the gradient v_p^x are plotted for three different pairs of LJ parameters. When there is adsorption of solutes around the polymer ($\varepsilon_{ms}^{LJ} = 1.5$), the polymer follows the gradient, migrating towards regions where the solute concentration is higher. Conversely, when there is depletion ($\varepsilon_{ms}^{LJ} = 0.5$) the polymer will move in the opposite direction. As a null check, we also performed simulations for the case where the $\varepsilon_{ms}^{LJ} = \varepsilon_{mf}^{LJ}$. In that case, there should be no phoresis, as is indeed found in the data shown in Fig. 5.4. The inversion of the velocity depending on the sign of the monomer-solute interaction is expected on the basis of irreversible thermodynamics [16] and has previously been observed in simulations of for nano-dimers, using hybrid molecular dynamics-multiparticle collision (MD-MPC) dynamics [29, 31].

The figure also shows that our simulations appear to be in the linear regime, as the magnitude of the phoretic velocity increases linearly with the strength of the applied field.

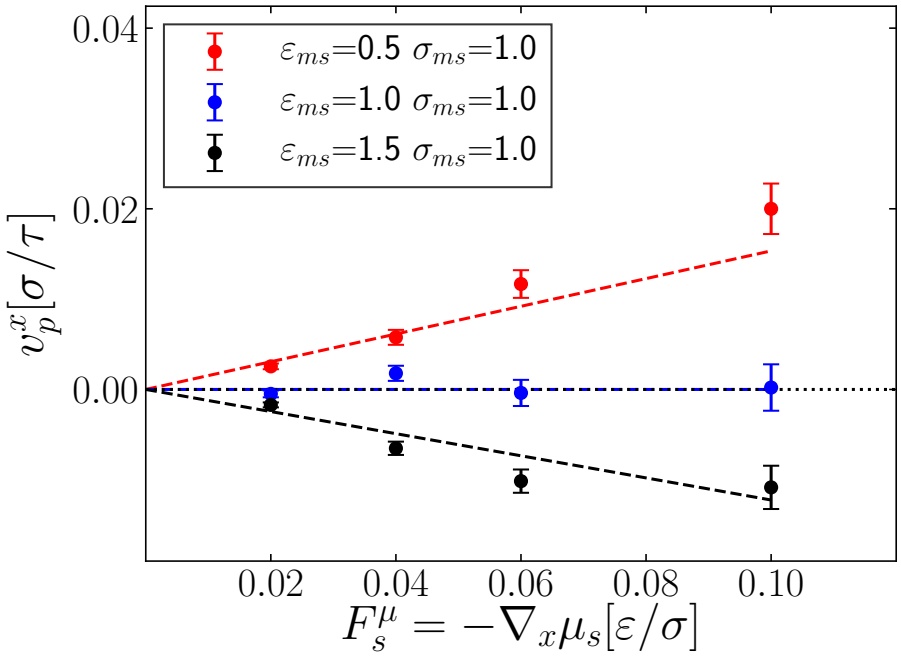

Fig. 5.4 Polymer velocities in the direction of the gradient for different LJ interactions $(\varepsilon_{ms}^{LJ}, \sigma_{ms}^{LJ})$ vs the force applied on the solute particles.

5.2.4 Mobility dependence on the interaction

The mobility M_{ps} of a polymer moving under the influence of a gradient in the solute chemical potential is defined through:

$$\mathbf{v}_p^x = M_{ps} \nabla_x \mu_s. \tag{5.4}$$

We can compute M_{ps} as a function of the polymer-solute interaction strength from the slope of the v_p^x *vs.* $\nabla_x \mu_s$ plots, such as the ones shown in Fig. 5.4. This procedure allows us to obtain M_{ps} as a function of the monomer-solute interaction strength ε_{ms}^{LJ}. We stress that whilst we determine M_{ps} by varying $\nabla_x \mu_s$, we keep the bulk composition of the mixture fixed (as well as the temperature and the pressure). The resulting relation between ε_{ms}^{LJ} and M_{ps} is shown in Fig. 5.5. As expected, M_{ps} is linear in ε_{ms}^{LJ} when $\varepsilon_{ms}^{LJ}/\varepsilon_{mf}^{LJ}$ is close to one. However, as the monomer-solute interaction gets stronger, M_{ps} saturates, and subsequently decays with increasing ε_{ms}^{LJ}.

The observed decrease of M_{ps} for large values of ε_{ms}^{LJ} suggests that when solute particles bind strongly to the polymer, they become effectively immobilised and hence cannot contribute to the diffusio-osmotic flow through and around the polymer. This argument would suggest that the diffusiophoretic velocity vanishes as ε_{ms}^{LJ} becomes much larger than

the thermal energy. However, this does not seem to be the case: rather M_{ps} seems to level off at a small but finite value. This suggests that not all fluid particles involved in the phoretic transport are tightly bound to the polymer. One obvious explanation could be that the LJ potential we use is sufficiently long-ranged to interact with solute particles that are in the second-neighbour shell around the monomeric units of the polymer. To test whether this is the case, we repeated the simulations with a shorter-ranged generalised LJ potential (GLJ)[116] (see Appendix A). In the insert of Fig. 5.5 this narrower potential ($r_c = 1.6$) is shown compared with the standard truncated and shifted LJ potential with $r_c = 2.5$. In our simulations, we only used the GLJ potential for monomer-solute interactions. For all other interactions, we still used the standard LJ potential.

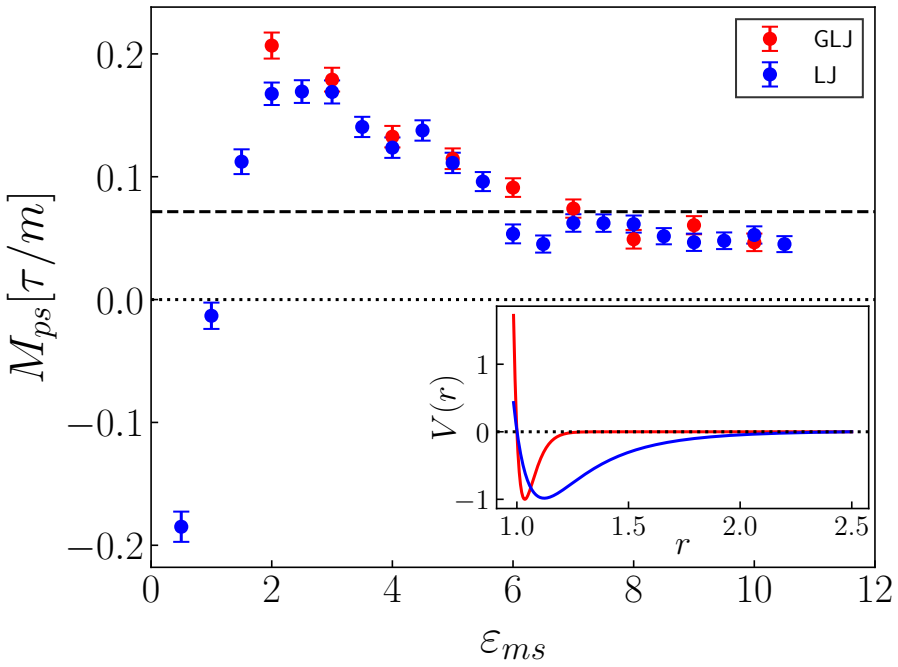

Fig. 5.5 Mobilities for different LJ interaction energies (ε_{ms}) using LJ and GLJ. The dashed line represents the theoretical estimation for $\varepsilon^{LJ} = 8.0$ (See Fig. 5.6a) using Eq. (5.5) and Kirkwood's estimation for the hydrodynamic radius $a = R_H^K$. All the simulations were performed keeping the thermodynamic conditions in the bulk constant (T,P, c_s^B). The insert the LJ potential for $r_c = 2.5$, $\varepsilon^{LJ} = 1$ is in blue and $\sigma^{LJ} = 1$ and a GLJ potential in red, showing the narrow range of the monomer-solvent interaction.

Fig. 5.5 shows a comparison of the results obtained with the LJ and the GLJ potentials. Even with the short-ranged monomer-solute interaction for which next-nearest neighbour interactions are excluded, M_{ps} still does not decay to zero at large ε_{ms}^{LJ}. This limiting behaviour suggests that the phoretic force is not just probing the excess of solute particles that are

directly interacting with the polymer, but also the density modulation of solutes (and solvent) that is due to the longer-ranged structuring of the mixture around the polymer coil. In Fig. 5.6, we show an extreme case ($\varepsilon_{ms}^{LJ} = 8.0$) where the polymer has collapsed (see Appendix D.3) and particles within a hydrodynamic radius R_H from the centre of mass do not contribute to phoresis as they are tightly bound. In contrast, particles in the structured liquid layer further away from the centre of the polymer ($r > R_H$) are mobile and can therefore contribute to the diffusio-osmotic flow

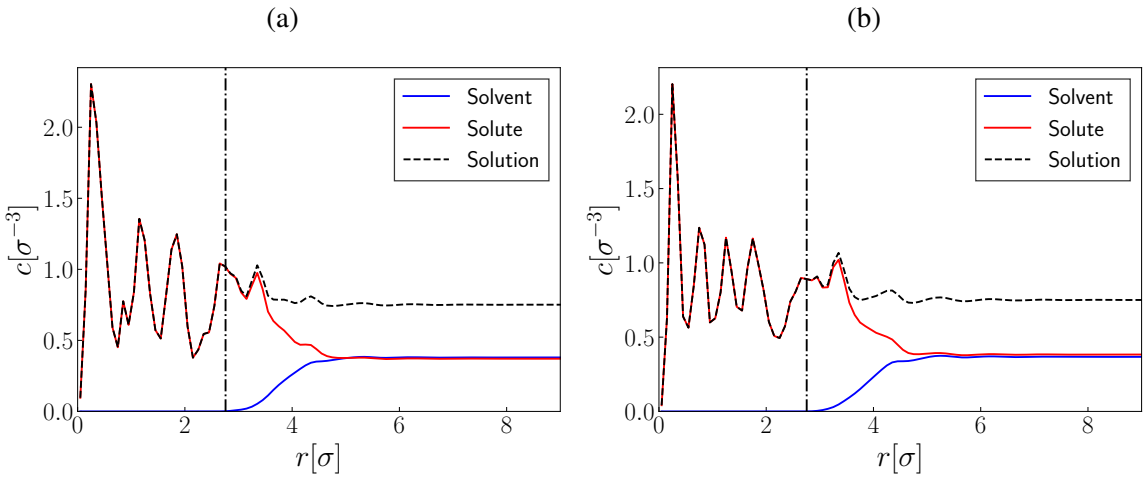

Fig. 5.6 Distribution of solutes, solvents and the total solution measured from the centre of mass of the polymer for (a) LJ, (b) GLJ. The vertical line represents the hydrodynamic radius R_H of the polymer, in both cases, $\varepsilon_{ms} = 8.0$. Mobile particles in the heterogeneous region outside the collapsed polymer coil contribute to the diffusio-osmotic flow in a similar way for both ranges of interaction.

5.2.5 Scaling of the phoretic mobility with the length of the polymer

For colloidal particles with a radius much larger than the range of the colloid solute interaction, the diffusiophoretic mobility is independent of the colloidal radius [15]. Often the diffusion of a polymer in a fluid is described as that of a colloid with an equivalent "hydrodynamic radius" R_H, one might assume that the diffusiophoretic mobility of a sufficiently large polymer is also size-independent. To our knowledge, this size independence has not been tested in simulations. However, experiments by Rauch and Köhler [117] showed that thermophoretic mobility of polymers varies with the molecular weight M_w for short polymers (fewer than 10 monomers), but very little for longer polymers (10-100 monomers). In the case of

diffusiophoresis of polymers in a salt-water solution, Mcafee & Annunziata [118] found that the diffusiophoretic mobility increases with the size of the polymer[1].

To our knowledge, there are no theoretical predictions for the diffusiophoretic mobility of polymers. Therefore, as a first approximation, we choose to use a colloidal particle model to estimate the velocity. The strong assumption that the polymer coil behaves as a hard-sphere has been used since Kirkwood [119]. Later we discuss the consequences of such approximation.

As discussed in the previous chapter (see Sec. 4.2), Anderson [15] derived an expression for the diffusiophoretic mobility of colloids in the case where the interfacial layer thickness L is smaller, but not much smaller than the radius a of the colloid. Introducing the small parameter $\lambda \equiv L/a$, Anderson derived the following asymptotic expression for the diffusiophoretic velocity v of a colloidal particle:

$$v = v_0 \left[1 - \frac{(K+H)}{L}\lambda + \mathscr{O}(\lambda^2) \right]. \tag{5.5}$$

It is worth mentioning that the corrections terms in Eq. (5.5) account for the effect of the curvature of the particle. All the above equations apply to the case where there is no hydrodynamic slip on the surface of the colloid. However, if solute particles are strongly adsorbed to the colloid, they become immobile. As a result, the surface of no-slip, and hence the effective colloidal radius, increases. Eq. (5.5) was derived assuming no-slip boundary conditions to solve the Navier-Stokes equation. Ajdari and Bocquet [68] showed that a correction due to the hydrodynamic slip captures the transport enhancement at interfaces. Including the amplification factor due to the surface slip, for moderate adsorption or depletion of solutes, the corrected diffusiophoretic velocity v' reduces to:

$$v' = v\left(1 + \frac{b}{L}\right). \tag{5.6}$$

where b is the hydrodynamic slip length.

To investigate the dependence of the phoretic motion on the number of monomers of the chain N_m, simulations were performed for a range of N_m from 5 to 60. As our polymers are fully flexible (but self-avoiding), a chain of 60 beads corresponds to a medium-sized polymer. The simulation box was scaled accordingly with the Flory exponent for a polymer in a good solvent $\nu \approx 0.6$, thus ensuring that the chain could not overlap with its periodic images. All the NEMD simulations were carried out for 10^8 time steps.

[1] Shin *et al.* [55] showed that in a dead-end channel larger colloidal particles travel farther than smaller particles

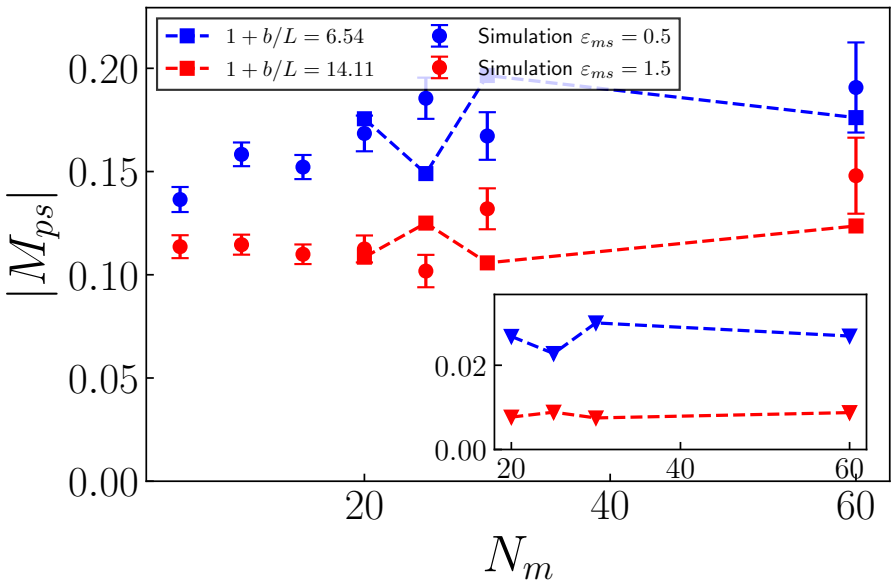

Fig. 5.7 Diffusiophoretic mobility M_{ps} of a polymer *vs* the number of monomers in the polymer N_m. The results $\varepsilon_{ms}^{LJ} = 1.5$ are shown in red and in blue for $\varepsilon_{ms}^{LJ} = 0.5$. The simulations results are represented as dots and the theoretical predictions (Eq. (5.5), including the amplification due to the hydrodynamic slip), are shown as squares. The insert shows the theoretical predictions without slip correction. In the theoretical calculations $a = R_H$, where R_H is the hydrodynamic radius estimated, for the specific interaction ε_{ms} and thermodynamic conditions, using Stokes-Einstein relation (Eq. (4.22))

In Fig. 5.7, the simulation results are shown together with theoretical predictions replacing the polymer by an equivalent hard sphere with a radius $a = R_H$ given by Stokes-Einstein relation in Eq. (4.22) (comparison with the Kirkwood approximation for R_H [119] are shown in Appendix D.4), where η denotes the viscosity of the solution in the bulk, which was computed independently, using the Green-Kubo expression relating η to the stress autocorrelation function, in an equilibrium simulation of the bulk fluid. The diffusion coefficient D was also computed from equilibrium simulations considering the different interactions ε_{ms}. For the details on the calculations for η and D see Appendix B.

Fig. 5.7 shows that the diffusiophoretic mobility of the polymer increases with N_m. The large quantitative differences between the simulations and the theoretical approximations for a colloid with the same hydrodynamic radius are to be expected: First of all, the assumption that the polymer coil behaves as a hard-sphere with $a = R_H$ is rather drastic. To be more precise, this approximation (which was also used by Kirkwood [119]) assumes that the liquid molecules within the coil region move together, such that the whole assembly moves as a rigid sphere (see e.g. [120]). This might be a good approximation for the diffusion of long polymer coils, but in the case of phoresis, it is unrealistic to assume that no solute/solvent

can be transported through the polymer at distances less than R_H. The second (but related) questionable approximation is that R_H defines the surface of the equivalent colloid in the integrals in the parameters of Eq. (5.5). As a consequence, the contribution of any excess solute at a distance less than R_H from the polymer centre is ignored. As is clear from Fig. 5.6 this assumption is incorrect and likely to underestimate the real diffusiophoretic flow, since Fig. 5.8b shows that there can be considerable solute advection for $r < R_H$.

Our simulations suggest that better theoretical models for polymer diffusiophoresis are required. In Fig. 5.8 we show the velocity field for a polymer with $N_m = 30$ for two cases: when it is subjected to a body force Fig. 5.8a and under the influence of diffusiophoresis Fig. 5.8b. As is obvious from the figure, in both cases there is fluid motion within the polymer at distances less than R_H from its centre of mass. However, there is an important difference between the flows inside the polymer for the pressure-driven and phoretically driven flows: strong hydrodynamic screening is found in the case of a pressure gradient while for diffusiophoresis, screening seems to be effectively absent. Notice that the density profile is somewhat asymmetric due to the advection produced by the pressure-driven flow. Shin *et al.* reported evidence for a similar absence of hydrodynamic screening in a dense plug of colloidal particles moving under the influence of diffusiophoresis [40]. Shin *et al.* argued that the difference in screening in the case of phoretic flow, as opposed to the flow due to body forces or pressure gradients, could be attributed to the difference in the range of the hydrodynamic flow fields. The flow decays as (($\sim 1/r$) for body-forces and pressure-driven flow. Meanwhile, phoretically induced flows decay as($\sim 1/r^3$) [16, 92, 105]. A signature of the rapid decay was noticed in a finite-size analysis. We observed that the diffusiophoretic velocity did not change with the increase of the box size (see Appendix D.2). Moreover, the fast decay in the phoretically induced flow implies that there is no effective hydrodynamic interaction between distant monomers in large polymers. This might explain the small variation in the mobilities for large N_s in Fig. 5.7.

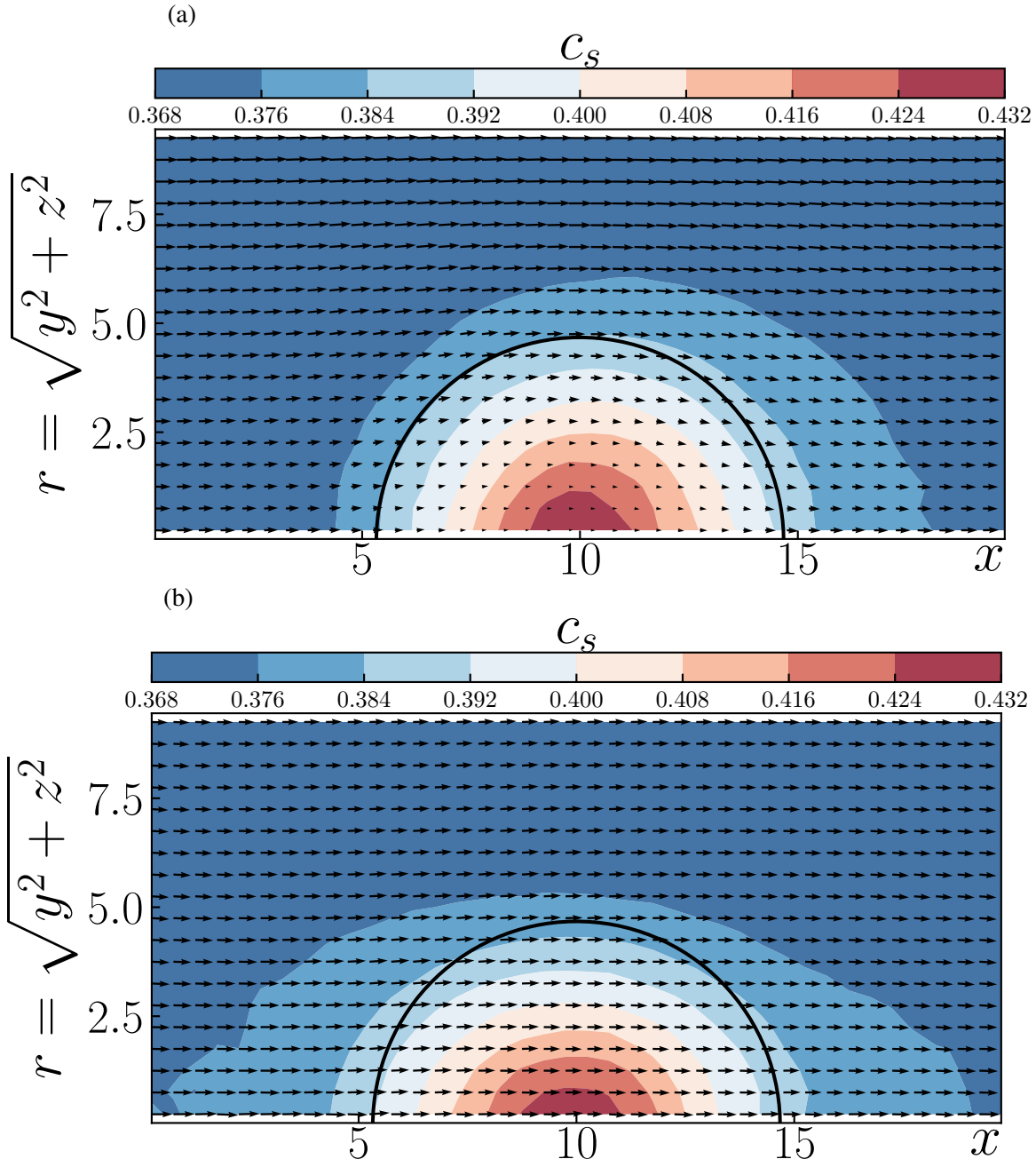

Fig. 5.8 Flow around a polymer coil. (a) when a body force is applied, hydrodynamic screening perturbs the streamlines at the vicinity of the polymer. (b) for diffusiophoresis the hydrodynamic screening seems not to perturb the flow profile near the polymer. The velocity field is measured in a coordinate system moving with the centre of mass of the polymer. The black semicircle shows the equivalent colloid and the contours show the solute concentration, for both cases $\varepsilon_{ms} = 1.5$. The measurements were taken inside a cylinder with an axis along the direction of the applied force, with the axis passing through the centre of mass of the polymer. The contours show the solute concentration c_s.

5.3 Conclusions

We have performed molecular dynamics simulation on the diffusiophoresis of polymers in a fluid mixture under the influence of a concentration gradient of solutes. We used the FD-NEMD method, where the effect of an explicit concentration gradient in the system by imposing equivalent microscopic forces on the solute, solvent and monomers. This approach allows us to use periodic boundary conditions and facilitates a systematic investigation of diffusiophoresis. We find, as in our previous case study, a non-monotonic relation between diffusiophoretic mobility and monomer-solute interaction. We rationalise that this behaviour is due to two main reasons: first, as in the colloidal case, solutes that are tightly bound do not contribute to phoresis. Second, the conformation of the polymer changes as the interaction with solutes varies. Furthermore, we have demonstrated that the diffusiophoretic mobility of a (short) polymer cannot be explained in terms of a model that assumes it as a solid spherical particle. Finally, we found an ineffective hydrodynamic flow screening inside a polymer moving due to diffusiophoresis. This result differs from what is observed in the case of a polymer moving through a fluid under the influence of an external force.

Chapter 6

General Conclusion and Outlook

"Physics is like sex: sure, it may give some practical results, but that's not why we do it."

Richard P. Feynman

In this thesis, we investigated diffusio-osmosis as well as diffusiophoresis using a microscopic approach. We first briefly presented the available theoretical and computational methods to study these phenomena employing both EMD and NEMD. Our first case study was the diffusio-osmotic flow in a simple planar geometry, where we propose an alternative route to derive a theoretical estimate for the flow velocity. Our expression is based on the LTE approach. We include the contributions to diffusio-osmosis from all the species in a multi-component solution. In particular, we take into account the solvent particles. This discrete treatment of the solvent is a crucial difference with respect to previous works based on continuum frameworks. Furthermore, we show that we can recover Derjaguin-Anderson's results for the limiting case when there is an ideal-dilute solution in the bulk.

We presented a systematic derivation of the entropy production for transport driven by chemical potential gradients using non-equilibrium thermodynamics. This starting point was crucial to construct a consistent set of thermodynamic forces and fluxes. As simple as this seems, the lack of this initial step could have caused erroneous interpretations in previous works. We used a representation with pressure gradients and chemical potential gradients for the solutes as thermodynamic forces. Once we defined the transport matrix, we employed linear response theory to find the Green-Kubo expressions for the diffusio-osmotic transport coefficients, demonstrating that Onsager's reciprocity was fulfilled. We then established the connection between micro- and thermodynamic forces. Afterwards, we used the microscopic forces to perform FD-NEMD on a benchmark system. Referring back to the simulation

results, we quantified the theoretical estimations based on the different species in the solution. For future research projects, it would be interesting to extend the simulations to systems with more than two components in order to test the limitations of our theoretical model and perhaps exploring some alternatives to the assumption of constant viscosity.

After building a solid theoretical background and validating our numerical simulations, we extended the application of FD-NEMD to study non-planar geometries such as colloids and polymers. In the case of colloids, we examined spherical particles under the influence of solutes in a binary solution. We performed simulations using two non-equilibrium techniques. We first imposed the explicit thermodynamic force driving the phoretic motion. Alternatively, we used the microscopic representation of the chemical potential gradient. Our findings show that the FD-NEMD method is more advantageous than BD-NEMD, mainly because it allows studying phoretic transport minimising the effects of advection. Our results proved a non-monotonic dependence of the velocity with the interaction strength between the colloid and the solutes. This behaviour shed light on the way that the mobility of solution in the nearest layers to the colloidal particle takes place. For moderate interactions, the excess of solutes increases the fluid flow around the colloidal particles. Conversely, when the solutes interact so strongly that they form an immobile layer around the colloid, there is a decay in their mobility and therefore their contribution to phoretic motion.

As a final case study, we explored the diffusiophoresis of a short polymer coil. The results showed the same monotonic relation between mobility and monomer-solute interaction. A further investigation, employing a generalised LJ potential, revealed that there is remnant transport at high interactions caused by the moving liquid layers beyond the range of direct interaction with the colloid. Moreover, we found that the theoretical predictions formulated for colloidal particles are not able to describe polymer diffusiophoresis. The lack of a defined surface in the case of the polymers makes it problematic to establish a reference point for the theoretical calculation. To compensate for the limitations in the theoretical estimates, we added a slip amplification factor in order to account for the missing elements in the derivation. Finally, we observed that there is a penetration of hydrodynamic flow fields and solutes into the polymer coil, in the case of phoretic motion. These flow patterns are different from what is observed for a polymer moving under the influence of a body force or a pressure-driven flow. The reason for the difference is that diffusiophoresis originates in the diffuse layer and the flow perturbations are restricted to this same region. Meanwhile, pressure-driven flows are characterised by a slow decay of the hydrodynamic perturbation.

In future work, we plan to use the experience from this thesis to simulate more challenging systems. In particular, we would like to focus on a porous medium constituted by random obstacles. In such a system, there is no clear separation between the diffuse layer and bulk.

This lack of differentiation poses a practical problem, as the definition of the microscopic forces in our simulations relied on the mechanical balance in the bulk. Furthermore, a formulation of the entropy production where the pressure gradient appears as one of the thermodynamic forces will not be convenient. For such an inhomogeneous system, the connection between the pressure gradient and an equivalent mechanical constraint on the particles using FD-NEMD is not possible. Lastly, non of the theories described in this work would allow studying this porous system. Perhaps an approach inspired by macro-transport processes might be useful.

Appendix A

Generalised Lennard-Jones (GLJ) potential

A.1 The need for a new short range potential

The Lennard-Jones 12-6 potential was proposed to describe noble gases like argon [121]. It Includes a dispersive London force that decays as $1/r^{-6}$ for long distances, which made it convenient for analytical calculations. The potential became widely used for molecular simulations due to the success in predicting experimental argon data [122, 123]. Later, it turned out that a fortuitous cancellation of error was the cause of the a priori accurate results [124]. For numerical purposes, the infinite range of the LJ potential needs to be truncated for MC simulations and additionally shifted for MD to avoid discontinuities in the force. There are several ways of truncating the potential, and the choices of cutoff radius are "infinite". This situation brings confusion, and special care is required to reproduce and compare results from different sources.

Wang *et al.* [116][1] proposed a class of LJ-like potentials with a finite range by construction, vanishing quadratically at the cutoff distance. Thus, avoiding the ambiguities mentioned before. The general form of the potential is

$$\phi(r) = \varepsilon\alpha\left(\left[\frac{\sigma}{r}\right]^{2\mu} - 1\right)\left(\left[\frac{r_c}{r}\right]^{2\mu} - 1\right)^{2\nu}, \tag{A.1}$$

with

$$\alpha = 2\nu\left(\frac{r_c}{\sigma}\right)^{2\mu}\left[\frac{1+2\nu}{2\nu\left[(r_c/\sigma)^{2\mu}-1\right]}\right]^{2\nu+1} \tag{A.2}$$

[1] This potential will be available in LAMMPS for the next stable release.

$$r_{min} = r_c \left[\frac{1+2\nu}{1+2\nu(r_c/\sigma)^{2\nu}} \right]^{1/2\nu} \tag{A.3}$$

The simplest case is $\nu = \mu = 1$, and little is gained with higher values of μ and ν. Increasing ν make higher derivatives of the potential continuous at r_c at a higher computational expense. The advantage and simplicity of this potential come as r_c is defined unambiguously.

A.2 Thermodynamic and transport properties

The wide use of the Lennard-Jones potential might be because many properties of this model have been studied extensively. Therefore, we computed the thermodynamic quantities for the different phases of GLJ potential and used a multivariate polynomial fit on our numerical data. To describe the procedure, here we focus on the liquid phase, but an equivalent development for the solid phase is straightforward [116]. Our starting point is the excess Helmholtz free energy $A_{\text{exc}}(N,V,T)$, or more precisely $\beta A_{\text{exc}}/V = \beta\rho a_{\text{exc}}$, where $\beta \equiv 1/k_B T$, and $a_{\text{exc}} \equiv A_{\text{exc}}/N$.

We assume that $\beta\rho a_{exc}$ can be expanded in a two variables polynomial, namely the density ρ and β,

$$\beta\rho a^L_{\text{exc}} = \sum_{n=n_{min}}^{n_{max}} \sum_{m=m_{min}}^{m_{max}} a^L_{n,m} \rho^n \beta^m \,. \tag{A.4}$$

we know from thermodynamics that

$$\rho e_{\text{exc}} = \left(\frac{\partial \beta\rho a_{exc}}{\partial \beta} \right)_\rho \,. \tag{A.5}$$

hence,

$$\rho e^L_{\text{exc}} = \sum_{n=n_{min}}^{n_{max}} \sum_{m=m_{min}}^{m_{max}} a^L_{n,m} m \rho^n \beta^{m-1} \tag{A.6}$$

Using again Eq. (A.4) and the following thermodynamic relation,

$$\beta P_{\text{exc}} = -\left(\beta\rho a_{exc} - \rho \left(\frac{\partial \beta\rho a_{exc}}{\partial \rho} \right)_T \right) \,, \tag{A.7}$$

we obtain the polynomial expansion for the excess pressure P^L_{exc}

$$\beta P^L_{\text{exc}}(\rho,\beta) = \sum_{n=n_{min}}^{n_{max}} \sum_{m=m_{min}}^{m_{max}} (n-1) a^L_{n,m} \rho^n \beta^m \,. \tag{A.8}$$

From Eqs. (A.4), (A.6) and (A.8) we notice that we can describe the relevant thermodynamic quantities using a *single* set of fitting parameters $a^L_{n,m}$ for the liquid phase. Therefore, to find $a^L_{n,m}$ we perform a minimisation of χ^2 given by

$$\chi^2 = \sum_{\alpha}\sum_{i} \frac{\left(\sum_{n',m'} c^{\alpha}_{n',m'} \rho_i^{n'} \beta_i^{m'} - X_\alpha(\rho_i,\beta_i)\right)^2}{\sigma^2_\alpha(\rho_i,\beta_i)}\,, \tag{A.9}$$

where the index α is such that X_α represents the thermodynamic quantities βP^L_{exc} or ρe^L_{exc} with error estimates given by $\sigma_\alpha(\rho_i,\beta_i)$. Comparing Eq. (A.9) with (A.6) and (A.8) we define m', n', $c^{\alpha}_{n',m'}$ and $\sigma_\alpha(\rho_i,\beta_i)$.

In Fig. A.1 we show the simulation results together with the estimations using the fitting. We used $n_{min} = 2$ (because at low densities, the excess pressure scales as ρ^2), $n_{max} = 8$, $m_{min} = -3$ and $m_{max} = 2$.

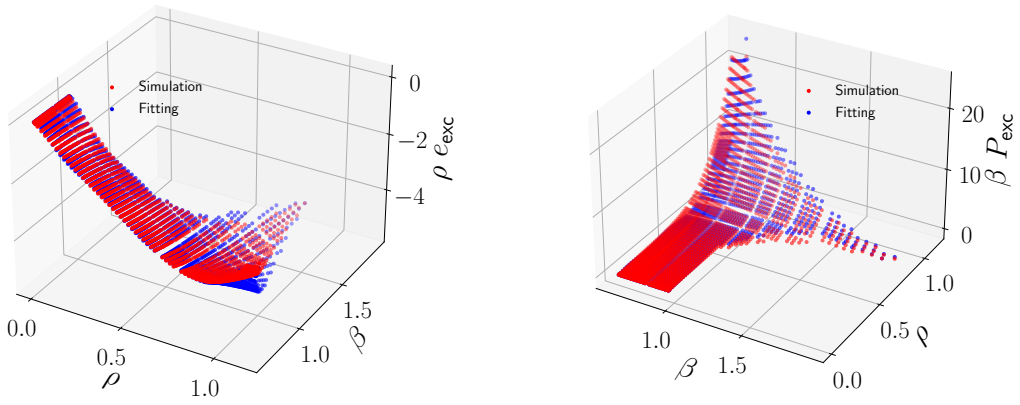

Fig. A.1 Simulation and fitting results for the liquid phase with $r_c = 2.0$. (a) shows the energy and (b) the excess pressure, both as a function of the density *rho* and the inverse temperature β.

Once we have estimated the fitting coefficients, we can also predict the excess chemical potential using,

$$\beta\mu_{exc} = \left(\frac{\partial \beta\rho a_{exc}}{\partial \rho}\right)_T\,. \tag{A.10}$$

Therfore, the same set of fitting coefficients $a^L_{n,m}$ allows predicting the excess chemical potential as follows

$$\beta\mu_{exc} = \sum_{n=n_{min}}^{n_{max}} \sum_{m=m_{min}}^{m_{max}} a^L_{n,m} n \rho^{n-1} \beta^m\,. \tag{A.11}$$

Finally, we used Green-Kubo expressions (see Sec. 3.2.3) to compute the diffusivity, viscosity and thermal conductivity. We performed the same multivariate fitting strategy for each one of the transport coefficients. For instance, the viscosity:

$$\eta = \sum_{n=n_{min}}^{n_{max}} \sum_{m=m_{min}}^{m_{max}} a_{n,m}^{(\eta)} \rho^n \beta^m \,. \tag{A.12}$$

In Fig. A.2 we show the simulation results together with the estimations using the fitting with $n_{min} = 0$, $n_{max} = 6$, $m_{min} = 0$ and $m_{max} = 6$.

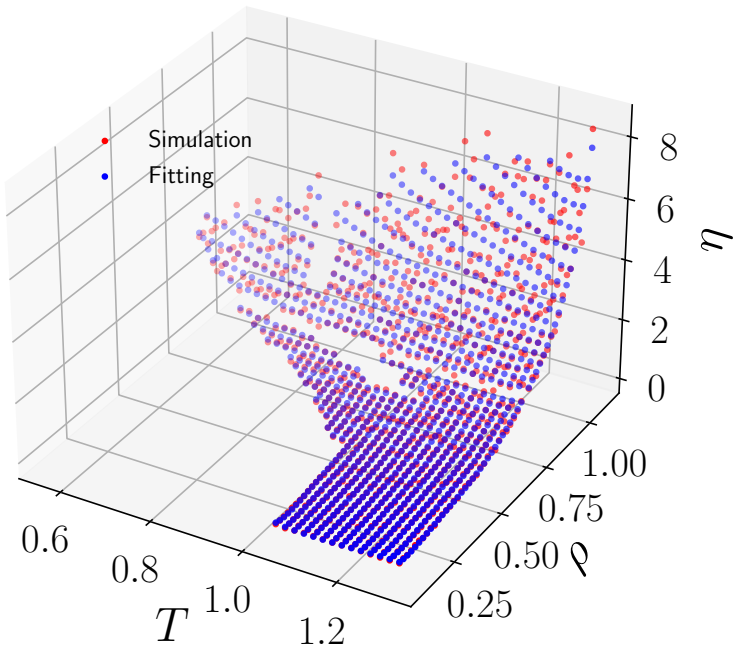

Fig. A.2 Simulation and fitting results for the viscosity of a liquid phase with particles interacting with parameters $\nu = 1$, $\mu = 1$ and $r_c = 2.0$.

Appendix B

Green-Kubo formalism

It can be shown that the response of a system to a small perturbation is described in terms of time correlations of microscopic observables in equilibrium. Therefore, only the knowledge of the effect of the thermal fluctuations is enough to describe the response to any small perturbation. This approach is known as the linear response theory. In this section, we discuss the standard procedure to compute transport coefficients that can be found in more detail elsewhere [56].

Suppose that the Hamiltonian of a system is described by

$$\mathscr{H} = \mathscr{H}_0 + \Delta\mathscr{H} \,, \tag{B.1}$$

where $\mathscr{H}_0$ is the Hamiltonian of the unperturbed system and $\Delta\mathscr{H}$ is the perturbation by an external field $\mathscr{F}$ weakly coupled to the system. If we have a monochromatic field, with frequency ω, the perturbation can be written as

$$\Delta\mathscr{H} = -A\mathscr{F}\exp\{-i\omega t\} \,, \tag{B.2}$$

where A is in general a function of the positions $\mathbf{p}^N$ and momenta $\mathbf{q}^N$ of the N particles in the system. The change in the observed variable B up to linear terms in $\Delta\mathscr{H}$ is given by

$$\langle \Delta B(t)\rangle = \frac{1}{k_B T}\int_0^\infty \langle B(t)\dot{A}(0)\rangle \mathscr{F}\exp\big\{-i\omega(t-t')\big\}dt' \,. \tag{B.3}$$

We can define the transport coefficients M_{ij} in the hydrodynamic limit ($\omega \to 0$) as [97]:

$$M_{BA} = \frac{1}{k_B T}\int_0^\infty \langle B(t)\dot{A}(0)\rangle \,. \tag{B.4}$$

For a system with microscopic invariance under time reversal transformations we have that $\langle B(t)\dot{A}(0)\rangle = \langle A(t)\dot{B}(0)\rangle$, thus $M_{BA} = M_{AB}$, fulfilling Onsager's reciprocal relations.

Equations as Eq. B.4 are know as Green-Kubo relations. These relations connect transport coefficients with the time correlations of the fluctuating microscopic variables in thermal equilibrium. Two examples that are relevant for the present work are the diffusivity D and the shear viscosity η.

The diffusivity or self-diffusion constant D in d dimensions can be expressed in terms of the velocity autocorrelation function,

$$D = \frac{1}{d}\int_0^\infty d\,t\ \langle \mathbf{v}(t)\cdot\mathbf{v}(0)\rangle = \int_0^\infty d\,t\ \left\langle v^i(t)v^i(0)\right\rangle\ . \tag{B.5}$$

Alternatively, the diffusivity can be expressed in terms of the mean-squared displacement (MSD) $\langle \Delta\mathbf{r}^2\rangle$ as,

$$D = \frac{1}{2d}\frac{\partial\langle\Delta\mathbf{r}^2\rangle}{\partial t}\ . \tag{B.6}$$

The Green-Kubo relation for the shear viscosity η is given by:

$$\eta = \frac{1}{Vk_BT}\int_0^\infty d\,t\ \langle\Pi^{xy}(t)\Pi^{xy}(0)\rangle\ . \tag{B.7}$$

with the xy component of the microscopic stress tensor given by the Virial expression [77]

$$\Pi^{xy} = \sum_{i=1}^{N}\left(m_i v_i^x v_i^y + \frac{1}{2}\sum_{j\neq i} x_{ij} f_y(r_{ij})\right)\ , \tag{B.8}$$

with the first term representing the kinetic contribution to the stress tensor and the second term is the potential contribution that depends on the distance between the particles x_{ij} and the force due to their interaction $f_y(r_{ij})$.

Appendix C

Measuring the viscosity

The shear viscosity η measures the momentum transfer of a fluid in a direction perpendicular to the flow. There are several approaches to compute this quantity -or any transport coefficients, using both equilibrium and non-equilibrium molecular dynamics. Meier *et al.* [125] discuss in detail the different procedures to determine η for a Lennard-Jones fluid. In this section, we illustrate two methods: one based on the Green-Kubo (GK) relations in Sec. 3.2.3 and the other on the well-know Poiseulle flow.

The first approach is purely based on equilibrium simulations and uses Eq. (B.7) to compute the viscosity. We measure the microscopic stress tensor using the virial expression in Eq. (B.8) and compute the stress autocorrelation function (SACF). As the fluid is isotropic, we improve the statistics using the average of the SACF from all the off-diagonal and diagonal terms of the stress-tensor [126]. In Fig. C.2 we compare our results with an empirical law for the viscosity [127].

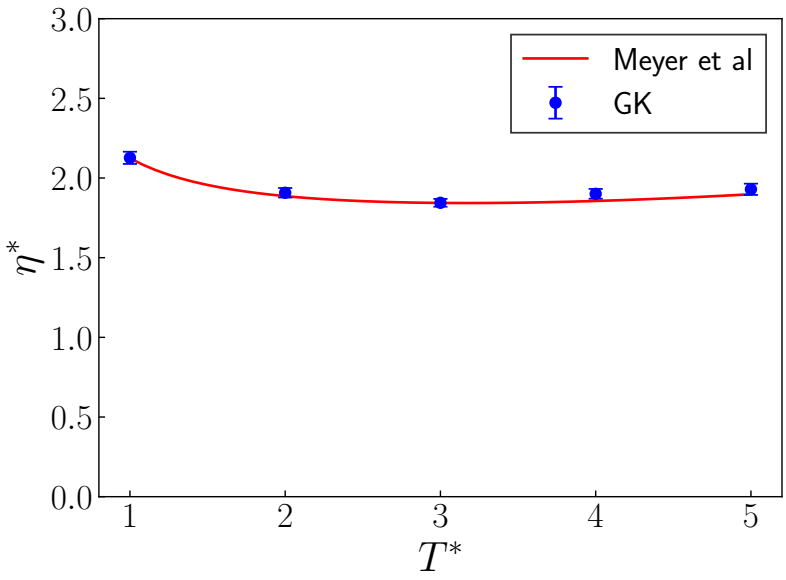

Fig. C.1 Reduced shear viscosity η^* for different reduced temperatures T^*. The points with error bars show the results for the estimations using the GK relation in Eq. (B.7). The red line is the prediction for the viscosity using an empirical law [127].

For the systems treated in the main text, we cannot use the empirical law for the viscosity by Meyer, as we use a shorter cutoff radius $r_c = 2.5\sigma$. Therefore, we need to compute explicitly the GK relation (see Eq. (B.7)) to obtain the shear viscosity. In the case of diffusio-osmosis, as we have an ideal binary solution in the bulk, we can assume a single component LJ system at $k_BT/\varepsilon = 1$, $P\sigma^3/\varepsilon = 1$. The system was thermostated and barostated for 2×10^5 time steps of $0.005t_0$. During the barostaing process, the simulation box was allowed to fluctuate in the z direction, i.e in the direction perpendicular to the walls. After that, we fixed the length of the simulation box in the z direction L_z, to the average value sampled during the barostating. We ran NVT simulations sampling all the independent components of the stress-tensor for 10^6 steps and computed the SACF (see Fig. C.1). We performed 10 independent runs. For each one, we evaluated the GK relation for different upper integration times t^*. In Fig. C.3 we show the evolution for one of the runs. Averaging the results from the independent runs, we find that the shear viscosity is $\eta^* = 1.57(2)$.

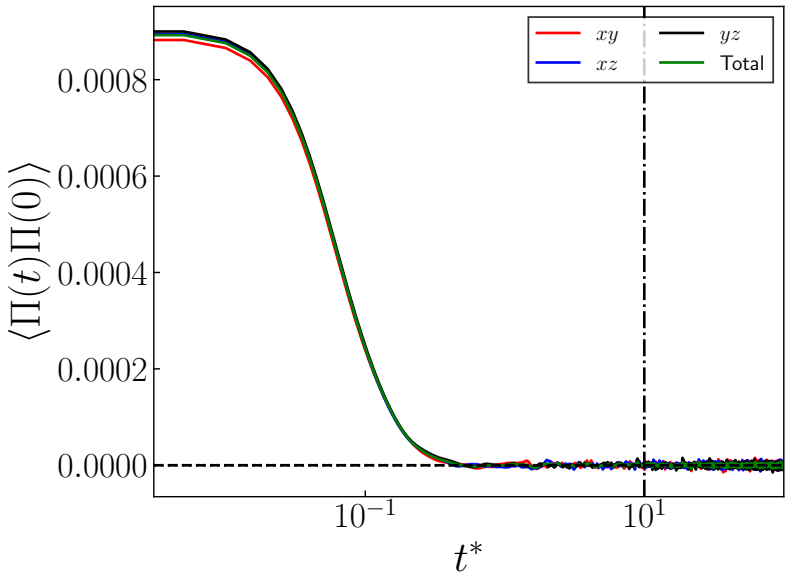

Fig. C.2 Stress autocorrelation function for the three out of diagonal terms *xy*, *xz*, *yz* and the average ("Total"). Results are plotted in a log scale to emphasise the fast decay. The vertical line indicates the upper limit for the integral shown in Eq. (B.7).

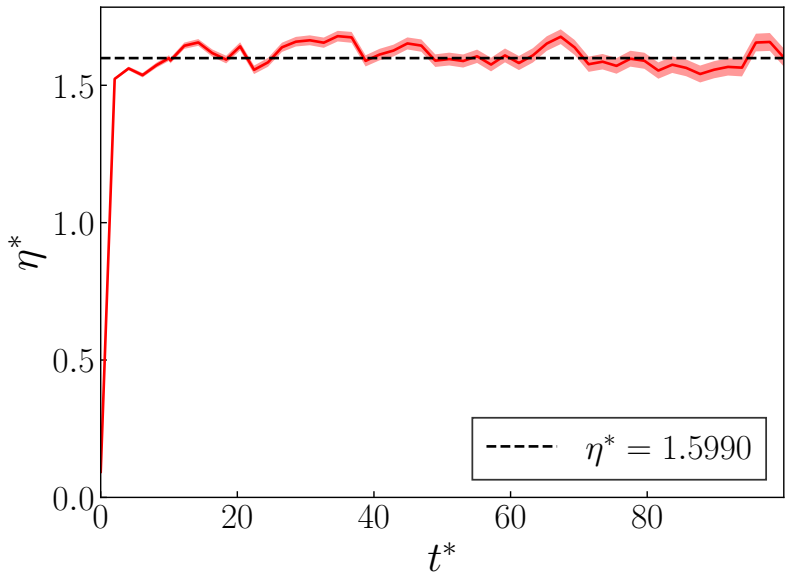

Fig. C.3 The evolution of η^* for different upper integration limits t^*. We show the results for one of the independent runs. The value of η^* at $t^* = 10$ is used as reference.

The second approach to compute the shear viscosity from NEMD was proposed by Todd *et al.* [94]. It consists of a planar Poiseuille flow simulated by applying a gravitational-like

force on all the particles in the fluid. The equation describing the hydrodynamics of the system is given by:

$$\rho(\mathbf{r},t)\frac{\mathrm{d}\mathbf{v}(\mathbf{r},t)}{\mathrm{d}t} = -\boldsymbol{\nabla}\cdot\Pi + \rho(\mathbf{r},t)\mathbf{F}^{e}\,. \tag{C.1}$$

Assuming a steady flow, Newtonian viscosity and homogeneous fluid density ρ, we find that,

$$v_x(z) = \frac{\bar{\rho}F^{e}}{2\eta}\left(z^2 - \frac{L_z^2}{4}\right), \tag{C.2}$$

where $\bar{\rho}$ is the average density in the bulk region, as defined in the main text.

Notice that the assumption of a homogeneous density in a confined liquid between solid walls is not valid at the interface (see discussion in Sec. 3.2.3). However, since we are interested in the shear viscosity in the bulk, we can assume that the density is constant. In Fig. C.4 we show the flow profiles for various F^{e}. We fitted the velocity profiles far from the walls by using Eq. (C.2). The average value for the viscosity is $\eta = 1.53(3)$. This result is in agreement with the estimates obtained using GK.

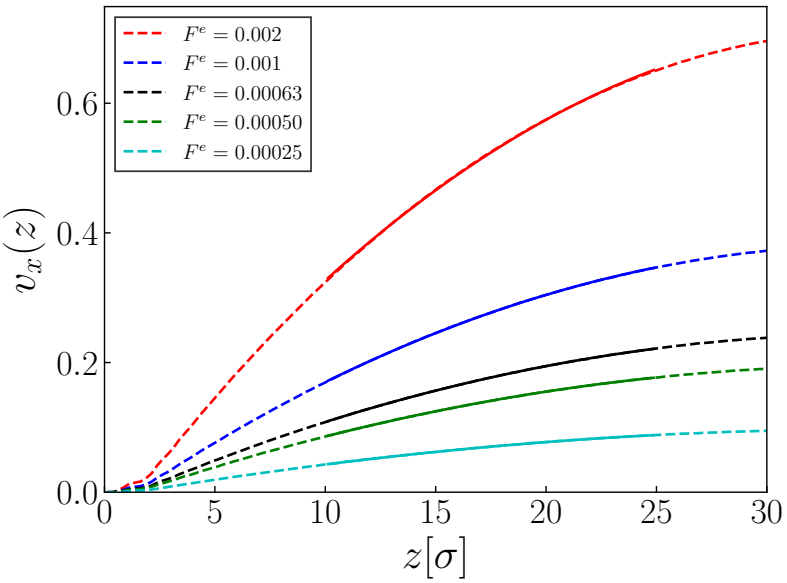

Fig. C.4 Flow profiles for different applied forces F_e. The fitting using Eq. C.2 is performed only in the bulk region where $z \in [10, 25]$

Appendix D

Additional results for polymer diffusiophoresis

The results in this section were performed using the same system as described in the polymer diffusiophoresis chapter with $c_s^B \approx 0.15$.

D.1 Fixed or free polymer

In the main text, we employed a dynamical definition of the bulk and the polymer domain. The definition was such that the z-coordinate of the centre of mass of the polymer coincides with the middle of the box. This procedure ensures that the *bulk* region remains unperturbed by the polymer. Another way of performing the FD-NEMD simulations on diffusiophoresis is to constrain the polymer to the centre of the simulation box. Thus, no redefinition of the coordinates is required. We achieved this in two different ways: first, we assign an *infinite* mass to a central monomer; second, we impose a zero-force constraint on the same monomer. In the latter, the monomer still exerts a force on all the other particles. In Fig. D.1, we show the results of these two methods compared with those obtained with the procedure described in the main text.

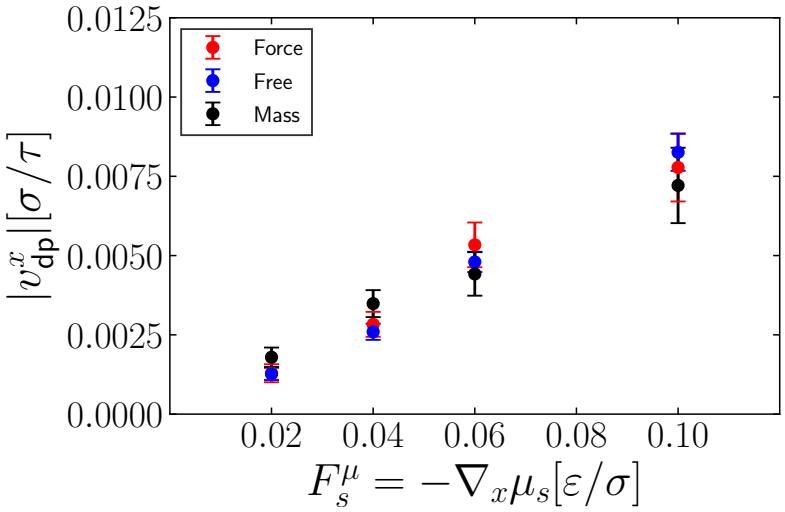

Fig. D.1 Diffusiophoretic velocity v_{dp} for $\varepsilon_{ms} = 1.5$ using three different methods: “Free" described in the main text, “Mass" assigning an infinite mass to one of the central monomers and “Force" constraining the central monomer to be force-free. In the first case, we measured the velocity of the centre-of-mass of the polymer. In the other two approaches, we measured the flow in the bulk.

D.2 Finite-size effects

Our original simulation box consisted of a cubic region of side L_c with additional bulk regions of cross-section $L_c \times L_c$, and a total height of $L_z = 10$. To analyse the finite-size effect on our simulations, we changed L and measured v_{dp}^{x} for the methods described in Sec. D.1. The results in Fig. D.2 show no clear size effect. These results differ from pressure-driven flow estimations by Hasimoto [128] (later improved by Sangani *et al.* [129]), who found that the drag force for a periodic array of spheres increases with the volume fraction due to the hydrodynamic interaction between the different elements in the array. The lack of a clear size effect on the v_{dp}^{x} suggests that, in the case of diffusiophoresis, the fast decay in the perturbation of the flow restricted to the diffuse layer has no effect far from the polymer. Moreover, Khair [105] predicts that for very low *Pe*, two identical spheres undergoing diffusiophoresis translate with the same velocity as isolated spheres.

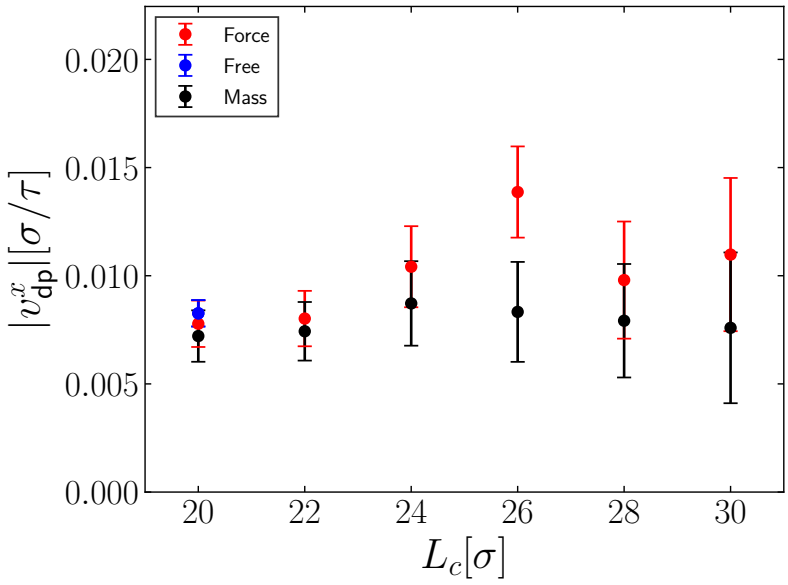

Fig. D.2 Diffusiophoretic velocity v_{dp} for different box side L_c, $\varepsilon_{ms} = 1.5$ and a force on the solutes $F_s^{\mu} = 0.15$. We report 3 different methods: “Free" described in the main text, “Mass" assigning an infinite mass to one of the central monomers and “Force" constraining the central monomer to be force-free.

D.3 Conformational changes

In Fig. D.3, we show the evolution of the different pair correlation functions for all the species. The results show that as the interaction between the monomers and the solutes ε_{ms} increases, the monomers tend to be surrounded only by solutes. The polymer undergoes conformational changes, going from an extended polymer for small $|\varepsilon_{ms}|$, typical for a polymer in a good solvent, to a collapsed globular shape when $|\varepsilon_{ms}|$ increases. The evolution of the radius of gyration R_g in Fig. D.4 corroborates the observations.

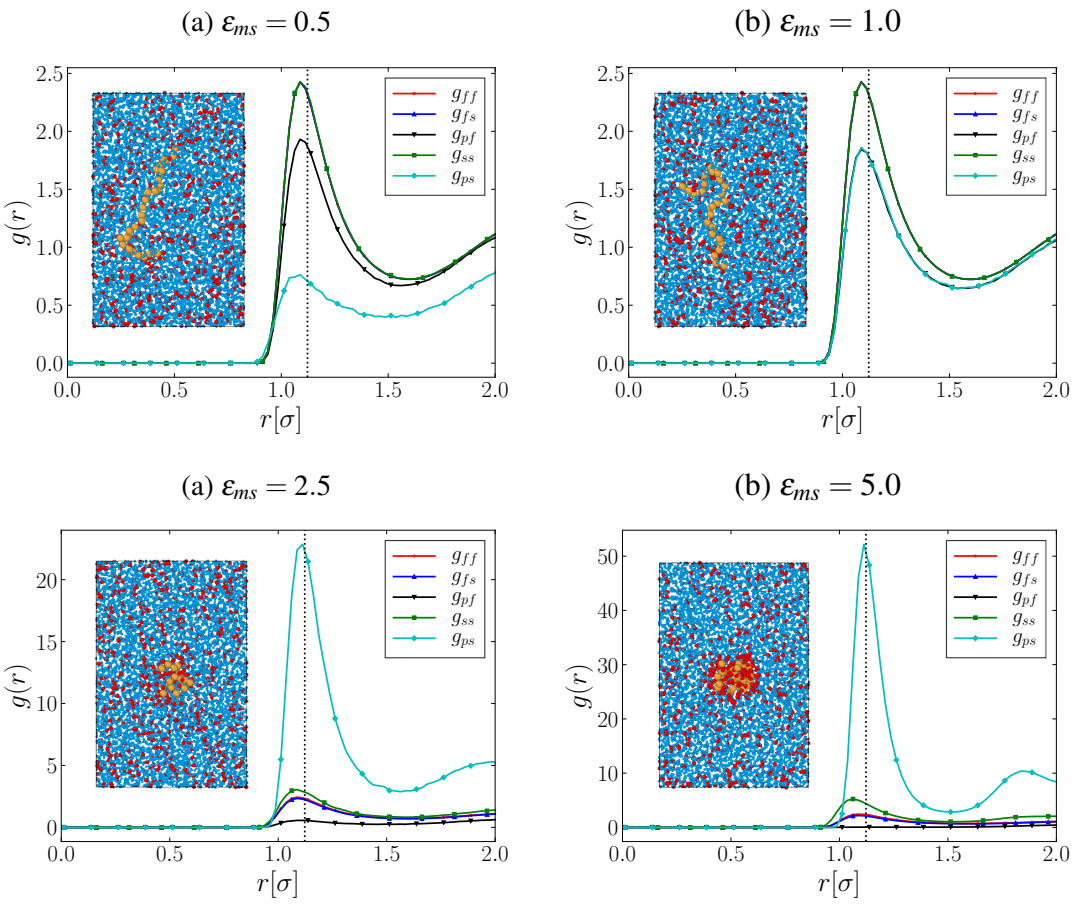

Fig. D.3 Pair-correlation distributions g_{ij} with the indexes i, j running over p, s, f, the monomers, solutes and solvent respectively. The small inserts show simulation snapshots with typical polymer configurations.

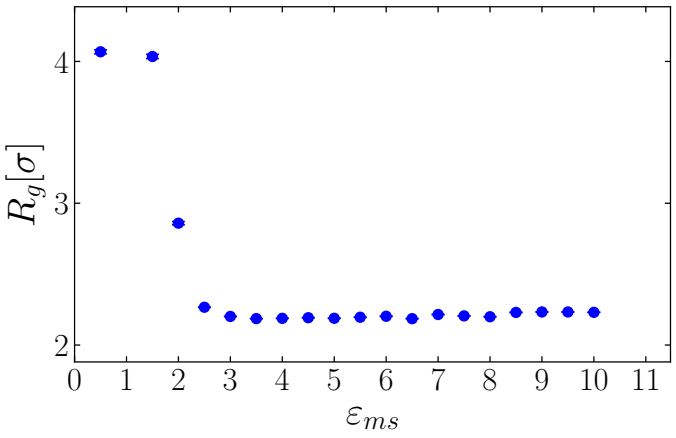

Fig. D.4 Radius of gyration R_g for a short polymer ($N_m = 30$) at different ε_{ms}.

D.4 Mobility vs N (Kirkwood approximation)

In Fig. D.5, the simulation results are shown together with theoretical predictions replacing the polymer by an equivalent hard sphere with a radius $a = R_H$. The hydrodynamic radius R_H is given by Kirkwood's approximation [119].

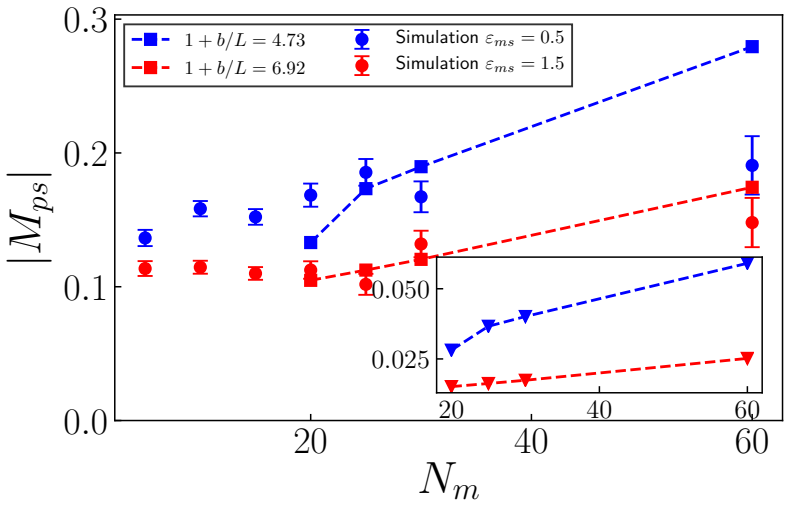

Fig. D.5 Diffusiophoretic mobility M_{ps} of a polymer vs the number of monomers in the polymer N_m. The results are shown in red for $\varepsilon_{ms}^{LJ} = 1.5$ and blue for $\varepsilon_{ms}^{LJ} = 0.5$. The simulations results are presented as dots and the theoretical predictions using Anderson's prediction [15], including the correction due to the hydrodynamic slip [68], are shown as squares. The insert shows the theoretical predictions without the correction for the hydrodynamic slip.

References

[1] B. Abécassis, C. Cottin-Bizonne, C. Ybert, A. Ajdari, and L. Bocquet, "Boosting migration of large particles by solute contrasts," *Nature Materials*, vol. 7, pp. 785–789, 2008.

[2] J. Tyndall, "On Dust and Disease," *The british medical Journal*, vol. 1, no. 547, p. 661–662, 1871.

[3] J. C. Maxwell, "On Stresses in Rarified Gases Arising from Inequalities of Temperature," *Philosophical Transactions of the Royal Society of London*, vol. 170, pp. 231–256, 1879.

[4] O. Reynolds, "On Certain Dimensional Properties of Matter in the Gaseous State," *Philosophical Transactions of the Royal Society of London*, vol. 170, pp. 727–845, 1879.

[5] R. W. Bosworth, A. L. Ventura, A. D. Ketsdever, and S. F. Gimelshein, "Measurement of negative thermophoretic force," *Journal of Fluid Mechanics*, vol. 805, pp. 207–221, 2016.

[6] F. Zheng, "Thermophoresis of spherical and non-spherical particles: a review of theories and experiments.," *Advances in colloid and interface science*, vol. 97, pp. 255–278, 2002.

[7] F. F. Reuss, "Notice sur un nouvel effet de l'électricité galvanique," *Mem. Soc.Imp.Nat. Moscou*, vol. 2, p. 327 –337, 1809.

[8] C. J. Biscombe, "The Discovery of Electrokinetic Phenomena: Setting the Record Straight," *Angewandte Chemie - International Edition*, vol. 56, pp. 8338–8340, 2017.

[9] S. Claesson and K. O. Pedersen, "The Svedberg. 1884-1971," in *Biographical Memoirs of Fellows of the Royal Society*, vol. 18, pp. 594–627, Royal Society, 1972.

[10] T. Svedberg and E. R. Jette, "The cataphoresis of proteins," *Journal of the American Chemical Society*, vol. 45, no. 4, pp. 954–957, 1923.

[11] N. D. Scott and T. Svedberg, "Measurements of the mobility of egg albumin at different acidities," *Journal of the American Chemical Society*, vol. 46, no. 12, pp. 2700–2707, 1924.

[12] T. Svedberg and A. Tiselius, "A new method for determination of the mobility of proteins," *Journal of the American Chemical Society*, vol. 48, no. 9, pp. 2272–2278, 1926.

[13] A. Tiselius, "A new apparatus for electrophoretic analysis of colloidal mixtures," *Transactions of the Faraday Society*, vol. 33, pp. 524–531, 1937.

[14] B. V. Derjaguin, G. P. Sidorenkov, E. A. Zubashchenkov, and E. V. Kiseleva, "Kinetic phenomena in boundary films of liquids," *Kolloidn. zh*, vol. 9, pp. 335–347, 1947.

[15] J. L. Anderson, M. E. Lowell, and D. C. Prieve, "Motion of a particle generated by chemical gradients Part 1. Non-electrolytes," *Journal of Fluid Mechanics*, vol. 117, pp. 107–121, 1982.

[16] J. L. Anderson and D. C. Prieve, "Diffusiophoresis: Migration of Colloidal Particles in Gradients of Solute Concentration," *Separation and Purification Methods*, vol. 13, no. 1, pp. 67–103, 1984.

[17] D. Velegol, A. Garg, R. Guha, A. Kar, and M. Kumar, "Origins of concentration gradients for diffusiophoresis," *Soft Matter*, vol. 12, pp. 4686–4703, 2016.

[18] S. Marbach and L. Bocquet, "Osmosis, from molecular insights to large-scale applications," *Chemical Society Reviews*, vol. 48, pp. 3102–3144, 2019.

[19] E. L. Talbot, J. Kotar, L. Parolini, L. Di Michele, and P. Cicuta, "Thermophoretic migration of vesicles depends on mean temperature and head group chemistry," *Nature Communications*, vol. 8, p. 15351, 2017.

[20] S. Shin, P. B. Warren, and H. A. Stone, "Cleaning by Surfactant Gradients: Particulate Removal from Porous Materials and the Significance of Rinsing in Laundry Detergency," *Physical Review Applied*, vol. 9, p. 034012, 2018.

[21] L. Bocquet and J. L. Barrat, "On the Green-Kubo relationship for the liquid-solid friction coefficient," *Journal of Chemical Physics*, vol. 139, p. 044704, 2013.

[22] R. P. Sear and P. B. Warren, "Diffusiophoresis in nonadsorbing polymer solutions: The Asakura-Oosawa model and stratification in drying films," *Physical Review E*, vol. 96, p. 062602, 2017.

[23] M. P. Howard and A. Nikoubashman, "Stratification of polymer mixtures in drying droplets: hydrodynamics and diffusion," *Journal of Chemical Physics*, vol. 153, p. 054901, 2020.

[24] D. Li, *Encyclopedia of Microfluidics and Nanofluidics*. Springer Reference, second ed., 2013.

[25] S. Shin, J. T. Ault, J. Feng, P. B. Warren, and H. A. Stone, "Low-Cost Zeta Potentiometry Using Solute Gradients," *Advanced Materials*, vol. 29, no. 30, pp. 1–7, 2017.

[26] J. T. Ault, S. Shin, and H. A. Stone, "Characterization of surface-solute interactions by diffusioosmosis," *Soft Matter*, vol. 15, pp. 1582–1596, 2019.

[27] H. Yoshida, S. Marbach, and L. Bocquet, "Osmotic and diffusio-osmotic flow generation at high solute concentration. II. Molecular dynamics simulations," *Journal of Chemical Physics*, vol. 146, no. 194702, 2017.

[28] B. Abécassis, C. Cottin-Bizonne, C. Ybert, A. Ajdari, and L. Bocquet, "Osmotic manipulation of particles for microfluidic applications," *New Journal of Physics*, vol. 11, p. 075022, 2009.

[29] G. Rückner and R. Kapral, "Chemically powered nanodimers," *Physical Review Letters*, vol. 98, p. 150603, 2007.

[30] J. R. Howse, R. A. Jones, A. J. Ryan, T. Gough, R. Vafabakhsh, and R. Golestanian, "Self-Motile Colloidal Particles: From Directed Propulsion to Random Walk," *Physical Review Letters*, vol. 99, p. 048102, 2007.

[31] Y. G. Tao and R. Kapral, "Design of chemically propelled nanodimer motors," *Journal of Chemical Physics*, vol. 128, p. 164518, 2008.

[32] A. Brown and W. Poon, "Ionic effects in self-propelled Pt-coated Janus swimmers," *Soft Matter*, vol. 10, pp. 4016–4027, 2014.

[33] L. Bocquet and E. Charlaix, "Nanofluidics, from bulk to interfaces," *Chemical Society Reviews*, vol. 39, pp. 1073–1095, 2010.

[34] M. Yang, R. Liu, M. Ripoll, and K. Chen, "A microscale turbine driven by diffusive mass flux," *Lab on a Chip*, vol. 15, pp. 3912–3917, 2015.

[35] J. T. Ault, P. B. Warren, S. Shin, and H. A. Stone, "Diffusiophoresis in one-dimensional solute gradients," *Soft Matter*, vol. 13, pp. 9015–9023, 2017.

[36] J. Palacci, B. Abécassis, C. Cottin-Bizonne, C. Ybert, and L. Bocquet, "Colloidal motility and pattern formation under rectified diffusiophoresis," *Physical Review Letters*, vol. 104, p. 138302, 2010.

[37] J. Palacci, C. Cottin-Bizonne, C. Ybert, and L. Bocquet, "Osmotic traps for colloids and macromolecules based on logarithmic sensing in salt taxis," *Soft Matter*, vol. 8, pp. 980–994, 2012.

[38] M. S. Mcafee, H. Zhang, and O. Annunziata, "Amplification of Salt-Induced Polymer Diffusiophoresis by Increasing Salting-Out Strength," *Langmuir*, vol. 30, no. 41, pp. 12210–12219, 2014.

[39] N. Shi, R. Nery-Azevedo, A. I. Abdel-Fattah, and T. M. Squires, "Diffusiophoretic Focusing of Suspended Colloids," *Physical Review Letters*, vol. 117, no. 25, pp. 1–5, 2016.

[40] S. Shin, J. T. Ault, P. B. Warren, and H. A. Stone, "Accumulation of colloidal particles in flow junctions induced by fluid flow and diffusiophoresis," *Physical Review X*, vol. 7, p. 041038, 2017.

[41] R. P. Sear, "Diffusiophoresis in Cells: a General Non-Equilibrium, Non-Motor Mechanism for the Metabolism-Dependent Transport of Particles in Cells," *Physical Review Letters*, vol. 122, p. 128101, 2019.

[42] S. Shin, V. S. Doan, and J. Feng, "Osmotic Delivery and Release of Lipid-Encapsulated Molecules via Sequential Solution Exchange," *Physical Review Applied*, vol. 12, p. 024014, 2019.

[43] K. P. Travis, B. D. Todd, and D. J. Evans, "Departure from Navier-Stokes hydrodynamics in confined liquids," *Physical Review E*, vol. 55, no. 4, pp. 4288–4295, 1997.

[44] B. D. Todd and P. J. Daivis, *Nonequilibrium molecular dynamics: Theory, algorithms and applications*. Cambridge University Press, 2017.

[45] M. Han, "Thermophoresis in liquids: A molecular dynamics simulation study," *Journal of Colloid and Interface Science*, vol. 284, pp. 339–348, 2005.

[46] M. J. Sanborn and R. Q. Snurr, "Predicting membrane flux of CH4 and CF4 mixtures in faujasite from molecular simulations," *AIChE Journal*, vol. 47, no. 9, pp. 2032–2041, 2001.

[47] A. Gupta, S. Shim, L. Issah, C. McKenzie, and H. A. Stone, "Diffusion of multiple electrolytes cannot be treated independently: Model predictions with experimental validation," *Soft Matter*, vol. 15, pp. 9965–9973, 2019.

[48] Y. Liu, R. Ganti, and D. Frenkel, "Pressure gradients fail to predict diffusio-osmosis," *Journal of Physics Condensed Matter*, vol. 30, p. 205002, 2018.

[49] J. P. Ebel, J. L. Anderson, and D. C. Prieve, "Diffusiophoresis of latex particles in electrolyte gradients," *Langmuir*, vol. 4, no. 2, pp. 396–406, 1988.

[50] T. Y. Chiang and D. Velegol, "Multi-ion diffusiophoresis," *Journal of Colloid and Interface Science*, vol. 424, pp. 120–123, 2014.

[51] I. Prigogine, *An introduction to thermodynamics of irreversible processes*. Interscience Publishers, 1955.

[52] S. Kjelstrup and D. Bedeaux, *Non-Equilibrium Thermodynamics of Heterogeneous Systems*. World Scientific, 2008.

[53] S. R. de Groot and P. Mazur, *Non-equilibrium thermodynamics.* New York: Dover Publications, 1984.

[54] B. J. Berne and R. Pecora, *Dynamic light scattering: with applications to chemistry, biology, and physics.* John Wiley & Sons, Inc, 2000.

[55] S. Shin, E. Um, B. Sabass, J. T. Ault, M. Rahimi, P. B. Warren, and H. A. Stone, "Size-dependent control of colloid transport via solute gradients in dead-end channels," *Proceedings of the National Academy of Sciences*, vol. 113, no. 2, pp. 257–261, 2016.

[56] J. P. Hansen and I. R. McDonald, *Theory of simple liquids*. Academic Press, 3 ed., 2006.

[57] L. D. Landau and E. M. Lifshitz, *Fluid Mechanics*, vol. 6. Pergamon Press, 2005.

[58] J. K. G. Dhont, *An Introduction to Dynamics of Colloids*. Amsterdam: Elsevier, 1996.

[59] T. D. Montenegro-Johnson, S. Michelin, and E. Lauga, "A regularised singularity approach to phoretic problems," *European Physical Journal E*, vol. 38, no. 139, 2015.

[60] J. L. Anderson and D. C. Prieve, "Diffusiophoresis Caused by Gradients of Strongly Adsorbing Solutes," *Langmuir*, vol. 7, no. 2, pp. 403–406, 1991.

[61] H. J. Keh and J. C. Weng, "Diffusiophoresis of colloidal spheres in nonelectrolyte gradients at small but finite Pélet numbers," *Colloid and Polymer Science*, vol. 279, pp. 305–311, 2001.

[62] N. Sharifi-Mood, J. Koplik, and C. Maldarelli, "Diffusiophoretic self-propulsion of colloids driven by a surface reaction: The sub-micron particle regime for exponential and van der Waals interactions," *Physics of Fluids*, vol. 25, no. 1, 2013.

[63] S. Marbach, H. Yoshida, and L. Bocquet, "Local and global force balance for diffusiophoretic transport," *Journal of Fluid Mechanics*, vol. 892, p. A6, 2020.

[64] P. J. Hoogerbrugge and J. M. V. A. Koelman, "Simulating microscopic phenomena with dissipative particle dynamics," *Europhysics Letters*, vol. 19, pp. 155–160, 1992.

[65] P. Espanol, "Fluid particle model," *Physical Review E*, vol. 57, no. 3, pp. 2930–2948, 1998.

[66] S. Chen and G. D. Doolen, "Lattice Boltzmann Method for Fluid Flows," *Annual Review of Fluid Mechanics*, vol. 30, pp. 329–364, 1998.

[67] G. Gompper, T. Ihle, D. Kroll, and R.G.Winkler, "Multi-Particle Collision Dynamics: A Particle-Based Mesoscale Simulation Approach to the Hydrodynamics of Complex Fluids," in *Advanced Computer Simulation Approaches for Soft Matter Sciences III*, pp. 349–359, Springer, Berlin, Heidelberg, 2009.

[68] A. Ajdari and L. Bocquet, "Giant amplification of interfacially driven transport by hydrodynamic slip: Diffusio-osmosis and beyond," *Physical Review Letters*, vol. 96, p. 186102, 2006.

[69] M. Yang, R. Liu, F. Ye, and K. Chen, "Mesoscale simulation of phoretically osmotic boundary conditions," *Soft Matter*, vol. 13, pp. 647–657, 2017.

[70] J. L. Barrat and L. Bocquet, "Large slip effect at a nonwetting fluid-solid interface," *Physical Review Letters*, vol. 82, no. 23, pp. 4671–4674, 1999.

[71] M. E. Tuckerman, *Statistical Mechanics: Theory and Molecular Simulation*. Oxford University Press, 2009.

[72] Y. Liu, R. Ganti, H. G. Burton, X. Zhang, W. Wang, and D. Frenkel, "Microscopic Marangoni Flows Cannot Be Predicted on the Basis of Pressure Gradients," *Physical Review Letters*, vol. 119, p. 224502, 2017.

[73] E. Mangaud and B. Rotenberg, "Sampling mobility profiles of confined fluids with equilibrium molecular dynamics simulations," *Journal of Chemical Physics*, vol. 153, p. 044125, 2020.

[74] J. Wei, S. Ramírez-Hinestrosa, J. Dobnikar, and D. Frenkel, "Effect of the interaction strength and anisotropy on the diffusio-phoresis of spherical colloids," *Soft Matter*, vol. 16, pp. 3621–3627, 2020.

[75] S. Ramírez-Hinestrosa, H. Yoshida, L. Bocquet, and D. Frenkel, "Studying polymer diffusiophoresis with non-equilibrium molecular dynamics," *The Journal of Chemical Physics*, vol. 152, p. 164901, 2020.

[76] M. P. Allen and D. J. Tildesley, *Computer Simulation of liquids*. Clarendon Press, 1987.

[77] D. Frenkel and B. Smit, *Understanding molecular simulation: from Algorithms to Applications*. Academic Press, 2 ed., 2002.

[78] E. J. Maginn, A. T. Bell, and D. N. Theodorou, "Transport diffusivity of methane in silicalite from equilibrium and nonequilibrium simulations," *The Journal of Physical Chemistry*, vol. 97, pp. 4173–4181, 1993.

[79] G. S. G. Heffelfinger and F. v. Swol, "Diffusion in Lennard-Jones Fluids Using Dual Control Volume Grand Canonical Molecular Dynamics Simulation (DCV- GCMD)," *Journal of Chemical Physics*, vol. 100, p. 7548–7552, 1994.

[80] J. M. D. MacElroy, "Nonequilibrium molecular dynamics simulation of diffusion and flow in thin microporous membranes," *The Journal of Chemical Physics*, vol. 101, pp. 5274–5280, 1994.

[81] G. Arya, H. C. Chang, and E. J. Maginn, "A critical comparison of equilibrium, non-equilibrium and boundary-driven molecular dynamics techniques for studying transport in microporous materials," *Journal of Chemical Physics*, vol. 115, pp. 8112–8124, 2001.

[82] S. Chempath, R. Krishna, and R. Q. Snurr, "Nonequilibrium molecular dynamics simulations of diffusion of binary mixtures containing short n-alkanes in faujasite," *Journal of Physical Chemistry B*, vol. 108, pp. 13481–13491, 2004.

[83] A. P. Thompson and G. S. Heffelfinger, "Direct molecular simulation of gradient-driven diffusion of large molecules using constant pressure," *The Journal of Chemical Physics*, vol. 110, pp. 10693–10705, 1999.

[84] D. J. Evans and G. P. Morriss, "Non-Newtonian molecular dynamics," *Computer Physics Reports*, vol. 1, pp. 297–343, 1984.

[85] D. J. Evans and G. Morriss, *Statistical Mechanics of Nonequilibrium Liquids*. Cambridge University Press, second ed., 2008.

[86] D. J. Evans, W. G. Hoover, B. H. Failor, B. Moran, and A. J. Ladd, "Nonequilibrium molecular dynamics via Gauss's principle of least constraint," *Physical Review A*, vol. 28, no. 2, pp. 1016–1021, 1983.

[87] W. G. Hoover, "Canonical dynamics: Equilibrium phase-space distributions," *Physical Review A*, vol. 31, no. 3, pp. 1695–1697, 1985.

[88] X. Liu, S. K. Schnell, J.-M. Simon, P. Krüger, D. Bedeaux, S. Kjelstrup, A. Bardow, and T. J. H. Vlugt, "Diffusion Coefficients from Molecular Dynamics Simulations in Binary and Ternary Mixtures," *International Journal of Thermophysics*, vol. 34, pp. 1169–1196, 2013.

[89] R. Ganti, Y. Liu, and D. Frenkel, "Molecular Simulation of Thermo-osmotic Slip," *Physical Review Letters*, vol. 119, p. 038002, 2017.

[90] B. V. Derjaguin and S.S Dukhin, "Application of thermodynamics of irreversible processes to the electrodiffusion theory of electrokinetic effects," in *Research in Surface Forces*, Springer US, 1971.

[91] A. Katzir-Katchalsky and P. F. Curran, *Nonequilibrium thermodynamics in biophysics*. Harvard University Press, 1965.

[92] J. L. Anderson, "Colloid transport by interfacial forces," *Annual Review of Fluid Mechanics*, vol. 21, pp. 61–99, 1989.

[93] B. Derjaguin, N. Churaev, and V. Muller, *Surface Forces*. Springer Science+Business Media, LLC, 1987.

[94] B. D. Todd, D. J. Evans, and P. J. Daivis, "Pressure tensor for inhomogeneous fluids," *Physical Review E*, vol. 52, no. 2, pp. 1627–1638, 1995.

[95] L. Fu, S. Merabia, and L. Joly, "What Controls Thermo-osmosis? Molecular Simulations Show the Critical Role of Interfacial Hydrodynamics," *Physical Review Letters*, vol. 119, p. 214501, 2017.

[96] S. Plimpton, "Fast Parallel Algorithms for Short-Range Molecular-Dynamics," *Journal of Computational Physics*, vol. 117, pp. 1–19, 1995.

[97] H. Yoshida, H. Mizuno, T. Kinjo, H. Washizu, and J. L. Barrat, "Molecular dynamics simulation of electrokinetic flow of an aqueous electrolyte solution in nanochannels," *Journal of Chemical Physics*, vol. 140, p. 214701, 2014.

[98] H. Yoshida and L. Bocquet, "Labyrinthine water flow across multilayer graphene-based membranes: Molecular dynamics versus continuum predictions," *Journal of Chemical Physics*, vol. 144, p. 234701, 2016.

[99] J. D. Weeks, D. Chandler, and H. C. Andersen, "Role of Repulsive Forces in Determining Equilibrium Structure of Simple Liquids," *Journal of Chemical Physics*, vol. 54, no. 12, pp. 5237–5247, 1971.

[100] L. Bocquet and J.-L. Barrat, "Flow boundary conditions from nano- to micro-scales," *Soft Matter*, vol. 3, p. 685, 2007.

[101] I. Bitsanis, J. J. Magda, M. Tirrell, and H. T. Davis, "Molecular dynamics of flow in micropores," *The Journal of Chemical Physics*, vol. 87, pp. 1733–1750, 1987.

[102] B. D. Todd and J. S. Hansen, "Nonlocal viscous transport and the effect on fluid stress," *Physical Review E - Statistical, Nonlinear, and Soft Matter Physics*, vol. 78, p. 051202, 2008.

[103] J. S. Paustian, C. D. Angulo, R. Nery-Azevedo, N. Shi, A. I. Abdel-Fattah, and T. M. Squires, "Direct measurements of colloidal solvophoresis under imposed solvent and solute gradients," *Langmuir*, vol. 31, no. 15, pp. 4402–4410, 2015.

[104] I. Williams, S. Lee, A. Apriceno, R. Sear, and G. Battaglia, "Diffusioosmotic and convective flows induced by a non-electrolyte concentration gradient," *Pnas*, 2020.

[105] A. S. Khair, "Diffusiophoresis of colloidal particles in neutral solute gradients at finite Péclet number," *Journal of Fluid Mechanics*, vol. 731, pp. 64–94, 2013.

[106] R. Golestanian, T. B. Liverpool, and A. Ajdari, "Propulsion of a molecular machine by asymmetric distribution of reaction products," *Physical Review Letters*, vol. 94, p. 220801, 2005.

[107] R. Golestanian, T. B. Liverpool, and A. Ajdari, "Designing phoretic micro- and nano-swimmers," *New Journal of Physics*, vol. 9, p. 126, 2007.

[108] N. O. Young, J. S. Goldstein, and M. J. Block, "The motion of bubbles in a vertical temperature gradient," *Journal of Fluid Mechanics*, vol. 6, no. 3, pp. 350–356, 1959.

[109] R. S. Subramanian, "Slow migration of a gas bubble in a thermal gradient," *AIChE Journal*, vol. 27, no. 4, pp. 646–654, 1981.

[110] E. Ruckenstein, "Can phoretic motions be treated as interfacial tension gradient driven phenomena?," *Journal of Colloid And Interface Science*, vol. 83, no. 1, pp. 77–81, 1981.

[111] C. Lee, C. Cottin-Bizonne, A. L. Biance, P. Joseph, L. Bocquet, and C. Ybert, "Osmotic flow through fully permeable nanochannels," *Physical Review Letters*, vol. 112, p. 244501, 2014.

[112] N. Sharifi-Mood, J. Koplik, and C. Maldarelli, "Molecular dynamics simulation of the motion of colloidal nanoparticles in a solute concentration gradient and a comparison to the continuum limit," *Physical Review Letters*, vol. 111, p. 184501, 2013.

[113] N. Clisby and B. Dünweg, "High-precision estimate of the hydrodynamic radius for self-avoiding walks," *Physical Review E*, vol. 94, p. 052102, 11 2016.

[114] M. Bishop, M. H. Kalos, and H. L. Frisch, "Molecular-Dynamics of Polymeric Systems," *Journal of Chemical Physics*, vol. 70, pp. 1299–1304, 1979.

[115] B. Dünweg and K. Kremer, "Molecular dynamics simulation of a polymer chain in solution," *The Journal of Chemical Physics*, vol. 99, pp. 6983–6997, 1993.

[116] X. Wang, S. Ramírez-Hinestrosa, J. Dobnikar, and D. Frenkel, "The Lennard-Jones potential: When (not) to use it," *Physical Chemistry Chemical Physics*, vol. 22, pp. 10624–10633, 2020.

[117] J. Rauch and W. Köhler, "On the Molar Mass Dependence of the Thermal Diffusion Coefficient of Polymer Solutions," *Macromolecules*, vol. 38, pp. 3571–3573, 5 2005.

[118] M. S. McAfee and O. Annunziata, "Effect of particle size on salt-induced diffusiophoresis compared to brownian mobility," *Langmuir*, vol. 30, no. 17, pp. 4916–4923, 2014.

[119] J. G. Kirkwood, "The general theory of irreversible processes in solutions of macromolecules," *Journal of Polymer Science*, vol. 12, p. 1, 1954.

[120] G. Strobl, *The Physics of Polymers: Concepts for Understanding their Structure and Behavior*. Springer-Verlag, 3 ed., 2007.

[121] J. E. Lennard-Jones, "Cohesion," *Proceedings of the Physical Society*, vol. 43, pp. 461–482, 9 1931.

[122] A. Rahman, "Correlations in the motion of atoms in liquid argon," *Physical Review*, vol. 136, p. A405, 10 1964.

[123] W. W. Wood and F. R. Parker, "Monte carlo equation of state of molecules interacting with the lennard-jones potential. I. A supercritical isotherm at about twice the critical temperature," *The Journal of Chemical Physics*, vol. 27, pp. 720–733, 9 1957.

[124] M. A. Van Der Hoef and P. A. Madden, "Three-body dispersion contributions to the thermodynamic properties and effective pair interactions in liquid argon," *Journal of Chemical Physics*, vol. 111, pp. 1520–1526, 7 1999.

[125] K. Meier, A. Laesecke, and S. Kabelac, "Transport coefficients of the Lennard-Jones model fluid. I. Viscosity," *Journal of Chemical Physics*, vol. 121, pp. 3671–3687, 2004.

[126] P. J. Daivis and D. J. Evans, "Comparison of constant pressure and constant volume nonequilibrium simulations of sheared model decane," *The Journal of Chemical Physics*, vol. 100, pp. 541–547, 1994.

[127] N. Meyer, J. F. Wax, and H. Xu, "Viscosity of Lennard-Jones mixtures: A systematic study and empirical law," *Journal of Chemical Physics*, vol. 148, p. 234506, 2018.

[128] H. Hasimoto, "On the periodic fundamental solutions of the Stokes equations and their application to viscous flow past a cubic array of spheres," *Journal of Fluid Mechanics*, vol. 5, no. 2, p. 317, 1959.

[129] A. S. Sangani and A. Acrivos, "Slow flow through a periodic array of spheres," *International Journal of Multiphase Flow*, vol. 8, no. 4, pp. 343–360, 1982.